TECHNISCHE UNIVERSITÄT MÜNCHEN

Max-Planck-Institut für Plasmaphysik

Investigations on radial electric fields in the edge transport barrier of H-mode discharges

Bernd Wieland

Vollständiger Abdruck der von der Fakultät für Physik der Technischen Universität München zur Erlangung des akademischen Grades eines

Doktors der Naturwissenschaften (Dr. rer. nat.)

genehmigten Dissertation.

Vorsitzender:		Univ.- Prof. Dr. Fiedrich
Prüfer der Dissertation:	1.	Hon.- Prof. Dr. Günter
	2.	apl. Prof. Dr. Feulner

Die Dissertation wurde am 28.07.2011 bei der Technischen Universität München eingereicht und durch die Fakultät für Physik am 14.09.2011 angenommen.

Für Naomi

Diese Arbeit wurde am Tokamak ASDEX Upgrade in Garching bei München, Deutschland, durchgeführt. Dabei wurde eine neue Diagnostik zur Messung des radialen elektrischen Feldes aufgebaut, die auf der Messung der passiven Emission von einfach ionisierten Helium-Ionen basiert, die in einer dünnen Schicht am Plasmarand vorkommen. An ITER wird die H-mode (high confinement mode) der bevorzugte Betriebsmodus sein. Dieser zeichnet sich durch einen verbesserten Energieeinschluss und eine starke Transportbarriere am Plasmarand aus. Die allgemein akzeptierte Theorie, dass der Gradient des radialen elektrischen Feldes und die damit verbundene verscherte Plasmarotation turbulenten Transport reduziert, ist bisher experimentell noch nicht nachgewiesen. Deshalb tragen die Messungen dieser neuen Diagnostik zu einem aktuellen und bisher nicht vollkommen verstandenen Thema der Plasmaphysik bei.

Das Hauptthema dieser Arbeit ist die Messung des radialen elektrischen Feldes in der Transportbarriere am Plasmarand von H-mode-Entladungen und der Vergleich der Tiefe dieses Feldes mit den Vorhersagen der neoklassischen Theorie. Aufgrund der Verwendung von passiver Spektroskopie sind Messungen in nahezu allen Typen von Plasmaentladungen möglich, ohne das Plasma zu beeinflussen oder zu stören. Die notwendige Entfaltung der linien-integrierten Messung wurde mittels integrierter Datenanalyse durchgeführt. Dabei wurde ein Vorwärts-Model aufgesetzt, welches die Rekonstruktion der benötigten radialen Profile ermöglichte. Hierbei kamen Bayes'sche Statistik sowie ein "Marcov chain Monte Carlo"-Algorithmus zum Einsatz. Die Vorteile dieser Methode sind eine konsistente Fehlerfortpflanzung aller gemessenen Größen, die automatische Berücksichtigung von Außreißern sowie das einfache Einbinden von Randbedingungen und Hintergrundwissen. Die Genauigkeit und Verlässlichkeit dieser Methode wird ausführlich in einer Sensitivitätsstudie diskutiert, wobei der Schwerpunkt auf den Auswirkungen der Unsicherheit in der Rekonstruktion des magnetischen Gleichgewichts liegt.

Das wichtigste Ergebnis dieser Arbeit ist, dass das Minimum im gemessenen radialen elektrischen Feld gut duch die neoklassische Theorie beschrieben wird. Dies deutet darauf hin, dass der turbulente Transport in der dominanten Ionen-Spezies in dem Bereich mit starker Verscherung reduziert ist. Um diese Annahme zu untermauern, wurde die Entwicklung des radialen elektrischen Feldes und der Randgradienten für unterschiedliche Arten von Entladungen untersucht. Dabei wurde der Zusammenbruch und die Wiederaufbauphase der Profile während eines ELM-Zyklus betrachtet. Weiterhin zeigte die Entwicklung der E_r-Profile während eines L-H-Übergangs gute Übereinstimmung von Messung und Theorie, sowohl in der L-mode als auch in der H-mode. Beim Vergleichen von Entladungen über einen weiten Bereich von unterschiedlichen normierten Stoßfrequenzen konnte die stoßfrequenz- und temperaturabhängige Abweichung der neoklassischen Theorie von $\nabla p/n$ bestätigt werden.

This thesis was carried out at the ASDEX Upgrade Tokamak in Garching near Munich, Germany. A new diagnostic for measuring the radial electric field was implemented, which utilizes the passive emission of singly ionized Helium, existing in a small shell at the plasma boundary. The H-mode is the preferred working regime for ITER, which is characterized by improved confinement and a strong transport barrier at the plasma edge. The widely accepted theory, that the radial electric field gradients and the concomitant sheared plasma flows reduce turbulent transport in the pedestal region, leading to these steep gradients in the density and temperature profiles, has not yet been experimentally verified. Therefore, the measurements of this diagnostic contribute to an ongoing and not fully understood topic in plasma physics.

This thesis focuses on the measurement of the radial electric field in the edge transport barrier of H-mode discharges and the comparison of its depth with the E_r depth predicted by neoclassical theory. By using passive spectroscopy, measurements for nearly all types of discharges are possible without disturbing or influencing the plasma. The necessary deconvolution of the line integrated measurements was performed by applying integrated data analysis. A forward model was set up, which allows the reconstruction of the involved radial profiles using Bayesian statistics combined with a “Marcov chain Monte Carlo” code. The advantages of this method are consistent error propagation of all measured quantities, automatic outlier treatment and simple integration of background knowledge as well as boundary conditions. The accuracy and reliability of this method is shown in a sensitivity study, with focus on the effects of the uncertainties of the equilibrium reconstruction.

The main result of this thesis is, that the minimum in the measured radial electric field is well described by neoclassical theory, indicating that in the region with strong velocity shear the turbulent transport for the main ions is reduced. To corroborate this assumption, the development of the radial electric field and the edge kinetic profiles were analyzed for different types of discharges. This includes the break-down and the recovery of the edge profiles during an ELM cycle. The E_r measurements during a L-H transition showed good agreement of theory and measurement in both L- and H-mode. Comparing discharges with a wide range in collisionality confirms the temperature and collisionality dependent deviation of neoclassical theory from $\nabla p/n$.

An dieser Stelle möchte ich allen Leuten, die mir bei der Erstellung dieser Dissertation geholfen haben, meinen Dank aussprechen. Die Zeit am Max-Planck Institut für Plasmaphysik hat mir sehr viel Spaß bereitet. Auch mein physikalisches Verständnis wurde durch zahlreiche interne Vorträge, Diskussionen und private Gespräche gefestigt und wesentlich erweitert. Hierfür möchte ich dem gesamten ASDEX Upgrade Team danken.

Ein besonderer Dank geht an meine Doktormutter Frau Prof. S. Günter, die diese Arbeit ermöglicht hat und durch die hervorragende akademische Betreuung stets für einen reibungslosen Ablauf gesorgt hat.
Außerdem gebührt Frau Dr. E. Wolfrum ebenfalls ein besonderer Dank, wegen der hervorragenden Betreuung während meiner gesamten Zeit am IPP. Sie hatte stets ein offenes Ohr für meine Fragen, unterstützte mich unermüdlich bei der Vorbereitung von Vorträgen und Poster und hatte jederzeit einen guten Rat zur Hand.

Für die zahlreichen Gespräche zum Thema Bayes'sche Statistik und integrierte Datenanalyse bin ich Herrn Dr. R. Fischer zu großem Dank verpflichtet. Seine Ratschläge und Unterstützung bei der Fehlersuche beschleunigten die Entwicklung der vorgestellen Diagnostik enorm. Weiterhin möchte ich auch Herrn Dr. T. Pütterich für sehr hilfreiche Gespräche zur Plasmarotation und zu Driftgeschwindigkeiten danken. Bei der Erstellung des Theorie-Teils der Arbeit, hatte Herrn Dr. A. Bergmann immer eine gute Antwort auf meine Fragen zur neoklassischen Theorie parat, wofür ich auch ihm herzlich danken möchte.

Herrn Dr. K. Behler und Herrn R. Merkel von der CODAC-Gruppe danke ich für die geduldige Unterstützung bei Computerproblemen auf dem Sun-System, sowie Herrn Dr. U. von Toussaint für die Lösung von Problemen mit dem Linux-Cluster. Insbesondere aber Herrn U. Mszanowski für entscheidende Tipps zur Optimierung und Parallelisierung von Fortran-Programmen.

Für die Unterstützung beim Betrieb der Spektrometer und bei Kalibrierungsarbeiten gebührt Frau Dr. E. Wolfrum und Herrn B. Sieglin ebenfalls großer Dank.

Ganz herzlich möchte ich mich natürlich auch bei den Korrekturlesern Herrn Dr. A. Bergmann, Herrn Dr. G. Conway, Herrn Dr. R. Fischer, Frau Prof. S. Günter, Frau E. Viezzer und Frau Dr. E. Wolfrum bedanken, die bis zur letzten Minute mit hilfreichen Tipps und Ratschlägen wesentlich zum Gelingen dieser Arbeit beigetragen haben.

Herrn J. Hausmann möchte ich an dieser Stelle ebenfalls für die Wartung des Versuchsaufbaus und die technische Unterstützung bei der Betreuung des Fortgeschrittenen-Praktikums danken.

Ein großer Dank geht auch an alle anderen Doktoranden und Doktorandinnen sowie Diplomanden und Diplomandinnen am IPP, für die großartige Gemeinschaft sowohl in physikalischer wie auch in privater Hinsicht. Dies gilt insbesondere für meine Zimmerkol-

legen Mike Dunne, Sina Fietz, Benedikt Geiger, Steffen Potzel und Philip Schneider, die mit ihrer lockeren und erfrischenden Art eine mitunter abwechslungsreiche, aber auch sehr produktive Arbeitsumgebung geschaffen haben. Auch bei den regelmäßigen Kaffee-Gästen, Jurrian Boom, Ivo Classen, Tim Happel und Christian Vorpahl möchte ich mich für hilfreiche und motivierende Worte bedanken.

Frau Prof. S. Günter, Prof. Herrn U. Stroth, Frau Dr. E. Wolfrum und Herrn Prof. H. Zohm danke ich darüber hinaus für tatkräftige Unterstützung und motivierende Worte bei der Planung meines weiteren beruflichen Werdegangs.

Nicht zuletzt geht noch ein ganz herzlicher Dank an meine Eltern, meine Frau sowie meine Freunde, die mich fortwährend unterstützt und motiviert haben.

Contents

List of Figures **IX**

1 Introduction **1**
1.1 Fusion . . . 1
1.2 Magnetic confinement . . . 2
1.2.1 1D confinement . . . 3
1.2.2 2D confinement . . . 3
1.3 Confinement modes . . . 5
1.3.1 Transport processes . . . 6
1.3.2 H-mode plasma, a motivation for this thesis . . . 8
1.4 Contents of this work . . . 11

2 Particle movement **13**
2.1 Coordinate system . . . 13
2.2 Equilibrium reconstruction . . . 15
2.3 Guiding-center approach . . . 16
2.4 Transport theory . . . 19
2.4.1 Radial force balance equation . . . 20
2.4.2 Radial particle transport . . . 20
2.4.3 Parallel particle flux . . . 22
2.4.4 Parallel ion velocity . . . 25
2.5 Flows and turbulence . . . 26

3 Atomic physics **29**
3.1 Line emission . . . 29
3.1.1 Collisional-Radiative model . . . 29
3.1.2 Photon emission coefficients . . . 32
3.1.3 Passive spectrum . . . 34
3.2 Corrections . . . 35

4 Diagnostics **39**
4.1 Edge diagnostics . . . 39
4.2 Combined profile reconstruction . . . 41
4.3 Consideration of ELMs . . . 43

5 Experimental setup 45
5.1 Diagnostic design . . . 45
5.2 Raw data . . . 47
5.3 Calibration . . . 48

6 Probabilistic data analysis 51
6.1 Bayesian probability theory . . . 51
6.2 Likelihood PDF . . . 52
6.2.1 Forward model . . . 53
6.2.2 Measured data . . . 56
6.3 Prior PDF . . . 59
6.3.1 Uncertain prior knowledge . . . 60
6.3.2 Restrictions on free model parameters . . . 61
6.3.3 Restrictions on calculated profiles . . . 64
6.4 Posterior PDF . . . 65
6.4.1 Detection of the maximum . . . 65
6.4.2 Error estimation . . . 66
6.4.3 Marcov chain Monte Carlo . . . 66
6.4.4 Model run-time . . . 68

7 Sensitivity study 71
7.1 First result . . . 71
7.1.1 Discharge #23227 . . . 71
7.1.2 Results . . . 72
7.2 Variation in equilibrium reconstruction . . . 76
7.3 Effects due to He II fine structure . . . 79
7.4 Possible experimental improvements . . . 80

8 Results 83
8.1 Previous radial electric field measurements . . . 83
8.2 Comparison to theory . . . 84
8.3 Effect of ELMs . . . 86
8.4 Plasma parameter scans . . . 89
8.4.1 NBI heating power scan . . . 89
8.4.2 Gas puff scan . . . 91
8.5 L-H transition . . . 93
8.6 Dependency of E_r on collisionality . . . 96

9 Summary and Conclusions 99

Bibliography XI

Glossary XVI

Index XXI

List of Figures

1.1 Cross-section of different fusion reactions . . . 2
1.2 Guiding-center approach . . . 2
1.3 Sketch of a Tokamak . . . 4
1.4 Nested magnetic flux surfaces . . . 4
1.5 Sketch of ASDEX Upgrade . . . 5
1.6 Reconstruction of flux surfaces . . . 5
1.7 Schematic of free (red) and trapped (blue) particles . . . 7
1.8 Neoclassic transport regimes . . . 7
1.9 Time traces and radial edge profiles of a discharge with a L-H transition 9
1.10 Sketch of different ELM-types, explained by Peeling-Ballooning theory . 10

2.1 Sketches of three different coordinate systems used at ASDEX Upgrade . 14
2.2 Illustration of drift motion . . . 17
2.3 Sketch of Pfirsch-Schlüter currents . . . 17
2.4 Sketch of force from parallel friction . . . 25
2.5 Edge toroidal ion velocity and Pfirsch-Schlüter return flows . . . 26
2.6 Effect of sheared velocity on turbulent eddies . . . 28
2.7 Decorrelation and absorbtion of eddies by sheared flow . . . 28

3.1 Sketch of emission shells . . . 32
3.2 Comparison of different contributions to the emission profile . . . 32
3.3 Temperature and density dependence of the PEC . . . 34
3.4 Fine structure splitting . . . 35
3.5 Comparison of fine structure splitting for different temperatures . . . 36
3.6 Line splitting for different magnetic field regions . . . 37

4.1 AUGPed fit of pedestal profiles (ELM synchronized) . . . 41
4.2 Comparison of ELM and inter-ELM edge profiles . . . 42
4.3 Positions of DCN laser beams . . . 42
4.4 Time evolution of edge temperature and density profiles . . . 43

5.1 Setup of the diagnostic . . . 45
5.2 Typical spectrum measured by the LIA spectrometer . . . 46
5.3 Typical spectrum measured by the LIC spectrometer . . . 46
5.4 Time evolution of the emission spectrum line center of one channel . . . 47
5.5 Central wavelength plotted over the radius . . . 47
5.6 3D plot of the experimental setup . . . 50

6.1 Flow chart of the forward model 53
6.2 Sketch of the determination of the conversion factor 58
6.3 Comparison of Gaussian and Cauchy shaped probability density functions 59
6.4 Comparison between mean value and marginal posterior PDF 68

7.1 Important plasma parameters of the AUG discharge #23227 72
7.2 Comparison of measured spectra of shot #23227 with the model output . 73
7.3 Profiles directly related to the measured data 75
7.4 Applied electron density and temperature profiles 75
7.5 Determined He^+ emission and E_r profile 75
7.6 Analysis of different shifts in the electron density 76
7.7 Analysis of different shifts in the electron temperature 78
7.8 Analysis of different toroidal rotation profiles 79
7.9 Analysis of fine structure and Paschen-Back splitting 80

8.1 Evolution of the radial electric field during an ELM cycle 87
8.2 Neoclassical coefficient and collisionality during an ELM cycle 88
8.3 Evolution of the profiles for different NBI heating 90
8.4 Important plasma parameters of the gas-scan 91
8.5 Comparison of discharges with three different gas puff levels 92
8.6 Important plasma parameters of the AUG discharge #24923 94
8.7 Development of the radial electric field during the L-H transition 95
8.8 Collisionality dependence of the radial electric field 97
8.9 Comparison of neoclassic prediction to $\nabla p/n$ 97

1 Introduction

1.1 Fusion

The process of combining two light elements (e.g. two Helium atoms) to a heavier one is called nuclear fusion. This is the opposite of nuclear fission, the process utilized in todays atomic power plants, where a heavier atom (e.g. ^{235}U) is split into lighter elements. In the following, this work will focus on topics related to fusion. This process can also be used as a power source by freeing atomic energy. The mass of the resulting heavier atom is smaller than the sum of the masses of the two initial atoms. The mass difference is set free in form of energy, which is several orders of magnitude higher than for chemical reactions using fossil fuels. In times of restricted fossil resources and a strong public disapproval concerning atomic waste from nuclear fission devices, fusion could be a promising way toward a long lasting and clean energy source.

Energy source of stars: Looking at the sky, we can see billions of working fusion power plants: the stars. The nearest one, the sun, has brought up the question for its energy source a long time ago and therefore enforces the research on fusion devices. The solution was found after the discovery of the atomic nucleus and the tunnel effect: the so-called proton-proton chain reaction [1].

$$4p \longrightarrow {}^{4}_{2}He + 2e^{+} + 2\nu_e + 26.7\,\mathrm{MeV} \tag{1.1}$$

Two protons p fuse into one Deuterium atom, together with another proton ${}^{3}_{2}He$ is formed. Two ${}^{3}_{2}He$ atoms can create one ${}^{4}_{2}He$ atom. The final process in equation (1.1) shows the fusion of 4 protons to one He nucleus together with 2 free electrons e, 2 neutrinos ν_e and $26.7MeV$ of energy.

The sun provides certain conditions to enable the proton-proton chain: high density and high temperature. Both of them are necessary because of the low cross-section of the proton-proton fusion. High density (of about $10^{30}\,\frac{1}{\mathrm{m}^3}$ in the core) is maintained by the gravitational forces, which requires a minimal mass of about one tenth of the solar mass (about $1.2 \cdot 10^{30}\,\mathrm{kg}$). This highly efficient gravitational confinement also enables a high temperature of about $10^{7}\,\mathrm{K}$, which is still too little to overcome the Coulomb barrier of a proton but provides sufficient tunneling probability to maintain the fusion reaction.[2]

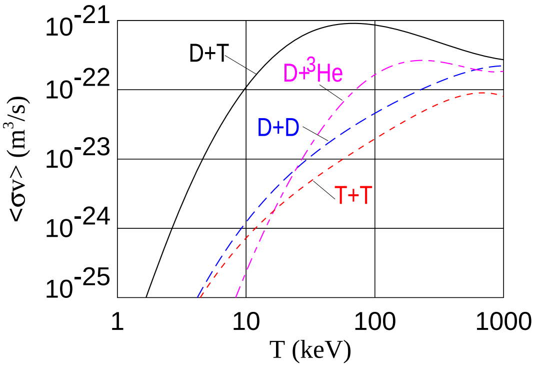

Figure 1.1: Cross-section of different fusion reactions

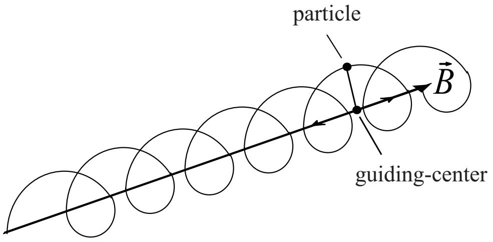

Figure 1.2: Guiding-center approach

Modifications for fusion on earth: Trying to design a fusion power plant on the basis of the proton-proton chain fails due to the limitations on size required for gravitational confinement. A solution to this problem can be achieved by replacing gravitational confinement by magnetic confinement, utilizing the response of charged particles to magnetic fields. Due to the fact, that this sort of confinement is less efficient and the amount of plasma in an earth bound device has to be drastically reduced, the cross-section is much too low. Therefore, other fusion reactions have to be explored. As can be seen in figure 1.1, the Deuterium-Tritium (D-T) reaction has its maximum at the lowest temperature, which leads to sufficiently high cross-sections for fusion devices.

$$D + T \longrightarrow {}^4_2He + n + 17.6\,\mathrm{MeV} \tag{1.2}$$

Tritium is radioactive with a half-life of 12.3 years and is therefore not naturally available. It has to be bred from Lithium by exposing it to neutrons. The high availability of Lithium together with the production of neutrons in the D-T fusion reaction will assure the required amount of Tritium. The second element, Deuterium, is naturally available with a percentage of 0.015 % within normal water and therefore also sufficiently available.

1.2 Magnetic confinement

The physical basis for magnetic confinement is the Lorentz-force acting on charged particles. Due to the high temperatures, a plasma consists of ionized atoms and free electrons. Applying a strong magnetic field forces all particles to gyrate around the magnetic field-lines and thus, particle-transport perpendicular to the magnetic field is strongly reduced. In plasma physics, it is a common simplification to describe the resulting particle motion with the guiding-center approach. The movement of the center of the gyration (guiding-center) on the magnetic field is treated separately from the circular motion around the guiding-center (see figure 1.2). A complete suppression of perpendicular motion is not possible due to drift motion (see chapter 2) and turbulent processes. Choosing different magnetic geometries, a diversity of fusion devices with completely different properties can be built.

1.2.1 1D confinement

Following the book of Freidberg [3], the simplest shape of the magnetic field $\vec{B}$ is linear ($\vec{B} = B \cdot \hat{e}_Z$) along the Z-axis ($\hat{e}_Z$) and homogeneous. Particles within this field have a high flexibility in motion along the Z-Axis but are well confined radially by the magnetic field. This so-called θ-pinch has a good radial confinement and stability, but the high particle losses due to the open ends in Z-direction makes it unfavorable as basis for a fusion device. Bending to a torus-like shape to reduce end losses is not possible, without losing radial confinement.

The alternative approach for a one dimensional device is the Z-pinch. In this case, the current $\vec{I} = I_0 \cdot \hat{e}_Z$ is applied externally and a poloidal magnetic field is induced. Radial confinement is maintained by balancing the particle and magnetic pressure with the tension force, that origins from the curvature of the magnetic field lines. Overall confinement is also very poor because of the end losses. This concept can be bent to a torus, but suffers from stability problems.

1.2.2 2D confinement

Low-β Tokamak: One possible solution to the end loss problem is a toroidal plasma combining both concepts, the θ- and the Z-pinch, resulting in helically twisted magnetic field lines. In a Tokamak a strong toroidal field is applied by external coils (see figure 1.3) similar to the θ-pinch. The poloidal part of the magnetic field is induced by a toroidal plasma current $\vec{J}_{tor}$ driven by a transformer. Radial confinement and heating is provided by this current, similar to the Z-pinch. One way to maintain toroidal confinement is by applying an additional vertical magnetic field $\vec{B}_v$. Forces pushing the plasma against the outer wall (e.g. forces arising from the toroidal magnetic field) are now balanced by an inward $\vec{J}_{tor} \times \vec{B}_v$ force. The strong toroidal field maintains the stability of the plasma. However, this setup is still not desirable as fusion power device, because the Z-pinch like confinement results in a low β:

$$\beta = \frac{2\mu_0 P}{B_t^2 + B_p^2}. \tag{1.3}$$

β is the ratio of kinetic pressure P to magnetic pressure, given by the square of the total magnetic field (toroidal B_t and poloidal B_p component) divided by two times the vacuum permeability μ_0.[4] Additionally, the plasma heating is limited by the maximal

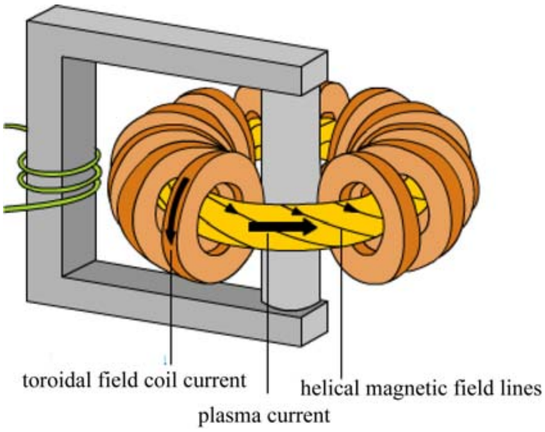

Figure 1.3: Sketch of a Tokamak[1]

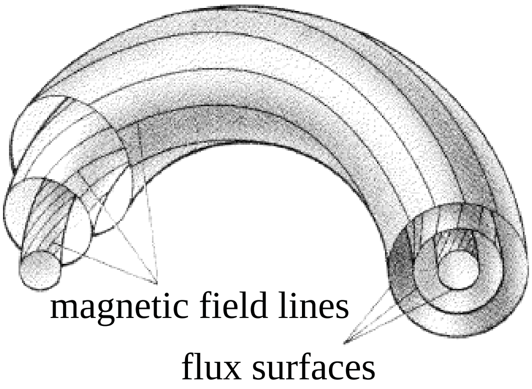

Figure 1.4: Nested magnetic flux surfaces[1]

current due to technical and stability reasons as well as the plasma resistivity $\propto T^{-\frac{3}{2}}$, that decreases with increasing temperature.

High-β Tokamak: Improvements to this concept can be achieved by applying external heating sources. Increased plasma temperature leads to a higher pressure and therefore increases β. Confinement now is sustained, θ-pinch like, by arising poloidal diamagnetic currents. The shape of the plasma can be visualized by creating nested surfaces enclosing a constant amount of magnetic flux, so-called flux surfaces (see figure 1.4). Important plasma parameters like temperature, pressure or density can be assumed to be constant on these surfaces. In the low-β case, these are nested concentric circles in a poloidal projection, but in the high-β case, there is an outward shift (the Shafranov-shift) of more inwardly situated surfaces relative to outer ones. This results in a compression of flux surfaces on the low field side. The direction from the plasma center to the outer wall of the torus is called low field side and the direction from the plasma center to the center of the torus is called high field side. The reason for this is the decaying magnetic field directed from the torus center outwards. The effects due to non equidistant flux surfaces are discussed in detail in section 2. Increasing β also requires a stronger vertical magnetic field to maintain the toroidal force balance and also an increasing plasma current to avoid a β limit.

Divertor devices: In a real fusion experiment, the vacuum vessel has to be protected from the hot plasma. This can be accomplished with a special shaping of the magnetic field. A separatrix is created, which separates closed magnetic field lines from open ones that lead particles in a separate region, called divertor chamber. Unconfined particles hit special divertor plates, which can manage a high heat flux. Additionally, neutral particles sputtered from the divertor plates have reduced probability of reaching the plasma and causing energy losses due to line radiation.

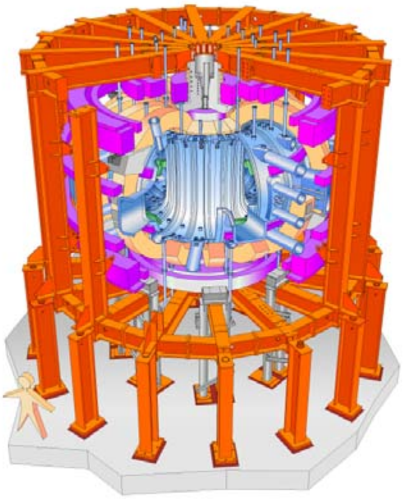

Figure 1.5: Sketch of ASDEX Upgrade

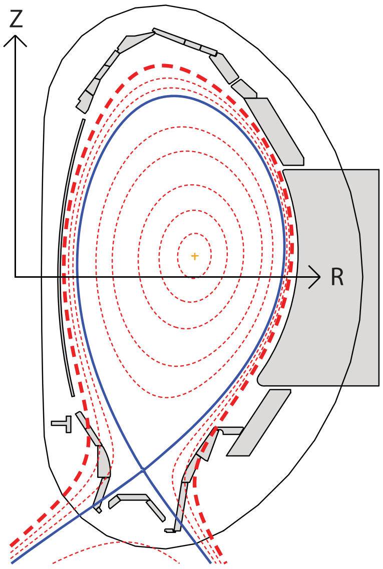

Figure 1.6: Reconstruction of flux surfaces

ASDEX Upgrade: This work was done at the Max-Planck-Institut for Plasma Physics in Garching, Germany. Since 1991 this institute runs the ASDEX Upgrade (Axial Symmetric Divertor EXperiment) fusion device (see figure 1.5). It is a full tungsten device with a poloidal divertor. Typical discharges last about 10 s and have a toroidal plasma current of about 1 MA. The magnetic field is about 2 T. The additional heating systems (neutral particle injection, ion cyclotron heating and electron cyclotron heating) can apply up to 27 MW to the plasma. With a typical plasma volume of 14 m^3 and a plasma mass of 3 mg it is a mid-size Tokamak in an international comparison. In figure 1.6 one can see the typical magnetic field configuration. The thin black line indicates the vacuum vessel containing the first wall, the grey elements. The red circles are the flux surfaces introduced in the "high-β Tokamak" paragraph. The Shafranov-shift, also introduced in that paragraph, leads to the outward shift of the inner flux surfaces, which results in a concentration of flux surfaces on the low field side. The separatrix, the blue solid line, marks the plasma boundary. The outer flux surfaces lead down to the divertor region of ASDEX Upgrade where the heat load is distributed on the divertor plates to protect the vacuum vessel, the built in heating systems and the diagnostics.[5]

1.3 Confinement modes

In the previous sections, the word “confinement” was often used, but never discussed in detail. One can derive different quantities for that purpose. One of them is the energy confinement time τ_E:

$$\tau_E = \frac{E_P}{P_V}. \tag{1.4}$$

E_P is the plasma energy and P_V is the total power loss of the system.[4] During a discharge the power loss has to be compensated either by auxiliary or by internal fusion α particle heating. High values of τ_E are favorable. The ratio of external heating P_{ext} compared to α particle heating P_α defines the Q value for a D-T-plasma:

$$\frac{P_{ext}}{P_\alpha} = \frac{5}{Q}. \tag{1.5}$$

The fact, that only one fifth of the fusion power is carried by alpha particles is already included in this definition.[1]

1.3.1 Transport processes

As already discussed, movement of charged particles perpendicular to magnetic field lines is strongly reduced. The remaining perpendicular transport can be separated in particle transport and heat transport. Therefore, the perpendicular particle transport coefficient D and the heat conductivity coefficient χ are introduced. In the following, an overview of different theories for determining these coefficients is given.

Classical transport: In a plasma with more than one particle and non-vanishing confinement time, there are particle collisions. These collisions lead to radial displacements in the order of one gyration radius $\vec{r}_g = \frac{m}{qB^2}\vec{v} \times \vec{B}$, if the mass differs significantly. Therefore, only electron-ion collision can cause radial transport. Together with the collision frequency ν_{ei} this defines the classical perpendicular particle transport coefficient [3]:

$$D_{c,ei} = r_g^2 \cdot \nu_{ei}. \tag{1.6}$$

Energy transport can also occur at inter species collisions

$$\chi_{ee} \approx \chi_{ei} \approx \chi_{ie} \approx \sqrt{\frac{m_e}{m_i}} \cdot \chi_{ii}. \tag{1.7}$$

The dominant heat transport is given by ion-ion collisions due to the large gyroradius.[2]

Neoclassical transport: The just presented transport coefficients do not include effects due to the magnetic topology of the plasma. In a Tokamak, the toroidal magnetic field is decaying with $1/R$, where R is the radial coordinate. Due to the invariant magnetic moment $\mu = \left(mv_\perp^2\right) / \left(2B\right)$, parallel velocity of particles, which is mainly toroidal, is

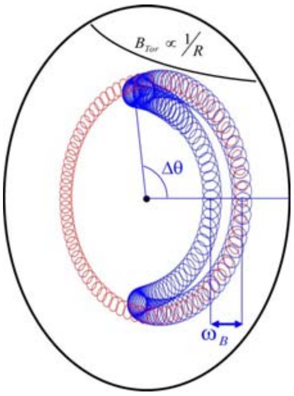

Figure 1.7: Schematic of free (red) and trapped (blue) particles[8]

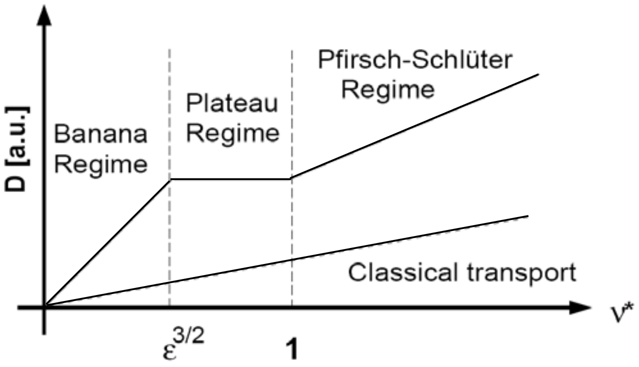

Figure 1.8: Neoclassic transport regimes[1]

converted to perpendicular velocity during their inward motion following the helically twisted magnetic field lines

$$\frac{v_{\parallel}^2}{v_{\perp}^2} < 2\epsilon, \qquad \text{with} \qquad \epsilon = \frac{r}{R}. \tag{1.8}$$

The points with vanishing parallel velocity are the return points in the Banana orbit. ϵ is the inverse aspect ratio of the Tokamak. In figure 1.7 [8], a sketch of the poloidal projection of the so-called trapped particles can be seen, but one has to bear in mind, that the leading component of the velocity is in toroidal direction. The width of these Banana orbits is determined by particle drift-motion caused by the gradient in the magnetic field. The radial excursion of trapped particles is larger than that of free particles, therefore the transport coefficients have to be adapted. Dependent on the fraction of the trapped particles and the increased displacement for each collision, a significantly higher radial particle transport is present in the plasma:

$$D_n \approx \frac{q^2}{\epsilon^{\frac{3}{2}}} D_c. \tag{1.9}$$

The safety factor q is a measure for the slope of the field lines (the number of toroidal circulations divided by the number of poloidal ones). This result is only valid, if the collision frequency is low enough that the particle can complete many banana orbits without collision.[3] Introducing the collisionality ν^* by normalizing the collision frequency to the time, a particle needs to finish a Banana orbit. The validity criterion for the transport coefficient derived above is given by $\nu^* < \epsilon^{\frac{3}{2}}$. For higher collisionalities the influence of trapped particles is reduced.

Anomalous transport: The use of the neoclassical transport theory has led to much more realistic calculations of transport processes than by simply using classical theory.

But there is still a discrepancy in calculation and experiment. The reason for this is, that in typical discharges the transport is dominated by turbulence, small, fast and strongly anisotropic fluctuations of most of the plasma parameters. The interested reader can find more information on this topic in chapter 2.5 and also for example in [9], [24], [25] and many other publications.

1.3.2 H-mode plasma, a motivation for this thesis

In 1980, a large step towards a fusion device was made. At the ASDEX tokamak (predecessor of ASDEX Upgrade), a new operational regime with strongly improved energy confinement was discovered. Due to the installation of a divertor and the application of sufficient heating power, the plasma switches from low-confinement mode (L-mode) into a so-called high-confinement mode (H-mode), which is characterized by steep gradients of density and temperature at the edge.[6] In an overview plot in figure 1.9 from ASDEX Upgrade, a typical L-H transition can be seen. In the first plot on the left side one can see, that during the flat top phase of the plasma current, there is a period of increased confinement triggered by switching on the electron cyclotron resonant heating system (ECRH). On the right side of this figure, a comparison of L- and H-mode radial edge profiles of the electron density and electron temperature is presented. The H-mode electron temperature profile shows a "pedestal" at the separatrix at $\rho_{pol} = 1.0$.[1] This leads to an offset for the core temperature which increases in L- and in H-mode with nearly the same slope. In the density profile, the top of the pedestal is outside of the measuring range of the Li-beam diagnostic, but in the time evolution on the left side, measured by a Deuterium-Cyanide interferometer (DCN), a clear jump can be seen by switching into H-mode. The formation of this so-called edge transport barrier (ETB) is the basis for nearly all scenarios of future fusion devices and the understanding of this plasma regime has advanced to one of the main topics in plasma physics, since it is not fully understood even 30 years after its discovery.

Edge transport barrier: A commonly accepted theory identifies a strong reduction of transport as reason for the steep gradients at the plasma edge. Due to a very localized change in certain plasma parameters, the high anomalous transport for ions is suppressed and the neoclassical transport χ_i becomes the leading process for the ion channel in this small shell within the plasma. It is assumed, that the formation of a strong shear in the radial electric field suppresses turbulent transport by tearing apart or tilt turbulent eddies.[46] This gives the radial electric field and its shear a key role in edge physics. Measurements with high spatial and temporal resolution are essential due to the narrow width ($\approx 2\,\mathrm{cm}$) of the transport barrier and the strong time dependence of the edge profiles, which is discussed in the next paragraph. At ASDEX Upgrade, lately, big effort was

---

[1] ρ_{pol} is a radial coordinate, which has a value of 1.0 at the last closed flux surface (see chapter 2.1).

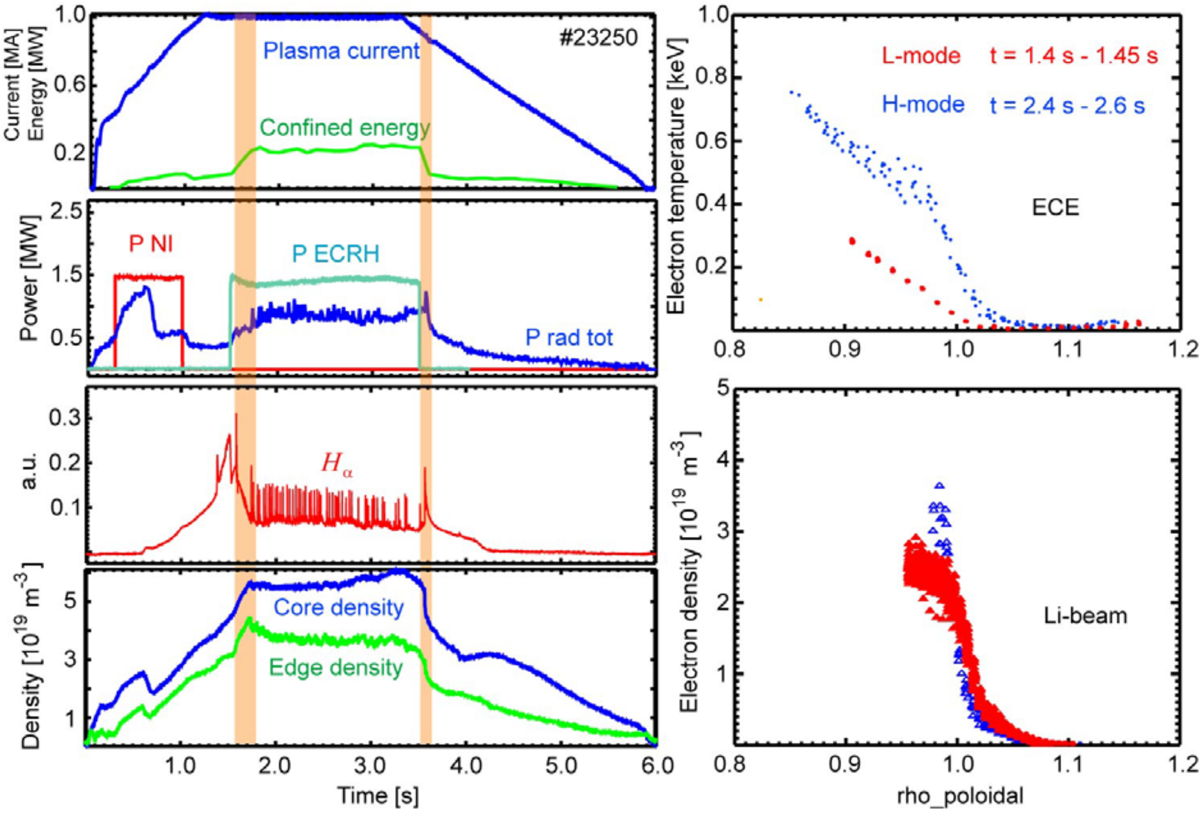

Figure 1.9: **Left:** Time traces of selected plasma parameters, in which the L-H transition and the H-L back-transition is marked by a yellow bar;
Right: Comparison of two radial edge profiles of L- and H-mode

put into improving the edge plasma diagnostics. Therefore, a new diagnostic of determining the radial electric field from passive He^+ line emission was implemented within the framework of this thesis, next to the already operating Doppler reflectometry system. While the doppler reflectometry system is designed to cover the whole plasma edge, the newly implemented method focuses on the small region containing the edge transport barrier.[26] One of the main goals of the new diagnostic is to investigate, whether the neoclassical predictions for the radial electric field agree with the measurements or not.

Edge localized mode: As mentioned just above, the edge profiles during H-mode have a strong time dependence. The reason for this is a periodic plasma edge instability called edge localized mode (ELM), which is not fully understood up to now. A short overview on commonly accepted findings is given in the following.
In the left graph of figure 1.10, one can see simulations by an edge stability code called ELITE for JET[2]-like plasmas [7]. It is shown, that the stable region for a given normalized

---

[2] The Joint European Torus (JET) is a fusion device, operated by Culham Centre for Fusion Energy in the United Kingdom.

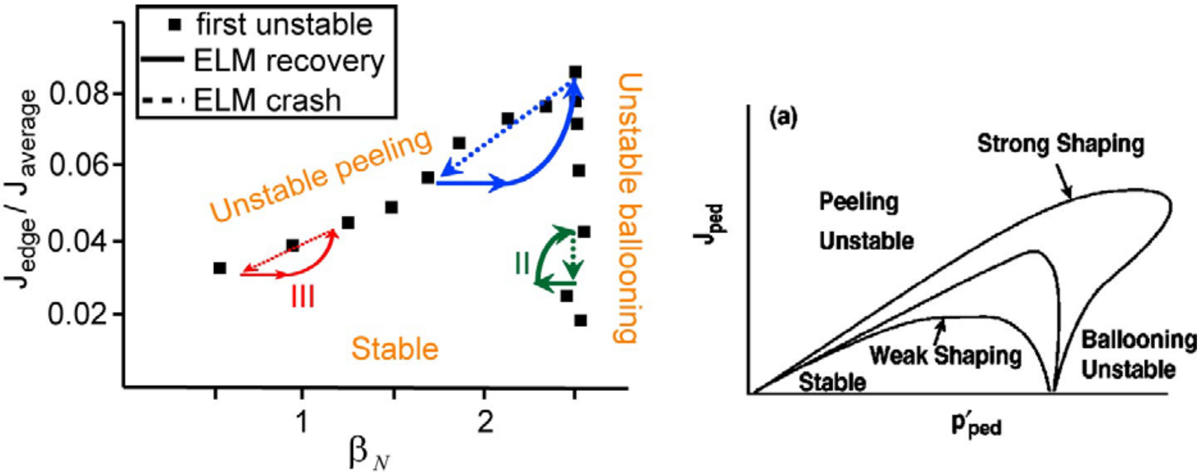

Figure 1.10: **Left:** Stability calculation for JET plasma together with simplified models of the ELM cycles of different ELM types [7]
Right: Variation of stability limits for different plasma shapes [7]

plasma β_N and the ratio of the edge current J_{edge} to the average current $J_{average}$ is limited on the one hand by the ballooning instability driven by the pressure gradient and on the other hand by the peeling instability driven by the plasma current. β_n is defined as $\beta_n = \beta a B / I$, where β is the plasma beta (see equation (1.3)), B is the magnetic field and I the total plasma current. The influence of stronger plasma shaping on these limits is shown in the right part of the figure. The limits are shifted to higher β_N and higher edge current. The development of plasma edge parameters is also illustrated in figure 1.10. Due to the continuous heating and the reduced transport, the edge gradients steepen up, resulting in an increasing plasma pressure and β. This leads to an increase of plasma edge current by the neoclassical bootstrap current[3], caused by the edge pressure gradient. For low β (red ELM cycle), the current limit is reached first and small Type III ELMs are triggered. Stronger heating reduces the ELM frequency. Further increase of heating power lead to large type I ELMs with increased frequency due to higher heating because of the ballooning limit. The small type II ELMs can only occur, if the current limit is not reached within the cycle. This is the case either for strong shaping or for high density and collisionality. A good indicator for ELMs is the H_α signal at ASDEX Upgrade, which is a measure for the particle flux to the divertor. During an ELM, the flux is significantly higher due to the collapsed transport barrier. This can be seen in the time evolution in figure 1.9. During H-Mode, the sharp peaks in this flux indicate the occurrence of ELMs. Affecting all plasma edge profiles and especially the radial electric field, which also collapses during an ELM, the time evolution of the analyzed plasma has to be correlated with the ELM cycle. This makes ELM synchronization to one of the leading topics within this work. A detailed discussion is presented in chapter 4.

---

[3] The bootstrap current is caused by the toroidal component of the banana orbits of trapped particles. In the presence of a radial pressure gradient, the particle density between neighboring Banana orbits slightly varies, which leads to a diamagnetic current. Friction forces due to collisions with passing particles amplify this effect.[12]

1.4 Contents of this work

The main task of this work is to analyze the radial electric field at the plasma edge at ASDEX Upgrade Tokamak. Therefore, a new method of measuring this field is presented, using passive He II emission. The basic principles of a magnetically confined plasma in a toroidal device was already discussed in this chapter. In the following two chapters, a closer look is taken on the essential theoretical topics for this work. Chapter 2 focuses on particle movement in a magnetically confined plasma, including the reconstruction of the confining magnetic field lines, the drift motion of charged particles and a basic over view on neoclassical theory. The atomic processes are discussed in chapter 3. A collisional-radiative model is presented, which is then used to model the observed emission line. Starting with chapter 4, the focus is shifted to the experimental part of the work. The plasma edge of ASDEX Upgrade and the most important diagnostics are introduced. Additionally the treatment of the ELMs, which is essential for edge physics, is discussed in detail. The presentation of the new radial electric field diagnostic is divided in chapter 5 and 6. While chapter 5 focuses on the experimental setup, chapter 6 gives an introduction to Bayesian statistics, on which the data evaluation is based. One first result, its accuracy and its sensitivity on other measurements and assumptions is discussed in the sensitivity study in chapter 7. The results are presented in chapter 8. This includes the effect of ELMs on the radial electric field, variations of different plasma parameters and the development of the E_r during an L-H transition. All results are compared to predictions from neoclassical theory. This work closes with a short summary of the main findings in chapter 9.

2 Particle movement

In the introduction of this work, a very short overview of the development of fusion devices was given. Within this scope some fundamental concepts in plasma physics, like flux surfaces or particle drifts were brought up, but were not discussed in the required depth, necessary for this work. The following chapters will pick up selected topics and go into more detail, starting with the movement of a single particle and its underlying forces in this chapter.

2.1 Coordinate system

As a starting point for discussing forces and velocities, a coordinate system has to be introduced. Due to the complex structure of a Tokamak, different sets of coordinates are required for the various physical effects.

Full 3D coordinates: The most general coordinate system without any implicit simplifications is a full 3D coordinate system (X, Y, Z). As origin, the center of the torus is chosen, with an upwards pointing Z-coordinate. Figure 2.1 a) shows a top view of the torus, illustrating the orientation of the X- and Y-axis. The vacuum vessel of ASDEX Upgrade is divided in 16 sectors also marked in this figure. By defining the X-axis on the border-line between sector 1 and 16 and the Y-axis perpendicular to it, an orthogonal coordinate system is created. Additionally, port 9 is highlighted in yellow, in which the optical head, used in this work, is mounted.

Simplified 2D coordinates: One basic feature of Tokamak devices is rotational symmetry in toroidal direction (φ in figure 2.1 a)). Therefore, a 2D coordinate system (R, z), shown in figure 2.1 b) can be set up defined by the following coordinate transformation:

$$X = R\cos\varphi \tag{2.1}$$

$$Y = R\sin\varphi \tag{2.2}$$

$$Z = z, \tag{2.3}$$

if φ is held fixed. In order to allow three dimensional intersection calculations required for line of sight integration, a third dimension t normal to R and Z, is added.

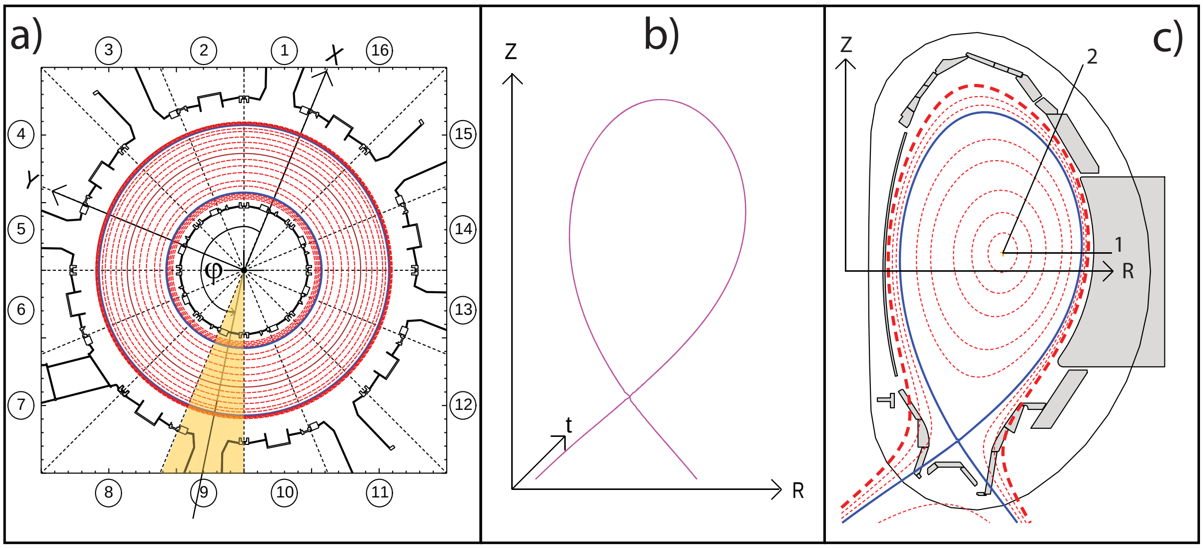

Figure 2.1: a) Top view of the torus vessel with Z coordinate pointing upwards;
b) The rotational symmetric 2D coordinate system with a sketch of the Separatrix (purple);
c) Sketch of AUG vessel with flux surfaces (red) and Separatrix (blue); line1 and 2 visualize the different spacing of the flux surfaces at different positions

1D flux surface coordinates: As already mentioned in the introduction, most plasma parameters are constant on flux surfaces, which can be identified by the normalized poloidal radius ρ_{pol}:

$$\rho_{pol} = \sqrt{\frac{\Psi_p - \Psi_0}{\Psi_S - \Psi_0}}. \tag{2.4}$$

Ψ_0 represents the poloidal flux on the magnetic axis (this means the center of the plasma) and Ψ_S is the flux at the separatrix[4]. Normalizing the poloidal flux Ψ_p at the given flux surface, a 1D coordinate is defined which varies from 0.0 at the plasma center to 1.0 at the separatrix and > 1.0 in the scrape-off layer. The radial plots in figure 1.9 presented in the introduction already utilized this coordinate system.
An impression of the distribution of the flux surfaces at ASDEX Upgrade is given by figure 2.1 c). The closed flux surfaces, confining the plasma, are separated from the open ones, leading the escaping particles to the divertor by the separatrix (plotted in blue). Additionally, two linear paths 1 and 2 are also included in the figure to illustrate the fundamental difference between the first two coordinate systems, compared to this one. If one chooses equidistant grid points in the three dimensional and two dimensional systems, they would not be equidistant in ρ_{pol}. Therefore, to be consistent, coordinate transformations to other coordinate systems are always done on the mid plane (path 1)

---

[4] The separatrix is the last closed flux surface (see blue line in figure 2.1 c). It separates the confining flux surfaces from the open ones in the so-called scrape-off layer (SOL). The separatrix can have one or two X-points. The lower single null configuration (LSN) has one X-point in the lower divertor chamber and the upper single null configuration (USN) has one X-point in the upper divertor.

and gradients are never calculated in ρ_{pol} in this work.

2.2 Equilibrium reconstruction

Until now, the equilibrium, which includes the shape and position of flux surfaces in a plasma is assumed to be known, but it is a complicated task to calculate the exact trajectories of the magnetic field in a Tokamak. In plasma physics, a simplified set of equations was derived, called ideal magneto-hydro-dynamic (MHD), with main focus on the magnetic geometry and the macroscopic equilibrium. Mass, momentum and energy conservation is included as well as Ohm‘s law and the Maxwell equations to account for the strong magnetic field. A fluid model is used to describe the plasma, in which the plasma current $\vec{J}$ together with the magnetic field $\vec{B}$ is used to balance the pressure gradient ∇p:

$$\vec{J} \times \vec{B} = \nabla p. \tag{2.5}$$

The magnetic field itself can be split in a toroidal $\vec{B}_t$ and a poloidal $\vec{B}_p$ component, where the poloidal component using the axis-symmetric assumption of a Tokamak, can be expressed as function of the poloidal flux Ψ_p [4]:

$$B_R = -\frac{1}{R} \cdot \frac{\partial \Psi_p}{\partial Z} \qquad\qquad B_z = \frac{1}{R} \cdot \frac{\partial \Psi_p}{\partial R}, \tag{2.6}$$

which is defined as $\Psi_p = \int \vec{B}_p \cdot d\vec{A}$. In the stationary MHD equilibrium ($\frac{\partial}{\partial t} = 0$), the magnetic field $\vec{B}$ as well as the current $\vec{J}$ is perpendicular to the pressure gradient

$$\vec{B} \cdot \nabla p = 0 \qquad\qquad \vec{J} \cdot \nabla p = 0 \tag{2.7}$$

and therefore the pressure is constant on flux surfaces $p = p\left(\Psi_p\right)$ as well as the poloidal current $\vec{I_p}\left(\Psi_p\right)$. This leads to a second-order nonlinear partial differential equation, called Grad-Shafranov equation, which defines the axis-symmetric toroidal equilibrium [3]:

$$\triangle^* \Psi = -\mu_0 R^2 \frac{dp}{d\Psi} - F\frac{dF}{d\Psi} \qquad \text{where} \qquad F\left(\Psi_p\right) \propto \vec{I_p}\left(\Psi_p\right). \tag{2.8}$$

$\triangle^* \Psi$ is defined as the elliptic operator $\triangle^* \Psi = R^2 \nabla \cdot \frac{\nabla \Psi}{R^2}$. For a more detailed description on ideal MHD, the book ”Ideal Magneto-Hydro-Dynamics” from Jeffry P. Freidberg [3] is recommended.

At ASDEX Upgrade, the Grad-Shafranov equation is solved numerically for equilibrium reconstruction using the CLISTE (CompLete Interpretive Suite for Tokamak Equilibria) code.[10] It uses the given poloidal field coil currents and the limiter structures to adjust the free equilibrium parameters to match the measured data as close as possible. These are magnetic measurements and optionally kinetic profiles to constrain the pressure. MSE measurements of the local magnetic field can also be used to constrain the q-profile. Soft X-ray measurements can additionaly constrain the position of the plasma center.

In this work, the ρ_{pol}-coordinate and therefore the equilibrium reconstruction is intensively used for alignment of the radial profiles of different diagnostics (see chapter 4) and for mapping of radial profiles to the lines of sight (see chapter 6). Uncertainties in the equilibrium reconstruction therefore enter the calculations in this work at various points, which leads to very complex interdependencies that cannot be propagated consistently through the whole model. The impact on the results is explored by a sensitivity study presented in chapter 7.

2.3 Guiding-center approach

The trajectory of a charged particle within the strong magnetic field of a Tokamak is very complex. One possible simplification is to apply the guiding-center approach, mentioned in the introduction. The gyration of a particle around a field line with the gyro-radius r_g and the frequency ω_c

$$r_g = \frac{mv_\perp}{qB} \qquad\qquad \omega_c = \frac{qB}{m}, \tag{2.9}$$

due to the Lorentz-force, is separated from the movement of the center of the gyration. Being dependent on particle charge q and mass m, the gyration direction and radius differs for ions and electrons.

Parallel motion of the gyro-center: The movement of the gyro-center parallel to magnetic field lines is not affected by the Lorentz-force. Therefore, it can reach very high velocities. Following the helically twisted magnetic field lines, a particle can reach every position of a flux surface within a very short time[5]. This strongly reduces the ability to built up gradients within a flux surface, which is a result already discussed in the introduction and in section 2.2 from a different point of view.

Perpendicular motion of the gyro-center: At the first sight, there is no perpendicular motion of the gyro-center, due to the Lorentz-force. But if an additional force F is added to the system, a drift of the particles perpendicular to the field and the force with the constant velocity v_D arises:

$$\vec{v}_D = \frac{\vec{F} \times \vec{B}}{qB^2}. \tag{2.10}$$

In figure 2.2 a sketch of the driving mechanism is shown. The additional force F disturbs the gyration motion in such a way, that in one half of the rotation the gyro-radius is diminished by decelerating the particle (blue) and in the other half of the rotation, the gyro-radius is enlarged by accelerating the particle (red). This leads to a constant

---

[5] This is not valid for rational flux surfaces. The magnetic field lines in these surfaces close with themselves after a finite number of toroidal rounds.

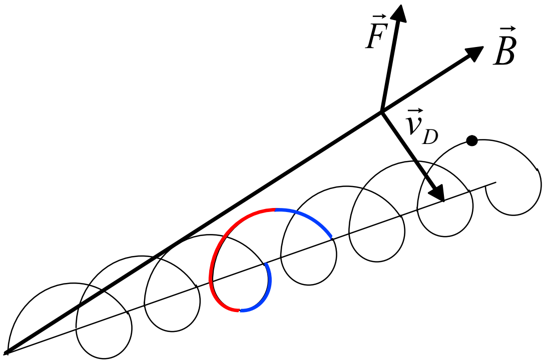

Figure 2.2: Illustration of drift motion

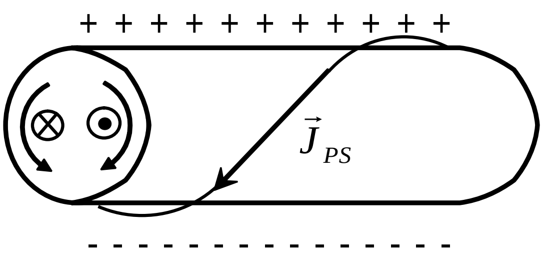

Figure 2.3: Sketch of Pfirsch-Schlüter currents

displacement of the particle after finishing one gyration and therefore to a motion with constant velocity perpendicular to the force F and the magnetic field.

∇B-drift: In a Tokamak, there are various forces which are superimposed to the magnetic field. The just introduced drift concept can be used to explore particle confinement in a Tokamak from the point of view of a single particle.
An important drift, inherent to all toroidal devices is the ∇B-drift. If parallel magnetic field lines, like the ones present in the θ-pinch, are bent to a torus, they get more dense to the center of the torus. On the one hand, this leads to trapped particles discussed in chapter 1.3.1 and on the other hand, it acts as a force $F = -\mu \nabla B$ on particles resulting in the ∇B-drift [2]

$$\vec{v}_D = -\frac{mv_\perp^2}{2qB^3} \nabla B \times \vec{B}, \tag{2.11}$$

where the magnetic moment μ of a particle, gyrating around a magnetic field line, is given by $\mu = \frac{mv_\perp^2}{2B}$. Due to the charge dependence, this drift would lead to charge separation in the case of a toroidal θ-pinch. But for a Tokamak with its helically twisted magnetic field, parallel compensation currents, the so-called Pfirsch-Schlüter currents arise to maintain the quasi neutrality. This is illustrated in figure 2.3. These currents are directed parallel to the magnetic field, due to the high parallel mobility of charged particles and the small poloidal component. They are oppositely directed on the high field side and the low field side of the torus.
In contrast to this drift which leads to the mainly toroidal Pfirsch-Schlüter currents, there are further drifts which cause mainly poloidal rotation. Therefore, these drifts are of high interest to the new E_r diagnostic, measuring poloidal rotation velocity.

$E_r \times B$-drift: The first mainly poloidal drift discussed here is caused by the radial electric field. Its origin is analyzed in detail in the next two sections:

$$\vec{v}_D = \frac{\vec{E}_r \times \vec{B}}{B^2}. \tag{2.12}$$

In the region with negative E_r and due to the negative magnetic field $\vec{B}$, a positive velocity is driven (ions and electrons move in positive z-direction on the low field side). As it will be shown later, this drift has a key position in deriving the radial electric field from the measurements of the poloidal plasma rotation.

Diamagnetic drift: A gradient in the temperature and the density can also cause a drift motion, called diamagnetic drift:

$$\vec{v}_D = -\frac{\nabla p \times \vec{B}}{qnB^2}. \tag{2.13}$$

Compared to the last two drifts, this is not a single particle effect due to a force acting on the gyro-motion, but it is a fluid-drift caused by the combined gyro-motion of all particles of one species in a volume element. In the presence of a density gradient, there are more particles gyrating in one direction with the gyro-center further inward, than in the other direction with the gyro-center further outward, leading to an apparent drift motion. The contribution due to the temperature gradient can be derived in the same way. Depending on temperature and density, this drift can differ strongly for different ion species. In the case of He^+-ions, which is not a fully ionized species, the particle pressure is rising looking from the scrape off layer to the center, until a maximal value is reached and then decreasing again. This leads to a change in the direction of the diamagnetic drift. The negative pressure gradient in the region further outward leads to a drift in negative z-direction. Regions further inward have a positive gradient leading to a positive drift velocity. This is in strong contrast to the diamagnetic drift of the main ions of the plasma. Fully ionized Deuterium typically drifts in the negative z-direction within the whole plasma due to a monotonically increasing pressure towards the plasma center.

Gradient in excitation probability: A similar effect compared to the diamagnetic drift is the drift caused by a gradient in the excitation probability. In the following chapter, electron impact excitation will be identified as the leading process causing the observed line radiation. In general one has to assume, that the excitation probability has a radial gradient, which leads to a “pseudo” particle drift. The reason for this is, that particles which are excited outside the observed volume element move into the volume element by gyration motion and then emit line radiation. Due to the gradient in the excitation probability, there are more excited particles gyrating through the observed volume element in one direction than in the other because the gyro-centers are on different radial positions. This leads to a shift of the observed wavelength and therefore to a “pseudo” drift velocity. In reference [11] this drift is discussed in detail. The apparent drift for the He^+ line is found to be negligible.

2.4 Transport theory

In the last section the drift motions were introduced, enabling particle motion perpendicular to the magnetic field due to gyro-motion. Also the consequences of this "classical" transport on toroidal confinement were discussed by introducing the toroidal Pfirsch-Schlüter return flows. Within this section a more formal approach is presented, which also includes effects from neoclassical theory and justifies the selection of drifts considered by the presented radial electric field diagnostic. Additionally, a theoretical prediction of the radial electric field can be derived. This section is based on the book of Helander [12] and also on considerations from the article of Hinton and Hazeltine [13]. A short outlook of possible corrections due to turbulence, which is neglected in the following considerations, is given in the next section.

In kinetic theory a partial differential equation called Boltzmann-equation is used to describe the number of particles within a spatial volume, centered at $\vec{r}$, and a velocity interval, centered at $\vec{v}$, by the density function $f = f\left(\vec{r}, \vec{v}, t\right)$:

$$\frac{\partial f}{\partial t} + \sum_{j=1}^{3} v_j \frac{\partial f}{\partial x_j} + \sum_{j=1}^{3} \frac{F_j}{m} \frac{\partial f}{\partial w_j} = \left(\frac{\partial f}{\partial t}\right)_{coll} . \tag{2.14}$$

The effects of magnetic confinement can be added by the $\left(\frac{\partial f}{\partial t}\right)_{coll}$ term, which includes particle collisions, and by including the Lorentz-force $\vec{F} = q\vec{E} + q\vec{v} \times \vec{B}$. E and B are the macroscopic averaged fields. Small scale fluctuations due to forces raised by atomic charges are moved to the collision operator $C\left(f\right) = \left(\frac{\partial f}{\partial t}\right)_{coll}$. Additionally, non-relativistic particle velocities are assumed. This leads to the Fokker-Planck equation [12]

$$\frac{\partial f_a}{\partial t} + \vec{V}_a \cdot \nabla f_a + \frac{q_a}{m_a}\left(\vec{E} + \vec{V} \times \vec{B}\right) \cdot \frac{\partial f_a}{\partial \vec{V}} = C_a\left(f_a\right), \tag{2.15}$$

where the subscript a is the particle species (e stands for electrons, i for ions and Z for impurity ions). The collision term C_a is a Fokker-Planck operator, which expresses the effect of Coulomb collisions. Therefore, it has to be defined as the sum over collisions with all other species within the plasma $C_a = \sum_b C_{ab}\left(f_a, f_b\right)$. The electric field vector $\vec{E} = -\nabla\Phi - \frac{\partial A}{\partial t}$ consists of a static, predominantly radial, electric field $\nabla\Phi$ and the time derivative of the vector potential $\frac{\partial \vec{A}}{\partial t}$, which is induced[6] by the magnetic field $\vec{B}_{OH} = \nabla \times \vec{A}$ of the ohmic transformer. $\vec{V}$ denotes the macroscopic fluid velocity, which is the average over the velocity $\vec{v}$ of all particles of a species at a certain point. Taking moments of the Fokker-Planck equation leads to equations for particle, momentum and energy conservation. The most important one for deriving the radial electric field is momentum conservation which is given in [12]:

$$\frac{\partial}{\partial t} m_a n_a \vec{V}_a + \vec{\nabla} P_a + \nabla \cdot \vec{\pi}_a - q_a n_a \left(\vec{E} + \frac{1}{c}\vec{V}_a \times \vec{B}\right) = \int d^3 \vec{m}_a \vec{v}_a C\left(f\right). \tag{2.16}$$

---

[6] The ohmic transformer is the only source from a neoclassical point of view. But there are also turbulent fluctuations of A, which can produce electric fields.

The first term on the left side of the equation accounts for inertia of the plasma particles, the second one is the force driven by the pressure gradient, the third term arises due to viscosity between the different species and the last one is the Lorentz-force. These are balanced by the friction force due to Coulomb collisions.

2.4.1 Radial force balance equation

A possible candidate for being a source of the radial electric field might be a difference in radial particle flux of electrons and ions. An expression for the perpendicular particle velocity can be directly derived from the momentum equation by taking the cross product with the magnetic field $\vec{B} = \vec{b} \cdot B$ [12]:

$$\vec{V}_{a\perp} = \frac{\vec{E} \times \vec{B}}{B^2} + \frac{1}{(m_a n_a \Omega_a)} \vec{b} \times \left[\vec{\nabla} \cdot P_a + \nabla \cdot \pi_a - \vec{R}_a + m_a n_a \left(\frac{\partial}{\partial t} \right) \vec{V}_a \right]. \tag{2.17}$$

The friction forces due to particle collisions are summarized by the $\vec{R}$ term and $\Omega_a = \frac{q_a B}{m_a}$ is the cyclotron frequency of the species. In lowest non vanishing order, $\vec{V}_{a\perp}^{(1)}$ is only poloidal (θ), given by $E \times B$- and diamagnetic drift motion:

$$\vec{V}_{a\perp}^{(1)} = \frac{\vec{E}^{(0)} \times \vec{B}}{B^2} + \frac{\vec{B} \times \nabla P_a^{(0)}}{m_a n_a^{(0)} \Omega_a B}. \tag{2.18}$$

The viscosity term can be neglected, if the particle distribution function f_a is close to a Maxwellian, which is always fulfilled, if closed flux surfaces are formed. Assuming a small collision frequency compared to the cyclotron frequency, collisions do not disturb the gyration motion of the particles and the friction force $\vec{R}$ can also be neglected. Inertia is small due to low velocities compared to thermal speed. Due to the fact that lowest order electric field $E^{(0)} = -\nabla\Phi$ and pressure $P^{(0)}$ are constant on flux surfaces and therefore directed radially, these flows remain within one flux surface. They do not contribute to radial transport. Equation (2.18) is the radial force balance equation:

$$V_\varphi B_\theta - V_\theta B_\varphi = \vec{V}_{a\perp}^{(1)} B = \frac{\partial p_Z}{q_Z n_Z \partial r} - E_r. \tag{2.19}$$

In literature on radial electric fields this equation is extensively used. By measuring the poloidal and toroidal rotation velocity profile, the radial electric field can be calculated, if density and temperature profiles of the observed impurity species Z are known. Active charge exchange recombination spectroscopy is often used to obtain the required profiles.

2.4.2 Radial particle transport

The question, if the presence of a radial electric field is connected to a difference in radial particle flux of electrons and ions, raised in the last section, could not be answered by analyzing lowest order perpendicular flows. The reason for this was, that these flows are purely poloidal and therefore do not contribute to radial particle transport. Looking at the next higher order, the perpendicular flow $\vec{\Gamma}_{a\perp} = n_a \vec{V}_{a\perp}$ is given by

$$\vec{\Gamma}_{a\perp} = n_a \vec{V}_{a\perp} = n_a \vec{V}_{a\perp}^{(1)} + n_a \vec{V}_c + n_a \vec{V}_{nc} + O\left(\delta^3\right), \tag{2.20}$$

$$\vec{\Gamma}_a^c = n_a \vec{V}_c = -\frac{1}{m_a \Omega} \vec{b} \times \vec{R}_\perp, \tag{2.21}$$

$$\vec{\Gamma}_a^{nc} = n_a \vec{V}_{nc} = \frac{1}{m_a \Omega} \vec{b} \times \left[\vec{R}_\parallel - q_a n_a \vec{E}^{(1)}\right], \tag{2.22}$$

where $\vec{b}$ is a unit vector pointing in the direction of the magnetic field.[13] The first order electric field $\vec{E}^{(1)} = \vec{E} - E^{(0)} = -\frac{\partial A}{\partial t}$ is given by the induced part, due to the magnetic field of the ohmic transformer, where A is the vector potential. The total particle flow can be split up into three terms: The first order term derived in the last section, which does not have a radial component and two other radial terms, separated due to their driving mechanism. Viscosity and inertia are again neglected in this order.

Classical radial flow $\vec{\Gamma}_a^c$: Transport effects due to the gyration motion of particles are referred to as “classical” (see section 1.3.1). These effects are caused by different forces modifying the gyro-orbit. This leads to a drift perpendicular to the magnetic field and the applied force. As discussed in the last section, lowest order perpendicular particle flow is poloidal and stays within one flux surface (see equation (2.18)), resulting in a poloidal friction force

$$R_\perp^{\text{friction}} = \frac{m_e n_e}{\tau_e}\left(V_e^{(1)} - V_i^{(1)}\right) = \frac{p_i' - p_e'}{\tau_e \Omega_e} \tag{2.23}$$

between particles of different species due to the relative velocity. Driven by the ∇P term, it has an explicit dependency on the particle charge q. The electric field term does not contribute, because it is equal for all species. Additionally, a poloidal thermal force arises due to a temperature gradient:

$$R^{\text{thermal}} = \frac{3 n_e T_e'(r)}{2 \Omega_e \tau_e}. \tag{2.24}$$

Following [12], this leads to a radial particle flow of

$$\Gamma_e^c = \Gamma_i^c = -n_e \frac{T_e}{m_e \Omega_e \tau_e}\left(\frac{p_e' + p_i'}{p_e} - \frac{3}{2}\frac{T_e'}{T_e}\right), \tag{2.25}$$

which is identical for electrons and ions due to momentum conservation ($R_{ei} = -R_{ie}$) of particle collisions. This flow is intrinsically ambipolar and therefore it cannot be a drive for the radial electric field.

This does not change even if impurities are included, which drastically increase radial ion particle flux because impurity-ion collisions lead to higher poloidal friction forces:

$$\Gamma_i^c = -n_i \frac{T_i}{m_i \Omega_i \tau_{iZ}}\left(\frac{p_i'}{p_i} - \frac{T_Z}{Z T_i}\frac{p_Z'}{p_Z} - \frac{3}{2}\frac{T_i'}{T_i}\right). \tag{2.26}$$

Electron-ion collisions can therefore be neglected. Ambipolarity is again automatically guaranteed by momentum conservation. The increased outward drift of ions is canceled by an inward drift of impurities:

$$\sum_a \Gamma_a^c = e\left(\Gamma_i^c + Z\Gamma_Z^c - \Gamma_e^c\right) = 0. \tag{2.27}$$

Neoclassical radial flow $\vec{\Gamma}_a^{nc}$: "Neoclassical" effects are based on Banana orbits of trapped particles. The concept of particle trapping due to the radially decaying toroidal magnetic field has been already discussed in section 1.3.1. Due to the predominantly toroidal motion of trapped particles, neoclassical friction $R_\|$ is parallel to the magnetic field. It arises due to the fact, that particles of one species have opposite velocities in one half of the Banana orbit compared to the other half. Neighboring Banana orbits therefore lead to a friction, which is strongly dependent on the collisional regime. Using the Fokker-Planck equation and the parallel return flows of neoclassical theory, the friction force can be related to parallel pressure gradients, given by the first order term $P^{(1)} = P - P^{(0)}$. The origin of these parallel fluctuations is the deviation of the guiding-center distribution from a Maxwellian. Due to momentum conservation, the sum of these friction forces over all species has to be zero: $\sum_a \vec{R}_{a\|} = 0$. Therefore, this part of neoclassical cross field transport is automatically ambipolar and cannot contribute to the formation of the radial electric field.

The second term is related to an inward movement of the flux surfaces caused by the induced electric field $\frac{\partial A}{\partial t}$, called Ware pinch. Due to the conservation of toroidal canonical momentum, the bounce points of Banana orbits move with the flux surfaces. Thus, trapped particles move inward. Passing particles are accelerated in parallel direction by the parallel field, which leads to an outward drift due to toroidal momentum conservation. This effect cancels exactly the inward motion of the field lines. Passing particles therefore experience no drift due to the parallel electric field. The inward drift of the trapped particles is intrinsically ambipolar due to the quasi-neutrality of the plasma $\sum_a n_a q_a = 0$.

2.4.3 Parallel particle flux

After having analyzed the perpendicular particle flow in depth, no driving mechanism for a steady state radial electric field could be found due to the automatic ambipolarity. In the following it is shown, that the development of the radial electric field is driven by the parallel particle flow in the plasma.

The reason for the build up of parallel particle velocity is given by the continuity equation, a moment of the Fokker-Planck equation, in a steady state plasma. It requires a divergence free total particle velocity in first order [13]:

$$\nabla \cdot \vec{V}^{(1)} = \nabla \cdot \left(\vec{V}_{\perp}^{(1)} + \vec{V}_{\parallel}^{(1)} \right) = 0. \tag{2.28}$$

Therefore, in a toroidal plasma, parallel Pfirsch-Schlüter return currents have to arise (see section 2.3 for a descriptive derivation). First measurements of these currents may be presented in the paper of Pütterich et al.[18]. Just inside the separatrix, a strong increase of the toroidal ion velocity is observed, which might be attributed to Pfirsch-Schlüter flows.

Recalling first order perpendicular particle velocity (2.18) and combining it with (2.28) leads to an expression for the first order parallel velocity

$$n\vec{V}_{a\parallel}^{(1)} = \frac{\vec{B}}{B} \cdot \left(n\vec{V}_{a}^{(1)} \right) = -\frac{1}{m\Omega} I \left(\frac{dP_a^{(0)}}{d\Psi} + e\bar{n}\frac{d\Phi}{d\Psi} \right) + K\left(\Psi\right) B, \tag{2.29}$$

where $K(\Psi)$ is an arbitrary integration constant.[13] Solving this equation for the electric field gives no useful results due to the unknown function $K(\Psi)$. This problem can be solved by looking again at the Fokker-Planck equation (2.15). By reordering with respect to the gyro-radius and by averaging over the gyro-phase, the drift kinetic equation can be derived:

$$\frac{\partial \bar{f}}{\partial t} + \left(\vec{V}_{\parallel} + \vec{V}_{d} \right) \cdot \vec{\nabla} \bar{f} + \frac{e}{m} \left[\frac{\partial \langle \Phi \rangle}{\partial t} + V_{\parallel} E_{\parallel} \right] \frac{\partial \bar{f}}{\partial \epsilon} = C\left(\bar{f}, \bar{f}\right). \tag{2.30}$$

This is a basic equation in plasma physics and is discussed in detail in numerous papers and books, for example [12],[13] or [19]. $\bar{f}$ is the phase-space distribution of gyro-centers, where the bar indicates the gyro-phase average. The coefficient of $\vec{\nabla}\bar{f}$ is the velocity of the gyro-center and the last term on the left side is a measure for the rate of energy change of a gyro-center. In a toroidal confined plasma the drift velocities are given by

$$\vec{V}_d = \frac{\vec{E} \times \vec{B}}{B^2} + \frac{1}{\Omega} \vec{b} \times \left(\mu \vec{\nabla} B + V_{\parallel}^2 \vec{b} \cdot \vec{\nabla} \vec{b} + V_{\parallel} \frac{\partial \vec{b}}{\partial t} \right). \tag{2.31}$$

The first term is the drift due to the electric field, the second one is due to the radial decaying magnetic field, the third one due to the curvature of the magnetic field and the last one combined with the third one is related to acceleration. By Amperes law, the second and third term can be expressed by a pressure gradient.

Rewriting the drift-kinetic equation only in zeroth order

$$\vec{V}_{\parallel} \cdot \nabla \bar{f}_e^{(0)} = C_{ee}\left(\bar{f}_e^{(0)}, \bar{f}_e^{(0)}\right) + C_{ei}\left(\bar{f}_e^{(0)}, \bar{f}_i^{(0)}\right) \tag{2.32}$$

$$\vec{V}_{\parallel} \cdot \nabla \bar{f}_i^{(0)} = C_{ii}\left(\bar{f}_i^{(0)}, \bar{f}_i^{(0)}\right), \tag{2.33}$$

leads to a gyro-center motion, simply following the magnetic field lines. Solving these two equations in the rest frame of the ions moving with $\vec{V}_i$, it can be derived, that $\bar{f}_e^{(0)}$ and $\bar{f}_i^{(0)}$ have Maxwellian shape, which is constant along magnetic field lines with equal mean velocity. Therefore, $\vec{V}_{i\|}^{(0)} = 0$, because $\vec{V}_{i\|}$ is not constant along magnetic field lines (it contains the Pfirsch-Schlüter return flows).[13] For the ions the 0-th order solution is given by

$$f_i^{(0)} = N_i \left(\frac{m_i}{2\pi T_i(\psi, t)} \right)^{3/2} \exp\left(-\frac{m_i \bar{\epsilon}}{T_i(\psi, t)} \right), \tag{2.34}$$

$$\text{where} \qquad N_i = n_{i,0}(\psi, t) \exp \frac{(Z_i e \langle \Phi(\psi, t) \rangle)}{T_i(\psi, t)}. \tag{2.35}$$

As expected, the zeroth order parallel velocity does not depend on the radial electric field, because drift velocities are neglected (compare equation (2.29)). The first order drift kinetic equations can be written in the following way:

$$\vec{V}_\| \cdot \nabla \bar{f}_e^{(1)} - \left(C_{ee}^l + C_{ei}^l \right) \bar{f}_e^{(1)} = -\vec{V}_{de} \cdot \nabla \bar{f}_e^{(0)} - \left(\frac{e}{T_e} \right) V_\| E_\| \bar{f}_e^{(0)}, \tag{2.36}$$

$$\vec{V}_\| \cdot \nabla \bar{f}_i^{(1)} - C_{ii}^l \bar{f}_i^{(1)} = -\vec{V}_{di} \cdot \nabla \bar{f}_i^{(0)}. \tag{2.37}$$

The collision operators have been replaced by linearized collision operators marked by a superscript l, in order to simplify further calculations. By solving these equations, one can identify four thermodynamic forces in the electron case and two in the ion case, that pushes f away from its Maxwellian shape $f^{(0)}$. For $f_e^{(0)}$, this is the pressure gradient of electrons and ions, the temperature gradient of the electrons, the parallel electric field and the effect on electrons due to collisions with ions. For $f_i^{(0)}$, this is the ion temperature gradient and the effect on the ions of collisions with electrons. From equation (2.37), the first order parallel ion velocity is derived [13]:

$$V_{i,\|}^{(1)} = \left(\frac{V_{th,i}^2}{2\Omega_{i,p}} \right) \left(\frac{\mu_i}{h} - \left[\frac{\partial p_i}{\partial \rho} + \left(\frac{Z_i e}{T_i} \right) \frac{\partial \langle \Phi \rangle}{\partial \rho} \right] h \right). \tag{2.38}$$

It contains the parallel return currents (term in square brackets) necessary to make the total velocity divergence free (see equation (2.28)) and therefore related to perpendicular drift motion. Furthermore, the two thermodynamic forces add a divergence free part (first term) due to friction forces. Applying the "weak-coupling approximation", which neglects the effect of electron-ion collisions on the ions, μ_i is given by the flux created by the ion temperature gradient

$$-\left(\frac{T_i}{Z_i T_e} \right) \mu_i \simeq -\left(\frac{T_i}{Z_i T_e} \right) (\beta_1, g_{2i}) \frac{\partial \ln T_i}{\partial \rho}, \tag{2.39}$$

where (β_1, g_{2i}) is the corresponding transport coefficient. In figure 2.4, the parallel force on passing ions due to friction with trapped ions is visualized in a poloidal projection. Due to the temperature gradient, two neighboring trapped particles (blue and green) have different energies. The energy dependence of the collision cross section leads to a toroidal force on the passing ion (red).[20] Dependent on the collisional regime, the resulting flux can be positive or negative due to the varying transport coefficient. In [13]

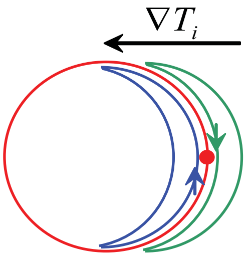

Figure 2.4: Poloidal projection of the parallel ion motion: The force due to friction of trapped ions (blue, green) on a passing ion (red) due to a temperature gradient is visualized

an approximation dependent on collisionality ν_* (see section 1.3.1) and plasma aspect ratio ϵ is given.

$$\text{Banana-plateau regime:} \qquad (\beta_1, g_{2i})_{bp} \simeq \frac{1.17 - 0.35\nu_{*i}^{1/2}}{1 + \nu_{*i}^{1/2} 0.7} \tag{2.40}$$

$$\text{Plateau-collisional regime:} \qquad (\beta_1, g_{2i})_{pc} \simeq \frac{(\beta_1, g_{2i})_{bp} - 2.1\nu_{*i}^2 \epsilon^3}{1 + \nu_{*i}^2 \epsilon^3} \tag{2.41}$$

The mean parallel ion velocity, averaged over a magnetic surface, can now be written as

$$\langle V_{i\|} \rangle = \langle V_{i,\|}^{(0)} + V_{i,\|}^{(1)} \rangle = \frac{cT_i}{Z_i q_i B_p} \left[(\beta_1, g_{2i}) \frac{\partial \ln T_i}{\partial r} - \frac{\partial \ln p_i}{\partial r} + \frac{Z_i q_i}{T_i} E_r \right], \tag{2.42}$$

where from now on, the radial electric field $\frac{\partial \langle \Phi \rangle}{\partial r}$ is labeled as E_r.

2.4.4 Parallel ion velocity

Knowing the average parallel ion velocity, equation (2.42) can be used to calculate the radial electric field from the ion temperature and density profiles. In the following it is assumed, that the parallel mean ion velocity $\langle V_{i\|} \rangle$ can be neglected compared to the other terms in equation (2.42), like it is done for instance in reference [22]. This lead to the following equation for the radial electric field:

$$E_r = \frac{T_i}{Z_i q_i} \left[\frac{\partial \ln p_i}{\partial r} - (\beta_1, g_{2i}) \frac{\partial \ln T_i}{\partial r} \right]. \tag{2.43}$$

In reference [14] it is shown by numerical simulations, that this equation is also valid at the plasma edge in the region of steep gradients even for vanishing toroidal ion velocities, which is the relevant region in this PhD work. This has to be shown explicitly, because the assumption, made during the derivation of (2.42) that the orbit width has to be small compared to the plasma gradients, is not given in this region. In the results part in

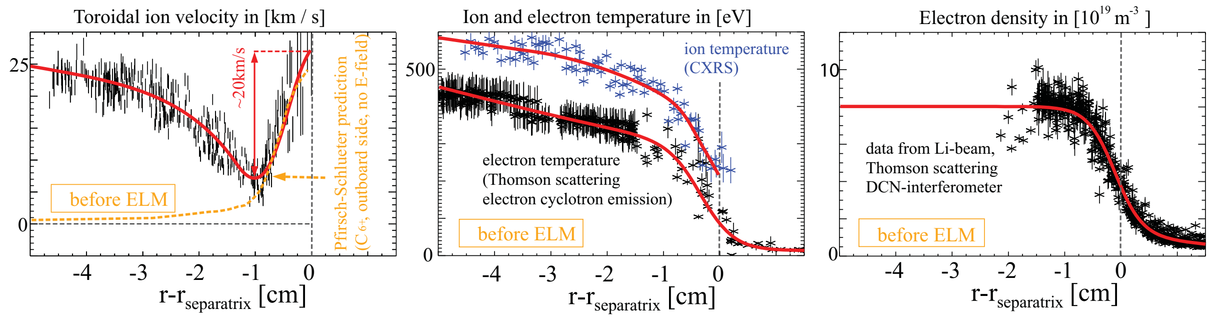

Figure 2.5: Edge toroidal ion velocity measured by charge exchange compared to Pfirsch-Schlüter return flows; the used electron and ion temperature as well as the electron density are also shown [18]

chapter 8 the neoclassical predictions are compared to measured data. This can be used to identify, if a vanishing mean toroidal ion velocity is justifiable and if the contribution due to the ion temperature and collisionality is significant or not.

Recent results at ASDEX Upgrade support this assumption. In reference [18] highly resolved toroidal ion velocity measurements by charge exchange spectroscopy have shown a dip in the velocity about 1 cm inside the separatrix (see figure 2.5). As suggested in the paper, the increase of the toroidal velocity towards the separatrix origins from the Pfirsch-Schlüter return flows. If this is correct, measurements on the high field side should show a velocity profile that should get negative in the region 1 cm inside the separatrix. The mean toroidal ion velocity then becomes small in the pedestal region at the plasma boundary and equation (2.43) describes the radial electric field in the edge transport barrier correctly.

2.5 Flows and turbulence

To close the discussion on transport, a short overview on turbulent effects and its interaction with the radial electric field is given. For example, in [23],[24] and [25] reviews on the actual understanding of turbulence are given. Also possible reasons for the transition from L- to H-mode are discussed, which are strongly related to this topic. As yet, no complete and widely accepted theory has been published.

In the introduction of this work the different concepts of particle and energy transport are mentioned. Starting from classical transport for linear confinement, curvature of magnetic field lines was introduced leading to neoclassical transport. Both theories fail in reproducing the measured transport coefficients. Only by allowing fluctuations in the electric and magnetic field, thus introducing turbulence, sufficiently high radial transport can be achieved. This anomalous transport is dominated by low frequency drift-wave fluctuations. Gradients in the density and temperature act as source for these collective oscillations due to the drift motion, caused by the gradients in combination with the magnetic field. Having to separate the motion of electrons and ions, these type of transport cannot be described by ideal MHD used for neoclassical calculations like the derivation of the radial electric field or the overview of plasma confinement in the introduction.[47] Another important phenomenon concerning turbulent transport are zonal flows, which at the edge can couple due to the curvature of the magnetic field and create flow oscillations called geodesic acoustic modes (GAMs). Both have zero poloidal ($n = 0$) and zero toroidal ($m \cong 0$) mode numbers and with a finite radial wave number. Turbulent fluctuations in the electric and magnetic field lead to layers of poloidal $E \times B$ velocity with opposite directions. The connection to drift waves is given by the “drift wave-zonal flow turbulence” theory, describing the energy transfer from drift waves to zonal flows. Not being able to drive radial flow, zonal flows cannot use radial gradients as energy source, but draw their energy from drift waves by modifying the wave vector, forming a self-regulating system.[48] A second mechanism which can drive zonal flows, is momentum exchange between the mean flow and the turbulence, called Reynolds stress.[23],[24]

A layer of sheared flows, which is created at the plasma edge by the steep gradients in the radial electric field, by zonal flows and also by Reynolds stress, can affect the just described turbulence in two ways. On the one hand, transport can be reduced by turbulence decorrelation and on the other hand, modes can be stabilized, which is summarized in [46]. In figure 2.6 one can see the impact of sheared flow on a turbulent eddy. The resulting deformation leads to a reduction in radial transport.[46] Furthermore, small eddies can be absorbed by the shear flow by extreme elongation, shown in figure 2.7 b) and thus leading to a self-amplification of the zonal flows. A decorrelation of large eddies, as shown in figure 2.7 a), which can not be directly absorbed by the sheared flow, may also have a key role in starting the self-amplification. However this is still under discussion, due to limited experimental evidence.[21]
Furthermore, in [24] it is shown that the turbulence for example by Reynolds stress, can have a feedback on the radial electric field, which was neglected in the discussion in the last section.

In the rest of this work, only neoclassical theory will be used for comparisons to the measurements. This is based on the assumption, that turbulent effects for the main ions are reduced in the H-mode transport barrier at the plasma edge. Good agreement of the predicted depth of the radial electric field with the measurements presented in the chapter 8 corroborates this assumption.

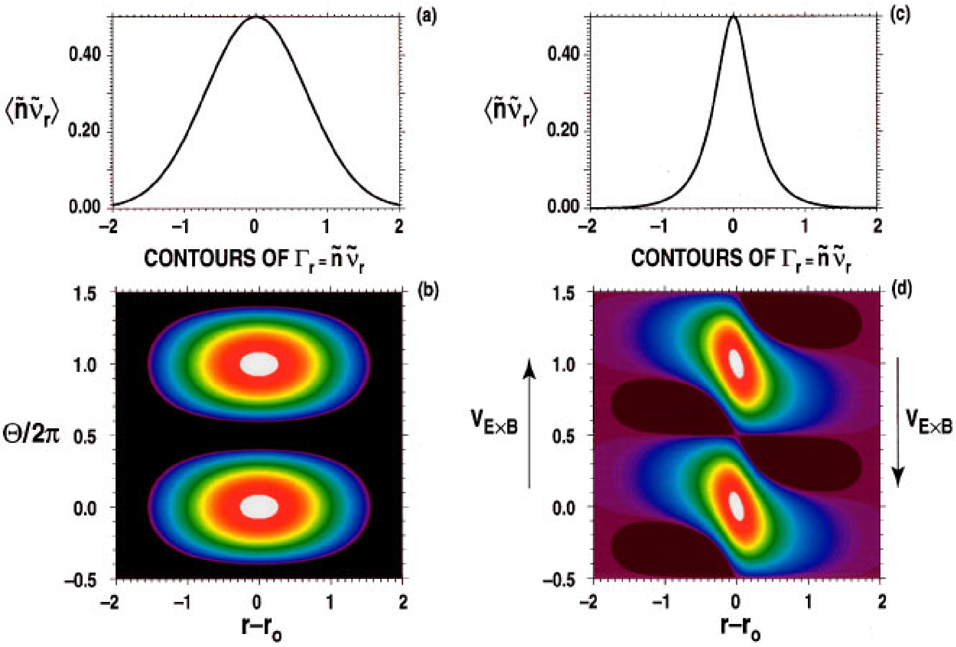

Figure 2.6: b) shows the color coded contours of turbulent radial flux in a cylindrical (r, θ) geometry; created by turbulent eddies, which couple with the background density profile; a) shows the radial flux averaged over the θ-coordinate; in c) and d) the transport reduction due to a shared velocity is visualized [46]

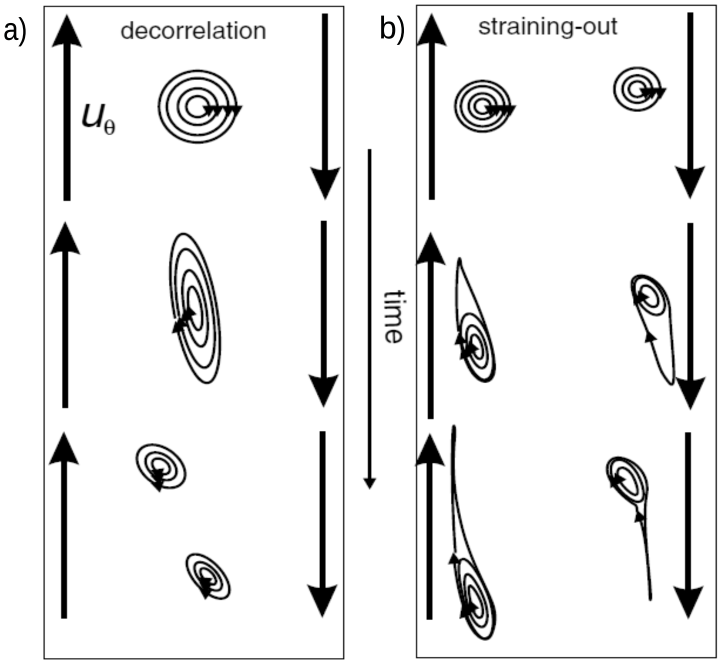

Figure 2.7: **Left:** Decorrelation of large eddies by sheared flow
Right: Small eddies are absorbed by the sheard flow [21]

3 Atomic physics

Having discussed particle motion in detail, the focus will now be shifted to the atomic processes within the plasma, which are responsible for plasma radiation. The E_r diagnostic, presented in this work, measures the passive line emission of He^+ at 468.57 nm and therefore depends strongly on atomic processes. The impact of these processes on line intensity, width and position will be explored.

3.1 Line emission

In order to calculate line radiation in a plasma, a collisional-radiative model is set up, which describes the transitions between the different ionization levels of one atom. It also covers excited states of ions and the transitions between them. The Max-Planck Institute for Plasma Physics, at which this work was done, is a member of the ADAS project (Atomic Data and Analysis Structure). Therefore, the ADAS cross-section data and the computer codes for modeling radiative processes in plasmas could be used. More information on this project is given on the homepage of the project: http://www.adas.ac.uk. In the following, the collisional-radiative model is presented on which all the utilized ADAS routines are based on.[34]

3.1.1 Collisional-Radiative model

Following reference [28], a basic approach of modeling atomic processes of impurities in a plasma is to use the coronal picture, which assumes low density and an optical thin plasma. Collisions of electrons e^- with impurity ions A of charge Z lead to excited ions A^* and radiation processes of these excited ions:

$$\begin{aligned} &\text{Impact excitation:} \qquad && e^- + A^Z \longrightarrow A^{Z*} + e^- \\ &\text{Spontaneous emission:} \qquad && A^{Z*} \longrightarrow A^Z + h\nu. \end{aligned}$$

Transitions between the different ionization stages are realized by including impact ionization with electrons and radiative recombination:

$$\begin{aligned}
&\text{Impact ionization:} && e^- + A^{(Z-1)} \longrightarrow A^{Z*} + e^- + e^- \\
&\text{Radiative recombination:} && A^Z + e^- \longrightarrow A^{(Z-1)*}.
\end{aligned}$$

In 1962, a paper was published [27], that presents an extension to the coronal approach to drop the condition of low densities, the collisional-radiative theory. It was extended a second time to the generalized collisional radiative theory in 1984 by McWhirter and Summers[29], to include the latest developments like divertor plasmas and high Z impurities. Now, the impurity atom A is separated into different ionization stages A^Z with the charge Z. Each stage A^Z is split into different levels of excitation A_i^Z, labeled by a subscript Roman letter. In this work, the impurity of interest is singly ionized Helium. From now on, all considerations are made for this species: $A^Z \rightarrow He^+$. Furthermore, collisions with the fully ionized plasma main ions are included. For the most cases at ASDEX Upgrade, this is fully ionized Deuterium D^+. The transitions within one ionization stage are given as follows:

$$\begin{aligned}
&\text{Impact excitation:} && e^- + He_i^+ \longrightarrow He_j^+ + e^- && (3.1)\\
& && D^+ + He_i^+ \longrightarrow He_j^+ + D^+ && (3.2)\\
&\text{Spontaneous emission:} && He_i^+ \longrightarrow He_j^+ + h\nu. && (3.3)
\end{aligned}$$

The level of excitation is increased by collisions with electrons and plasma main ions. Spontaneous emission decreases the level and lead to line radiation. In this work, the transition from $He_4^+ \rightarrow He_3^+$ was observed. The population of the ionization stages is determined by the following four processes:

$$\begin{aligned}
&\text{Impact ionization:} && e^- + He^0 \longrightarrow He_i^+ + e^- + e^- && (3.4)\\
& && D^+ + He^0 \longrightarrow He_i^+ + D^+ + e^- && (3.5)\\
&\text{Secondary ionization:} && e^- + He_i^+ \longrightarrow He^{2+} + e^- + e^- && (3.6)\\
& && D^+ + He_i^+ \longrightarrow He^{2+} + D^+ + e^- && (3.7)\\
&\text{Charge-exchange:} && He^{2+} + D^0 \longrightarrow He_i^+ + D^+ && (3.8)\\
& && He_i^+ + D^0 \longrightarrow He^0 + D^+ && (3.9)\\
&\text{Recombination:} && He^{2+} + e^- \longrightarrow He_i^+ && (3.10)\\
& && He_i^+ + e^- \longrightarrow He^0. && (3.11)
\end{aligned}$$

Impact ionization with electrons and plasma main ions act as a source for He^+, whereas secondary ionizations, which are also included have to be treated as a sink. Charge-exchange reactions with the main ions as well as recombination processes with electrons act as both, source and sink, for the population of He^+.

The key aspect of the collisional-radiative model is to find a balance between the radiative transitions, the effects due to collisions and the overall plasma parameters. By introducing rate coefficients R of collisions and time constants τ of radiative processes, the time evolution of such a system is determined. The populating processes of an ionization stage Z are given by:

$$\begin{aligned}\frac{d}{dt}N^{(Z)}_{i,pop} = \quad & N_{e^-}\sum_{j=1}^{m_{Z-1}} R^{ion}_{e^-}\left(Z-1\rightarrow Z, j\rightarrow i\right)N^{(Z-1)}_j \\ & + N_{D^+}\sum_{j=1}^{m_{Z-1}} R^{ion}_{D^+}\left(Z-1\rightarrow Z, j\rightarrow i\right)N^{(Z-1)}_j \\ & + N_{e^-}\sum_{j=1}^{m_{Z+1}} R^{rec}\left(Z+1\rightarrow Z, j\rightarrow i\right)N^{(Z+1)}_j \\ & + N_{D^0}\sum_{j=1}^{m_{Z+1}} R^{cx}\left(Z+1\rightarrow Z, j\rightarrow i\right)N^{(Z+1)}_j \\ & + \sum_{j=i+1}^{m_Z}\frac{N^{(Z)}_j}{\tau\left(j\rightarrow i\right)}.\end{aligned} \tag{3.12}$$

They are dependent on the electron and the two (neutral and fully ionized) Deuterium densities as well as on the densities of the ionization stage one above and one below of He^+. Due to the rate coefficients R, an additional temperature dependence is introduced. The depopulation processes can be written in an analog way:

$$\begin{aligned}\frac{d}{dt}N^{(Z)}_{i,depop} = \quad & N_{e^-}\sum_{j=1}^{m_{Z-1}} R^{ion}_{e^-}\left(Z\rightarrow Z+1, i\rightarrow j\right)N^{(Z)}_i \\ & - N_{D^+}\sum_{j=1}^{m_{Z-1}} R^{ion}_{D^+}\left(Z\rightarrow Z+1, i\rightarrow j\right)N^{(Z)}_i \\ & - N_{e^-}\sum_{j=1}^{m_{Z+1}} R^{rec}\left(Z\rightarrow Z-1, i\rightarrow j\right)N^{(Z)}_i \\ & - N_{D}\sum_{j=1}^{m_{Z+1}} R^{cx}\left(Z\rightarrow Z-1, i\rightarrow j\right)N^{(Z)}_i \\ & - \sum_{j=1}^{i-1}\frac{N^{(Z)}_i}{\tau\left(i\rightarrow j\right)}.\end{aligned} \tag{3.13}$$

These two sets of equations for the population and the depopulation are formulated using excitation level resolved rate coefficients. The last term in the populating and depopulating process is the radiative contribution. The populating term is given by the populating transitions from all excitation levels above and the depopulating term represents radiative transitions from the observed excitation level i to all below. The collision induced populating transitions between excitation levels are included in an analog way for electrons

$$\frac{d}{dt}N^{(z)}_{i,pop\_ex,e} = N_{e^-}\left[\sum_{j=1}^{i-1} R^{exc}_{e^-}\left(j\rightarrow i\right)N^{(z)}_j + \sum_{j=i+1}^{m_z} R^{de-exc}_{e^-}\left(j\rightarrow i\right)N^{(z)}_j\right] \tag{3.14}$$

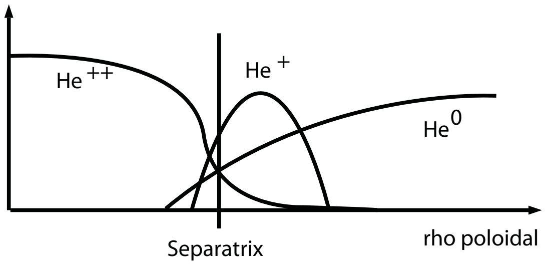

Figure 3.1: Sketch of emission shells

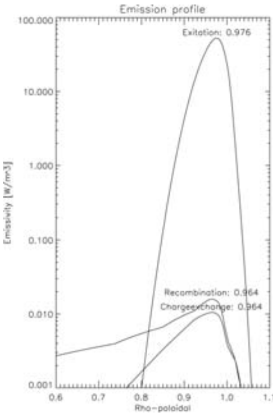

Figure 3.2: Comparison of different contributions to the emission profile

and for protons

$$\frac{d}{dt}N^{(Z)}_{i,pop\_ex,D} = N_{D^+}\left[\sum_{j=1}^{i-1} R^{exc}_{D^+}\left(j\rightarrow i\right)N^{(Z)}_j + \sum_{j=i+1}^{m_Z} R^{de-exc}_{D^+}\left(j\rightarrow i\right)N^{(Z)}_j\right] \tag{3.15}$$

consisting of impact excitation from lower levels and impact induced deexcitation from higher levels. The corresponding impact induced depopulation processes are

$$\frac{d}{dt}N^{(Z)}_{i,depop\_ex,e} = -N_{e^-}\left[\sum_{j=1}^{i-1} R^{de-exc}_{e^-}\left(i\rightarrow j\right) + \sum_{j=i+1}^{m_Z} R^{exc}_{e^-}\left(i\rightarrow j\right)\right]N^{(Z)}_i \tag{3.16}$$

for electron impact and

$$\frac{d}{dt}N^{(Z)}_{i,depop\_ex,D} = -N_{D^+}\left[\sum_{j=1}^{i-1} R^{de-exc}_{D^+}\left(i\rightarrow j\right) + \sum_{j=i+1}^{m_Z} R^{exc}_{D^+}\left(i\rightarrow j\right)\right]N^{(Z)}_i \tag{3.17}$$

for proton impact. In a stationary plasma, all these processes are in balance with each other.

3.1.2 Photon emission coefficients

As a result of solving the just presented radiative collisional model, so-called photon emission coefficients (PEC) were calculated. These coefficients are a measure for the number of photons emitted by a given transition, stored in PEC-files, separated by the emitting process. Together with the electron density and temperature profile as well as the He^+ density profile they are used to calculate the radial emission profile of the He II

line. In figure 3.1, an overview of the radial distribution of the different ionization stages of Helium is given.
In this work, the transition from He^+ (n=4) to He^+ (n=3) at a wavelength $\lambda_{4\rightarrow3} = 468.57\,\mathrm{nm}$ is measured. In the following, the population processes of the upper level are explored separately and rated for their importance concerning the emission profile.

Ionization: Starting the discussion from the outermost radial position, which is in the scrape-off layer, ionization of neutral Helium and Deuterium is the leading process (see equation 3.4). But only ionization with simultaneous excitation to the $n = 4$ level of simply ionized Helium acts as a direct source for the measured radiation process. The cross-section of this process is only $0.1\,\%$ of the cross-section of ionization, leaving the ion in the ground state.[31] Therefore, it is not directly contributing to the line emission but it acts as a source of He^+ ions (and also further inward He^{2+} ions).

Impact excitation: The next process gains importance near the separatrix with a sufficiently high density of free electrons n_e and He^+ ions n_{He^+}. By collisions He^+ ions are excited to the $n = 4$ level (see equation 3.1 and 3.2) and therefore contribute to the measured emission by:

$$\langle P\rangle = n_{He^+} \cdot n_e \cdot \mathrm{PEC}_{\mathrm{excit}}\left(n_e, T_e\right) \cdot E_{Ph}, \qquad E_{Ph} = \frac{hc}{\lambda_{4\rightarrow3}}. \tag{3.18}$$

Looking from the SOL inwards, the emission is increasing due to the rising amount of He^+, free electrons and free protons. Further inward it decays, because of the decaying He^+ density due to ionization to He^{2+}. A plot of the density and temperature dependence of the associated PEC is presented in figure 3.3.

Charge-exchange: Within the same radial region, where D^0, He^+ and He^{2+} exist simultaneously with a sufficiently high density, another process is possible, charge-exchange of neutral Deuterium with fully ionized Helium (see equation 3.8):

$$\langle P\rangle = n_{He^{2+}} \cdot n_D \cdot \mathrm{PEC}_{\mathrm{CX}}\left(n_D, T_D\right) \cdot E_{Ph}, \qquad E_{Ph} = \frac{hc}{\lambda_{4\rightarrow3}}. \tag{3.19}$$

The charge-exchange rate is strongly dependent on the excitation state of the neutral atom ($\propto n^4$). Using ADAS to model the relative population of the excited levels of Deuterium, which is dependent on electron temperature and density, charge-exchange of the (n=2) level of Deuterium is the leading process.[32]

Recombination: With increasing He^{2+} density, recombination processes (see equation 3.10) get more important. There is no sharp inner boundary, because only He^{2+} and

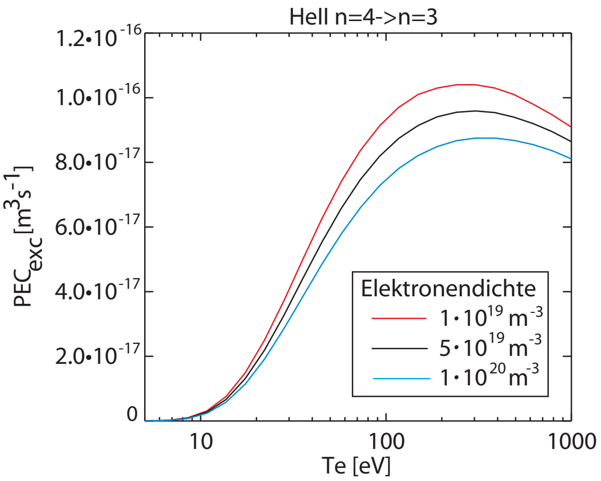

Figure 3.3: Electron temperature and density dependent electron impact photon emission coefficient of Helium for the $n = 4 \rightarrow 3$ transition

free electrons are required which exist in the whole plasma. Only the decay of the cross-section with increasing electron temperature leads to a reduction of emission towards the plasma center.

$$\langle P \rangle = n_{He^{2+}} \cdot n_e \cdot \mathrm{PEC}_{\mathrm{recom}}\left(n_e, T_e\right) \cdot E_{Ph} \qquad E_{Ph} = \frac{hc}{\lambda_{4\rightarrow3}} \tag{3.20}$$

Comparison: The importance of the different contributions to the emission profile is visualized in figure 3.2, which was created by a STRAHL run. The STRAHL code [33] is a one dimensional code to calculate the transport and emission of impurities. The contribution due to impact excitation is about four orders of magnitude higher than the contribution of the other two processes. To simplify the model and to decrease computation time only impact excitation is included in the model.

3.1.3 Passive spectrum

Having explored the emission profile, a model of the spectrum of the passive He II line was set up in the following way. The central wavelength was extracted from the NIST Atomic Spectra Database (http://www.nist.gov/pml/data/asd.cfm) and corrected for Doppler-shift due to the velocity of the He^+ ions discussed in the last chapter. The shape of the line was given on the one hand by a Gaussian shaped part due to Doppler-broadening depending on the He^+ ion temperature. And on the other hand by a Lorentz-shaped part, which is explained in more detail in chapter 6.2.1. This led to a Voigt-shaped line spectrum. Integrating these profiles along a given line of sight (LOS) resulted in the observed passive He II line spectra.

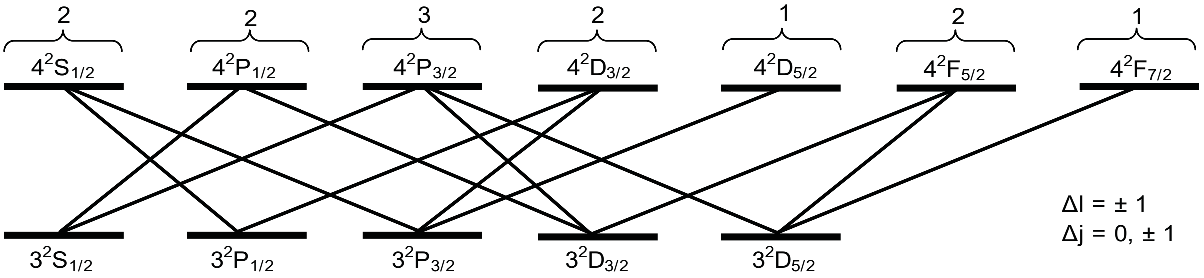

Figure 3.4: Line transitions from the n=4 level to the n=3 level, with respect to l-s coupling resulting in 13 transitions

3.2 Corrections

In the section just before, a very simple model of a passive line spectrum was presented. Before it could be applied to simulate the measured data, the effects of various corrections were investigated in order to check whether they can be neglected or not.

He II fine structure splitting: A more sophisticated atomic model of the He II ($n = 4 \rightarrow 3$) line transition identifies 13 separate transitions due to the fine structure splitting of the (l-s) coupled $n = 4$ level and the $n = 3$ level (see figure 3.4). A comparison of this exact model (red) to a simple[7] Gaussian one (blue) of the resulting emission spectrum is given in figure 3.5 (a) and (b). The ADAS database was used to extract the relative intensities and the positions of the single lines. The relative difference between the simple and the exact model in percent is plotted in green, where the maximal difference of the left and right wing is given separately as values. Sub-figures (a) and (b) show, that for increasing temperatures the deviation decreases. Also the asymmetry caused by the fine structure is strongly reduced for higher temperatures due to the effect of Gaussian-shaped Doppler-broadening of each line. The consequence of having neglected the fine structure is an increasing overestimation of the ion temperature towards the scrape-off layer. Fitting a Gaussian with free width to the line profile at 50 eV leads to an overestimation of 0.923 eV (1.8%). In the case of 30 eV the overestimation increases to 0.735 eV (2.45%). Using a Voigt-shaped line profile like it was done in this work does not change the overestimation of the temperature, because the difference in the relative positions of the single lines of the exact profile are smaller than the Doppler-broadening due to the temperature. A more serious problem arises from a temperature dependent shift of the central wavelength due to the fine structure, plotted in sub-figure (c). For temperatures below 50 eV, it has the same order of magnitude as the measured line shifts (see chapter 5).

---

[7] A Gaussian-shaped profile was assumed with a width defined by the temperature due to Doppler-broadening. The position and the amplitude was set equal to the exact model to simplify shape comparison.

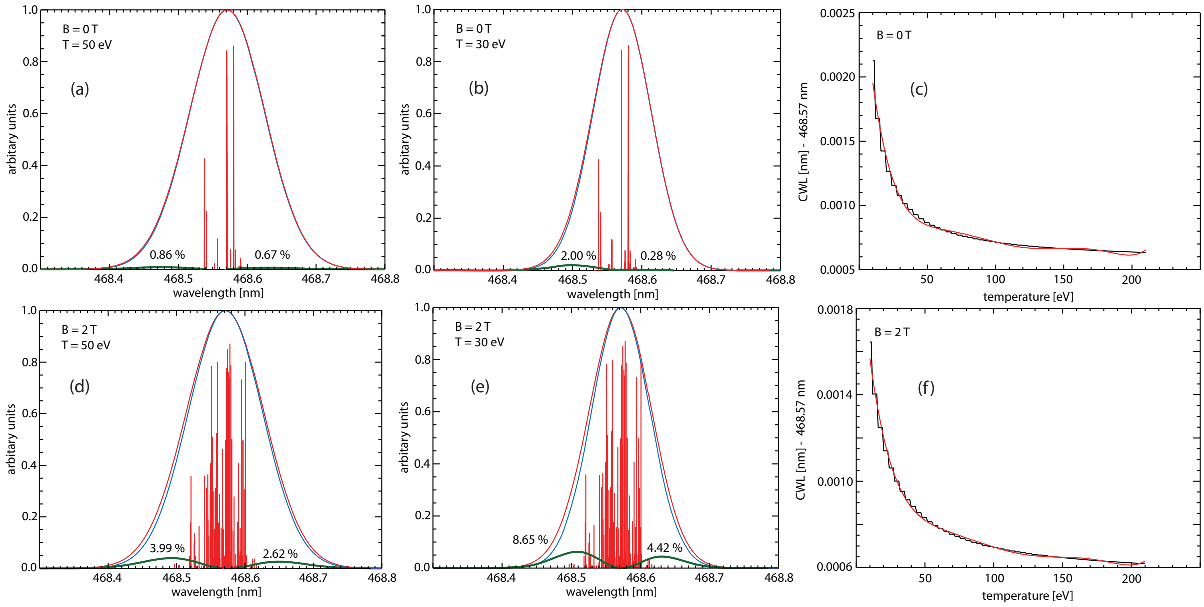

Figure 3.5: Comparison of Gaussian approximation (blue) to a combined line profile using fine structure splitting and Zeeman / Paschen-Back effect (red) for different temperatures and magnetic fields (a),(b),(d) and (e). The deviation is plotted in green. The viewing angle relative to the magnetic field is set to 80°. (c) and (f) show the deviation of the central wavelength to the tabulated value of 468.57 nm for both magnetic fields (black) and the spline fit (red).

Paschen-Back effect: Within a magnetic field, the shape of a line emission spectrum undergoes some major changes. These are strongly dependent on the strength of the magnetic field and the internal structure of the ion. The different regimes are called normal Zeeman-effect, anomalous Zeeman-effect and Paschen-Back effect (see figure 3.6). For weak magnetic fields (below 1 T) the Zeeman-effect is present. Dependent on the total spin S of the ion, normal Zeeman for $S = 0$ and anomalous Zeeman else, the line is split in symmetrically shifted σ- and unshifted π-components. For stronger magnetic fields, which are present at ASDEX Upgrade, the (l-s)-coupling within the ion is destroyed. This is called Paschen-Back effect. The selection rules ($\Delta m_s = 0$ and $\Delta m_l = 0, \pm 1$) allow only three possible types of transitions. Analog to the Zeeman effect, the unshifted one with $\Delta m_l = 0$ is called π-component and the two symmetrically up and down shifted ones with $\Delta m_l = \pm 1$, are called σ-components. The relative intensities of these components are dependent on the viewing angel compared to the magnetic field. For nearly perpendicular observation, which is relevant for this diagnostic (see chapter 5), all three components contribute with nearly equal weight, leading to a symmetric broadening of the He II line. In figure 3.5 (d) and (e) the effect of a 2 T magnetic field on the He II spectrum is shown for two different temperatures. Analog to the case with no magnetic field, sub-figures (a)

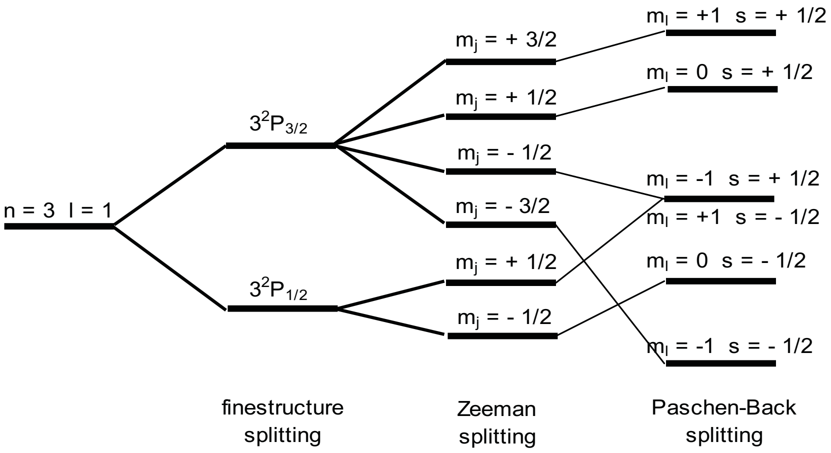

Figure 3.6: Splitting of the 6 degenerated states of the ($n = 3$, $l = 1$) level: $-l \leq m_l \leq l$, $m_s = \pm 1/2$. Fine structure splitting due to relativistic corrections: coupling of the angular momentum leads to two states $j = l \pm s$. Weak magnetic field: the $-j \leq m_j \leq j$ degenerated states are separated (Zeeman splitting). Strong magnetic field: (l-s) coupling is destroyed, nearly all states are separated (Paschen-Back effect).

and (b), one can see for both temperatures an asymmetric deviation from the Gaussian fit (blue). This leads to an overestimation of the temperature and a shift of the central wavelength. In the case of 30 eV, a free-width Gaussian fit causes a temperature of 37.6 eV, which is an overestimate of 25.3 %. This decreases for higher temperatures due to the increasing Gaussian shaped Doppler-broadening to 15.6 % in the case of 50 eV. Again, the introduction of a Voigt shaped line profile, like it is done in this work, reduces the temperature overestimate only marginally: in the 30 eV case to 22.3 % and in the 50 eV case to 13.4 %. The asymmetry of the left to the right wing is not as strong as for the case only with fine structure splitting, but due to higher number of lines and a wider distribution of their CWLs, higher temperatures are necessary to cover this effect by Doppler broadening. The CWL of a free Gaussian fit deviates from the tabulated value (see sub-figure (f)). Compared with the case without magnetic field, the deviation is reduced but still relevant in the region around 50 eV. In chapter 7, Sensitivity study, the effect on the estimated radial electric field will be discussed.

4 Diagnostics

The narrow region just inside the separatrix and all available radial profiles within this region are of great importance for the radial electric field evaluation. This pedestal region (see section 1.3.2) has a typical width of about 2 cm and is governed by steep gradients due to the reduction of anomalous transport in H-mode. In this chapter, an overview of the available edge diagnostics at ASDEX Upgrade is given and also the effect of ELMs on these profiles is discussed.

4.1 Edge diagnostics

As basis for the discussion on edge physics, the most important edge diagnostics are introduced. The experimental requirements due to the small spatial extent and the short time scales in this region are very high. But great effort during the last years has led to a variety of sufficiently accurate diagnostics and data evaluation methods.

Li-beam (electron density): One way of probing the plasma is to inject a radial beam of neutral Lithium atoms and measure the Li I (2p → 2s) line emission at 670.8 nm. Due to collisions, the neutral Li is ionized and confined by the magnetic field, which leads to a beam attenuation strongly dependent on the electron density, restricting the measurement region to the plasma edge. A relation to the electron temperature profile is not given, because of the negligible dependence of the excitation probability on it. With a spatial resolution of about 5 mm and a temporal resolution down to 50 μs, the pedestal of the electron density can be measured with sufficiently high resolution. [35], [36]

Electron cyclotron emission (electron temperature): The already discussed gyration of the electrons around magnetic field lines can be utilized to measure the plasma electron temperature. It is based on measurements of the cyclotron resonance frequency

$$\omega = \frac{eB}{m_e}, \tag{4.1}$$

which is radiated from these particles due to their accelerated circular motion. In the case of an optically thick plasma, continuous absorption and reemission leads to a black body like radiation profile, where the intensity is only dependent on the temperature. The necessary link to create a radial profile is given by the relation of the emission frequency and the radially decaying magnetic field. Highly resolved edge profiles can therefore be measured until the plasma becomes optically thin. In this "shine through" region too hot temperatures from further inward are measured.[37]

Thomson-scattering (electron temperature and density): An alternative method of determining the electron temperature and density is a Thomson-scattering system (TS). Its advantage is, that density and temperature are measured simultaneously at the same scattering volume, creating a link between the radial positions of these two profiles. The basic idea of Thomson-scattering is to inject a laser beam (Nd:YAG, 1 J pulse energy at 120 Hz up to 6 J at 20 Hz, pulse duration ≈ 4 ns) vertically into the plasma and measure the scattered light from electrons at different positions to get radially resolved profiles. Using a central beam, the complete area from the center to the plasma boundary is covered. For pedestal studies, higher resolution in the small region around the separatrix is required. Therefore, the beam can also be injected vertically at the low field side near the separatrix, reducing the radial coverage to $0.98 \leq \rho_{pol} \leq 1.1$ and thus increasing the resolution. The intensity of the scattered light is dependent on the number of electrons in the scattering volume, which can be used to calculate the electron density. From the same data, by analyzing the shape of the spectrum, the electron temperature can be calculated looking at the full width at half maximum.[38]

DCN interferometer (electron density): A third system for electron density measurements is available at ASDEX Upgrade. Five Deuterium CyaNide (DCN) laser interferometers are used to measure line integrated densities along the lines of sight visualized in figure 4.3. Due to the low spatial resolution, this system cannot be used as stand-alone diagnostic for profile reconstruction, but combining it with other diagnostics leads to more reliable result, because of the very accurate calibration of the interferometer system.

Charge exchange recombination (ion velocity and temperature): Additionally to the electron density and temperature profiles, the parallel velocity of the He^{+} ions is required for radial electric field determination. The He^{+} velocity is assumed to be equal to the impurity ion velocity, determined by charge exchange recombination spectroscopy (CXRS). Neutral Deuterium atoms, which penetrates the plasma deeply due to the high energy of the heating beam, collides with an impurity ion (e.g. He^{2+}, C^{6+}) and an electron from the Deuterium is transferred to the ion, leaving it in an excited state. The line radiation at a specific wavelength emitted by the decay of this exited state is detected. From the Doppler-shift and Doppler-broadening of this emission line the velocity and temperature of the impurity ion can be determined. The link between the velocity of

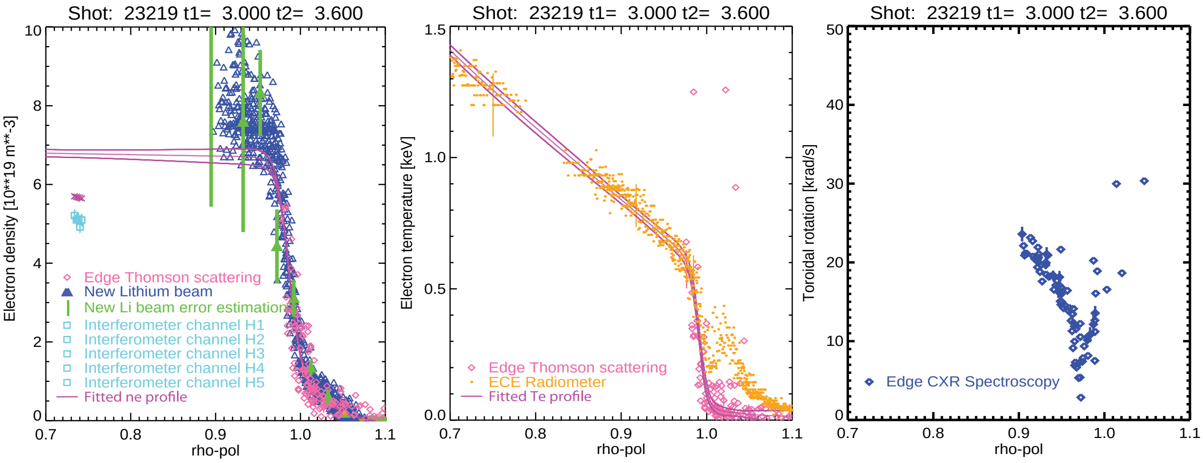

Figure 4.1: AUGPed fit of pedestal profiles (ELM synchronized)

different species is given by the assumption, that fully ionized impurities are in thermal equilibrium with the main ions of the plasma.[40] The edge CXRS system installed at ASDEX Upgrade has a sufficiently high resolution to resolve the small structures within the pedestal region, as discussed in detail in reference [39]. Typical ion velocity spectra show a minimum just inside the separatrix, as already mentioned in section 2.4.3 (see rightmost graph in the figure 4.1).

4.2 Combined profile reconstruction

Each of the just presented diagnostics covers only parts of the pedestal. By combining all profiles, benefiting from overlapping diagnostics, a complete set of highly resolved plasma edge profiles can be derived. Fitting these profiles with analytic functions is the basis of further edge research. For this purpose, a graphical tool called AUGPed was written by Lorne Horten. Within this program, profiles of different diagnostics are combined, clipped to trusted regions and corrected for radial displacements, arising from uncertainties in the absolute position and from equilibrium reconstruction. The profile fitting is done by adjusting the parameters of a hyperbolic tangent function which is extended by polynomials of order up to three at the inner and outer side of the strong gradient region. In figure 4.1 examples of combined edge profiles together with the AUGPed fits (purple) are presented. The alignment problem of the electron temperature is solved by shifting the profiles radially to match the 100 eV at the separatrix, as derived in [49]. The radial displacement of the Thomson-scattering data then defines the absolute position of the electron density profile, because Thomson-scattering as already discussed is measuring density and temperature simultaneously within the same scattering volume. At the pedestal top, there are no data from edge TS and the Li-beam is already largely attenuated. Therefore, the line integrated measurements from the DCN interferometers are included. Having no concrete radial position, the minimal ρ_{pol} value along the DCN

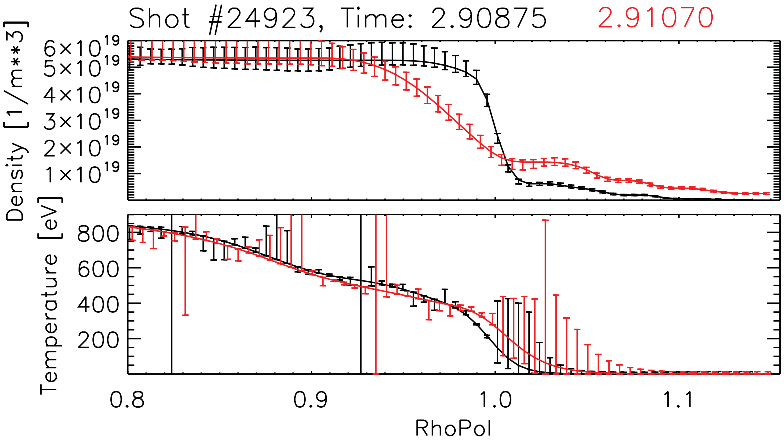

Figure 4.2: IDA pedestal profile fits, using Li-beam data, DCN interferometer data and ECE data red: during ELM; black: just before ELM

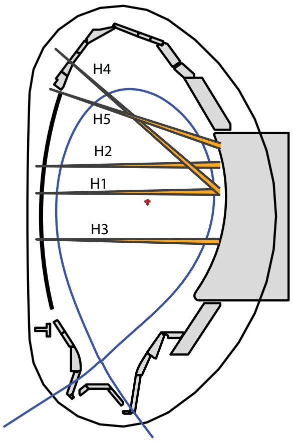

Figure 4.3: Positions of DCN laser beams

LOS is chosen for plotting. For comparison the line integration of the fitted profile is also plotted (purple crosses).

To ensure a sufficient amount of data points and due to the different time resolutions of the included diagnostics, AUGPed was only used on large time intervals (of about 100 ms). These time averaged, smooth profiles lead to very accurate and well aligned edge profiles. But this is also a disadvantage, if the evolution of edge profiles on small time scales has to be analyzed. Especially in an H-mode plasma, time averaging has to be done with great care due to ELM activity. The edge gradients change substantially within the ELM cycle (typical type-I ELM frequencies are about 50 - 150 Hz). Therefore, the ability of ELM synchronized time averaging was included in AUGPed. More detail on ELM synchronization is given in the next section.

An alternative way of creating combined pedestal profiles is to apply Integrated Data Analysis (IDA) to the measured data, which is presented in [41]. No time averaging of profiles is done, which leads to a time resolution of 1 ms, being sufficiently high to resolve the profile evolution during the ELM cycle. Only the Lithium beam data, the DCN interferometer data and ECE data have sufficient temporal resolution to be evaluated simultaneously on a millisecond time base. Thomson-scattering is excluded leading to large error bars in the shine through region of the ECE profile and a loss of relative alignment between electron density and temperature. In figure 4.2 typical profiles can be seen.

The aim of the two methods of edge profile reconstruction (AUGPed and IDA) is different. For time evolution analysis, for example L-H-transitions or comparison between two ELM cycles, it is beneficial to use the fast IDA profiles. The proper aligned AUGPed fits are better suited for comparisons of H-mode regions with different plasma parameters, for

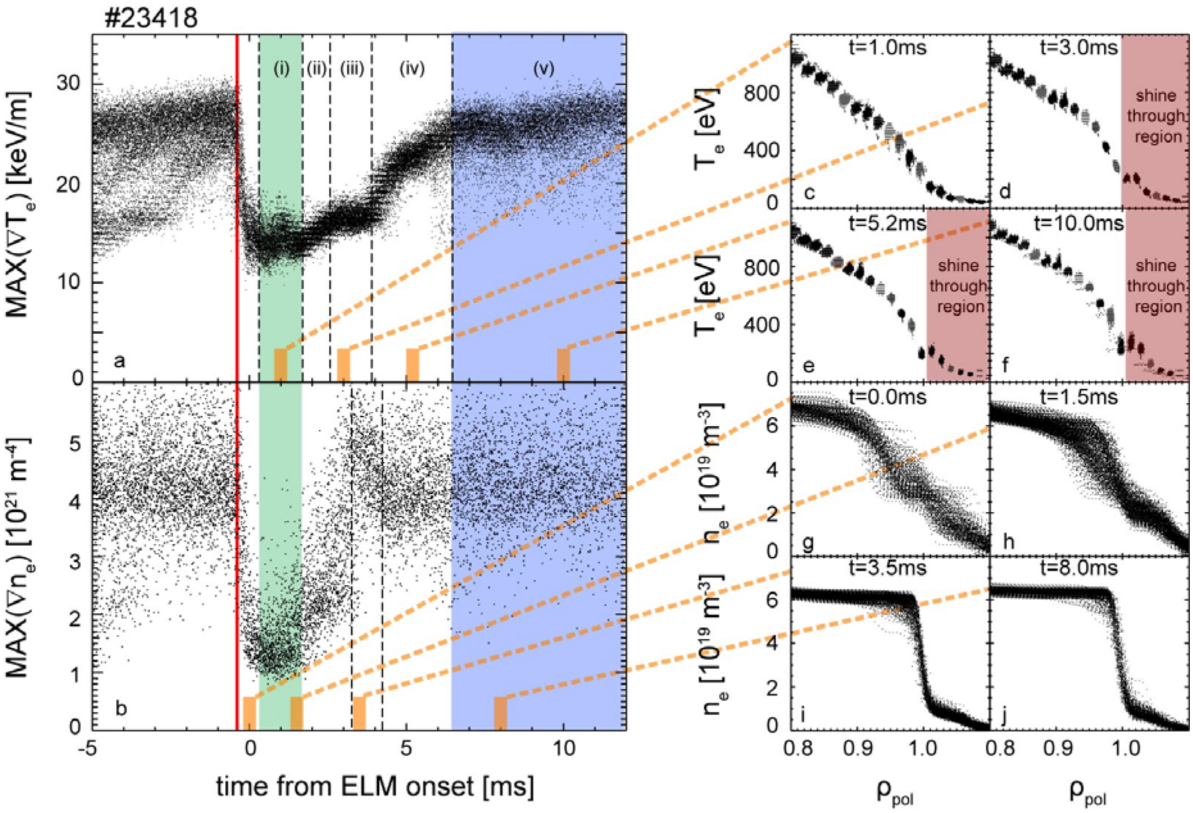

Figure 4.4: Time evolution of the gradients of electron temperature and density edge profiles [45]

example different heating or fueling. In chapter 8, it is clearly pointed out, which method was used to create the pedestal profiles required for electric field evaluation.

4.3 Consideration of ELMs

The edge profiles of a H-mode plasma, which were primarily analyzed in this work, are strongly influenced by the ELM cycle. In section 1.3.2, a short overview of the different types of ELMs and their driving mechanism was given. The gradients of the edge profiles are increasing due to reduced turbulent transport and continuous heating, until a stability limit is reached. Therefore, edge profiles are strongly time dependent. Looking at many different time points, the evolution of these profiles could be analyzed in reference [42] and [45]. One of the main results was, that the time evolution of the edge profiles is cyclical with respect to the onset of an ELM. Different states relative to the ELM-onset could be identified. In figure 4.4 this is visualized. The maximal gradients of the electron temperature and the electron density are plotted relative to the ELM-onset (red bar). Five regions in the evolution of the temperature gradient were identified. Therefore, data evaluation always has to be done relative to the onset of an ELM. Temporal averages over many ELM cycles, preserving the internal ELM structures, can only be realized by considering a narrow temporal region within each ELM cycle. This is shown in the eight small radial profiles on the right side of the figure. The yellow bars mark the origin of the data relative to the ELM cycle. Essential for this “ELM-synchronized time averaging” is a reliable method that identifies the exact time point of each ELM-onset during the discharge. At ASDEX Upgrade so-called ELM shot files are written, containing the start and end time point of every ELM during a discharge. The detection method is based on the algorithm presented in [43], which is now available in a rewritten and improved version by Andreas Burckhart. Different signals or a combination of them can be selected for ELM detection. The ELM shot files used within this work are based on the poloidal currents from shunt measurements in the outer divertor target plates.

The just presented method of “ELM-synchronized time averaging” was applied to all time averaging processes required for this work. In AUGPed, this feature is already built in, as mentioned in the last section. But it was also explicitly applied, if averaging over IDA edge profiles was necessary. Furthermore, mapping of radial coordinates with respect to the equilibrium reconstruction was done separately for each time step before the averaging took place. Therefore, it is also ELM-synchronized, which led to strongly reduced mapping uncertainties due to a radial displacement of the plasma during the ELM.

These highly resolved edge profiles, on ELM-cycle time scales, are a good basis to analyze the time evolution of the radial electric field within one ELM. According to neoclassical theory, discussed in detail in chapter 2, the deep well drastically reduced due to the breakdown of the temperature and density gradients (see equation (2.43)). Then, within the recovery phase of the gradients, the well in the radial electric field should deepen again until the stationary phase is reached. There, it should stay constant until the next ELM happens. Confirmation of this predicted behavior could be a good evidence for the assumption, that neoclassical transport is dominant in the pedestal region. Also the focus could be shifted to longer time scales. Is there a time evolution of ELM cycles during a constant plasma phase and is it related to the radial electric field? Also the transition between different plasma regimes could be of great interest like the development of the radial electric field and the associated ELM-cycles just after the L-H transition.

5 Experimental setup

In the last three chapters, selected topics of plasma edge physics were discussed in detail, to provide a basis for presenting a new diagnostic at ASDEX Upgrade. It aims for determining the radial electric field with high spatial and temporal resolution in the region around the separatrix. The experimental setup is described in this chapter, followed by detailed information on the evaluation process in the next chapter.

5.1 Diagnostic design

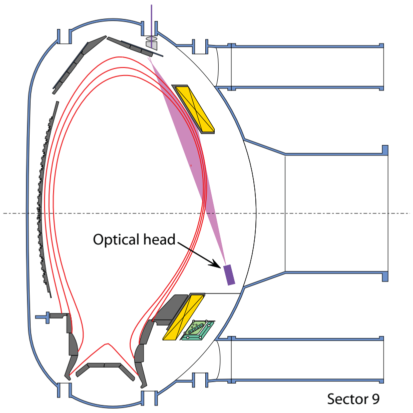

Figure 5.1: Setup of the diagnostic

The presented radial electric field diagnostic measures passive emission from He^+ ions at 468.57 nm. An optical head was used in sector 9 of ASDEX Upgrade (see figure 2.1, marked in yellow). A sketch of the poloidal cross section of this sector is given in figure 5.1, where the optical head and the lines of sight (LOS) starting from it are marked in magenta. The fiber endings are arranged in two parallel radial rows. 28 channels are installed on the left side and 27 on the right with a radial resolution of about 6 mm. 17 of them are connected to the analyzing spectrometers used for data acquisition. These two Czerny Turner spectrometer systems are called LIA and LIC. The focal length of the LIA spectrometer (JOBIN YVON) is $f = 0.75$ m, which is equipped with a 1200 l/mm grating and a fast EMCCD camera (RoperScientific MicroMax 512BFT) with 512 × 512 pixel. One pixel has a spectral coverage of 0.0175 nm. The camera can capture the spectra of 11

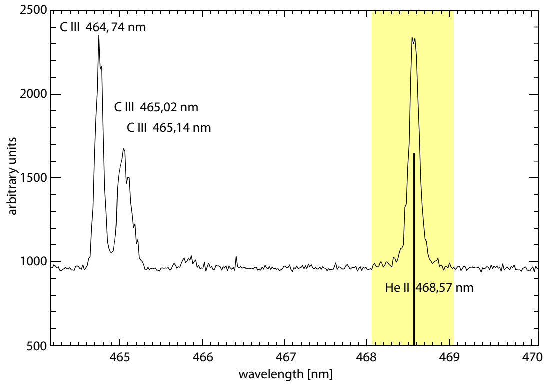

Figure 5.2: Typical spectrum measured by the LIA spectrometer

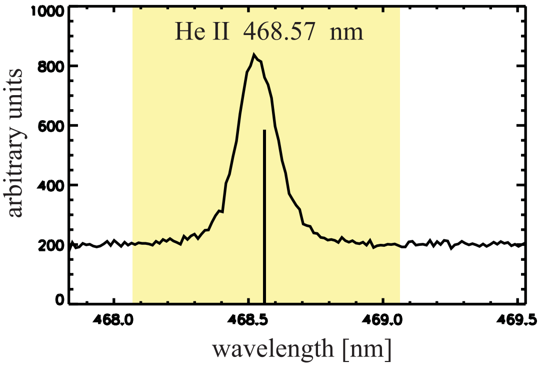

Figure 5.3: Typical spectrum measured by the LIC spectrometer

LOS with a time resolute of 4 ms, using hardware supported amplification and region of interest (ROI) binning. The second spectrometer (ACTON) is identical in focal length, but it is equipped with a 1800 l/mm grating and a different type of camera. Capturing the spectra of 8 LOS, the camera (MicroMax) has also a time resolution of 4 ms but only supports ROI binning. Due to the smaller number of pixels, 120, the spectral coverage of a pixel is only slightly increased compared to LIA. It is 0.0129 nm. Together, both spectrometers are capable of capturing 19 spectra simultaneously. One channel of each spectrometer is connected to a calibration lamp to improve the accuracy of the absolute wavelength calibration (more details will be given later in this chapter). Typical passive spectra measured by the two spectrometers, which are set to a central wavelength of $\lambda_c = 468.57\,\mathrm{nm}$, can be seen in figures 5.2 and 5.3. The most obvious difference is the different spectral coverage due to the finer grating of the LIC spectrometer. In the spectrum of the LIA spectrometer the neighboring carbon lines can be seen. Therefore, to avoid distortion of the calculated radial electric field and to save computation time, only a small region of the spectrum $468.57\,\mathrm{nm} \pm 0.5\,\mathrm{nm}$, marked in yellow, was used in the following.

Passive spectroscopic measurements, like the one described here, do not disturb or influence the plasma. Therefore, measurements for every discharge can be done, supported by a fully automated data acquisition and storage system. Due to the fact, that two other diagnostics are also using this system, measurements of the He II line are not available for all discharges. One of them is active charge exchange recombination measurements using the Li-beam to determine the ion temperature at the plasma boundary.[44] The other one is a passive method which can determine the electron temperature in the scrape off layer.

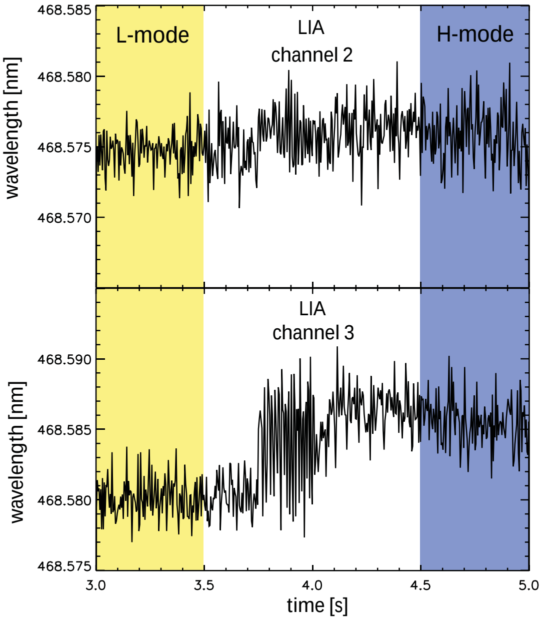

Figure 5.4: Time evolution of the emission spectrum line center of one channel

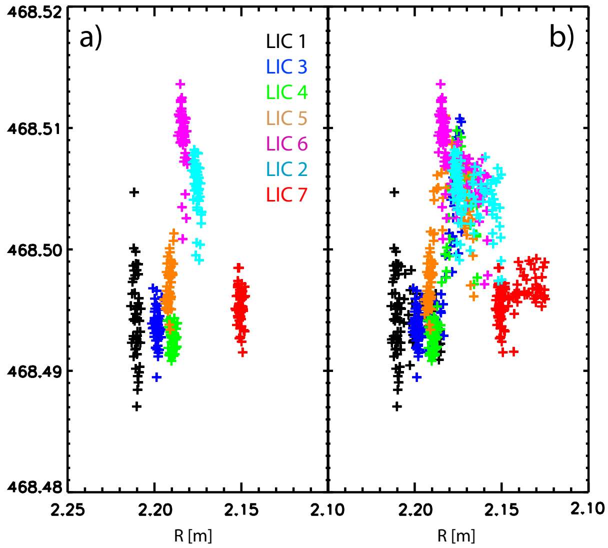

Figure 5.5: Central wavelength over radius for all LOS of LIC
a): constant plasma position
b): with R_{aus} scan

5.2 Raw data

After having discussed the data acquisition, a first approach to explore the information content and its accuracy could be done. Therefore, the passive line integrated He II line was fitted by a single Gaussian in order to determine the line center. The deviation from the tabulated value λ_0 is related to the velocity of the observed He^+ ions by the Doppler-shift, if effects due to line integration are neglected and the $E_r \times B$-drift is the only drift accounted for. Now, one can look either on the time evolution of the line center of single channels (figure 5.4) or at the relative wavelength shift between the channels (5.5 a)).
In the first case, the results depend strongly on the observed channel. The most obvious difference is the presence of a clear shift of the central wavelength between L- and H-mode of the plasma in channel 3 but not in channel 2. Due to the small radial distance (about 6 mm) in the launching point of these parallel lines of sight, a strong shear in rotation velocity has to be present at the plasma edge. This first interpretation of the measurements is in agreement with the prediction of transport reduction in the pedestal due to poloidal velocity shear (see chapter 4). Furthermore, the clear difference in central wavelength of LIA channel 3 demonstrates, that the experimental setup is accurate enough to measure the small shifts in the order of 0.005 nm even though the accuracy of the data analyzed by a single Gaussian is about 0.004 nm, estimated from the scatter. In the next chapter a more advanced method is presented, which substantially

increases the accuracy.
In the second case (figure 5.5 a)), which compares relative shifts of the channels, it is possible to make first assumptions on the shape of the radial electric field. The central wavelength of each channel of the LIC spectrometer, within a short time interval of 0.5 s during H-mode, is plotted over a radial position. The assignment of a position to a channel is not trivial due to non-localized line integrated measurements. As a rough estimate the intersection point of each LOS with a plane of constant Z coordinate was used. Therefore, from left to right, the LOS penetrates deeper into the plasma. Only the channels 6 and 2, which are located in the middle of the measuring range, show a clear jump in central wavelength. This indicates a very narrow shell ($\sim$ 3 cm) of increased toroidal rotation velocity with steep gradients. The maximal wavelength shift of $\delta\lambda = 0.015$ nm indicates a depth of the associated radial electric field of -20 kV/m assuming a magnetic field of -2 T. From channel 7 it can be concluded that the rotation velocity has to be reduced again further inward. Assumptions on the gradient are not possible due to a lack of resolution on this side using only one spectrometer. This was fixed on the one hand by introducing a short radial plasma shift or, on the other hand, by combining the measurements of both spectrometers. Figure 5.5 b) shows the results with improved resolution due to a short outward shift of the separatrix of $\sim$2 cm within the time interval of 0.5 s. The values characterizing the radial electric field derived in this chapter have to be used with great care, because essential effects like line integration or the diamagnetic drift have been neglected.

5.3 Calibration

In the section just above, shifts of the line center of about 0.015 nm were discussed, which is nearly equal to the resolution of the cameras (0.0175 nm for LIA and 0.0129 nm for LIC). Therefore, line shifts of one pixel and below had to be measured, which could only be done with sufficient accuracy by fitting the whole spectrum (58 pixel in the case of the LIA spectra and 78 pixel in the case of the LIC spectrometer). The model used to fit the data is described in detail in chapter 6. The absolute wavelength calibration of each spectrometer and also the cross calibration of the two spectrometers had to be done with comparable or even better resolution to reduce the error of derived profiles. Accurate intensity calibration was also required to enable emission profile reconstruction, required for unfolding the line integrated spectra.

Wavelength calibration: The assignment of a pixel position to the appropriate wavelength is the most crucial point of the presented diagnostic. The required high level of accuracy could only be achieved by including corrections for optical effects. Lens effects, pincushion distortion and a tilt of the camera were analyzed in order to create correction functions for the wavelength calibration and the profile measurements. The wavelength calibration itself was performed with a helium spectral lamp, whose spectrum was recorded for a large wavelength region. Identifying the discrete emission lines by the use of the NIST database [55], a consistent calibration for a large range of central wavelengths of the spectrometer could be calculated. Furthermore, the accuracy of the absolute wavelength calibration was increased even more by connecting one spectrometer channel to a Zn-lamp, which has an emission line within the measurement region at 468.01 nm. This results in an in-situ correction factor that was included in the profile reconstruction. On the one hand it was used for relative alignment of the wavelength calibration of the two spectrometers. On the other hand the variation of the line center of the Zn-lamp is a measure for the error of the absolute wavelength calibration, which was included in the Bayesian data analysis presented in the next chapter.

Intensity calibration: As already mentioned, also an absolute calibration $\vec{C}_A$ of each channel n was required. For earlier discharges an Ulbricht rod was used. For the campaigns in the years 2010 and 2011 it was replaced by an Ulbricht sphere. The radiance of the sphere R_s in $\left[\frac{W}{nm \cdot m^2 \cdot sr}\right]$ at the wavelength of the He II line is multiplied with the full solid angle of 4π, with the width of a pixel on the detector and divided by the energy of a photon $\frac{h \cdot c}{\lambda}$ leading to the emission E_s of the sphere in $\left[\frac{\text{Photons}}{m^2 s}\right]$. This emission was calculated for the observed transition at $\lambda = 468.57\,\text{nm}$ and related to the countrate of the n-th channel of the camera

$$C_{A,n} = \frac{E_s}{\text{countrate}_n} \qquad \left[\frac{\text{Photons}}{m^2 \cdot \text{counts}}\right], \tag{5.1}$$

resulting in the absolute calibration factor $C_{A,n}$ for each spectrometer channel. The measurement noise was taken into account by recording about 2000 samples and taking the average. The standard deviation gives the uncertainty $\sigma_{C_{A,n}}$.

LOS calibration: A measurement, obtained by passive spectroscopy, is strongly dependent on the path of the LOS in the vessel and also on the path relative to the plasma. Determining the latter was already discussed in section 2.2 using the CLISTE code. The absolute viewing path in the vessel was measured using the FARO system. This high precision 3D measuring system, using a movable mechanical arm, is installed during vessel openings at ASDEX Upgrade. By measuring the position of two points along the illuminated LOS, the path is completely determined. To combine this method with an alternative one, that had been used in earlier discharges, a virtual joint starting point of all LOS was calculated together with the intersection point on a plane with constant z value equal to that of the Li-beam injection tube. This intersection point, in combination with the distance to the end of the tube, is also sufficient to determine the path of each LOS in the vessel. If no FARO measurement was available for one LOS, interpolation at the Li-beam z-value was used. In figure 5.6, one can see the LOS connected to the two spectrometers (LOS of the LIA spectrometer in yellow and LOS of the LIC spectrometer in blue). This plot was created with the AUGddd program written by Tillman Lunt.[50] The measurements by the outermost channels (LIA 1-3 and LIC 1) have to be used with

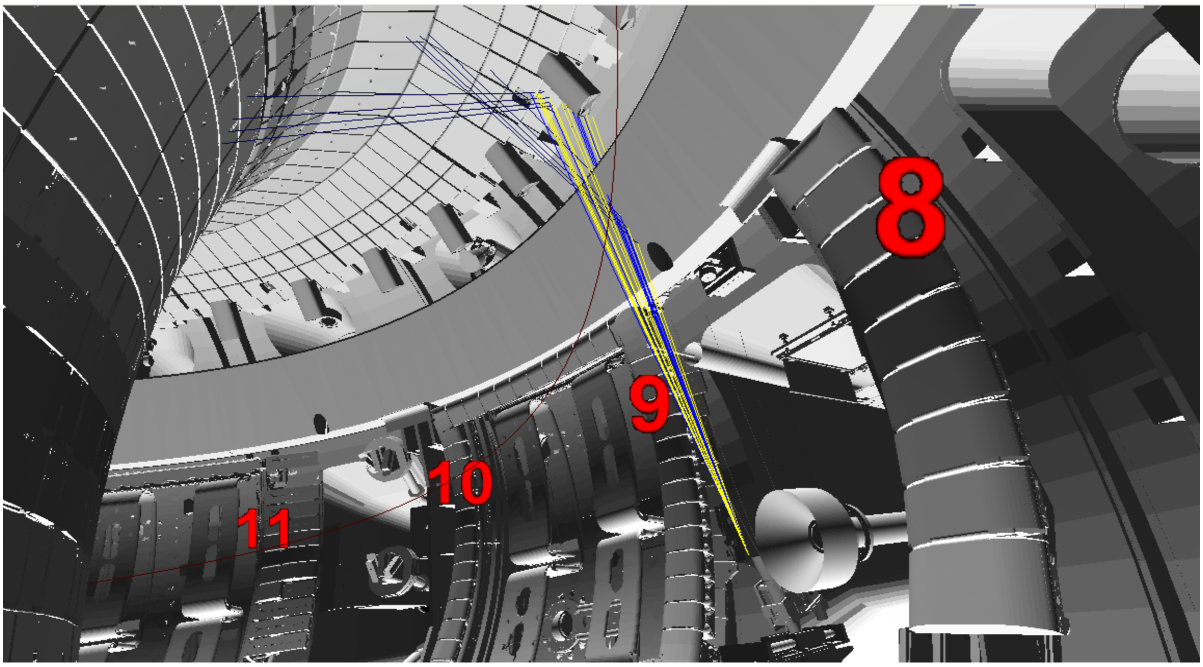

Figure 5.6: Setup of the diagnostic; LOS of LIA spectrometer in yellow; LOS of LIC spectrometer in blue; reflections of innermost and outermost LOS in black

care in the data evaluation, because there is the possibility of reflections (black lines) at the passive stabilizer loop (PSL) directly into the upper divertor. This leads to increased photon count rates and a possible modification of the line shape. In chapter 7 this is discussed in more detail using measured data. There, it will be shown, that the shift of the line center used in this chapter is only marginally modified. The innermost channels (LIA 7-10 and LIC 7-8) suffered also from reflections (black lines in figure 5.6). These LOS hit the lowest upper divertor plate and are reflected back into the high field side SOL of the plasma, also leading to increased count rate and modifications of the line shape.

6 Probabilistic data analysis

Having discussed the experimental setup and some first results in the last chapter, the focus will now be shifted to the development of an evaluation method for the radial electric field, that takes into account the complete physics discussed in the first part of this thesis (chapters 1 to 4). The main task is to unfold the line integrated measurements and to separate the contribution of the $E \times B$ velocity from the total poloidal velocity. The first part is normally done by applying Abel inversion to the measured profiles and the second one by physical considerations (see the radial force balance equation (2.18)). In this work, an alternative approach was chosen. Integrated data analysis was used to extract the radial electric field profile from the measured data by Bayesian probability theory (BPT), implementing a so-called forward model. It calculates modeled emission profiles for each LOS dependent on the radial profiles, prior knowledge and boundary conditions. Advantages of this approach are consistent error estimations within this fully probabilistic framework, integration of prior knowledge and the possibility to include non-Gaussian-distributed measurement errors.

6.1 Bayesian probability theory

Following the book of Sivia [53], the basic difference of Bayesian probability theory (BPT) to classical statistics is a different understanding of probability. The definition of probability as frequency of an event in infinitely many repeated experiments is used in classical statistic. In contrast to that, in BPT, it represents the degree of belief of the given hypothesis considering all related information available. Basic logical considerations lead to the usual rules of probability theory:

$$p\left(X|I\right) + p\left(\bar{X}|I\right) = 1 \tag{6.1}$$

$$p\left(X,Y|I\right) = p\left(X|Y,I\right) \times p\left(Y|I\right). \tag{6.2}$$

$\bar{X}$ represents the complementary hypothesis to X. The | sign indicates, that the probability of the hypothesis is conditional on an other hypothesis. As mentioned just above, I is the background information the probability is based on. Combining these two equations, Bayes theorem

$$p\left(X|Y,I\right) = \frac{p\left(Y|X,I\right) \times p\left(X|I\right)}{p\left(Y|I\right)} \tag{6.3}$$

is derived.[53] Applying this concept to data analysis, Y is replaced by the measured data $\vec{d}$ and X by the physical model M with parameters $\vec{\eta}$. The term on the left side then represents a measure for the truth of the chosen physical model (respectively the chosen model parameters) based on the measurements $\vec{d}$, called posterior probability. This is related to the likelihood probability, the first term of the numerator. It is a measure for the likeliness of getting the data $\vec{d}$ by using the model M. The posterior probability also depends on the compatibility of the model parameters with the prior knowledge I, expressed by the prior probability. The term in the denominator depends on the chosen model and is therefore often used in model comparison. For parameter estimation using only one model it can be neglected. The Bayes theorem is now given by

$$p\left(M\left(\vec{\eta}\right)|\vec{d}, I\right) \propto p\left(\vec{d}|M\left(\vec{\eta}\right), I\right) \times p\left(M\left(\vec{\eta}\right)|I\right). \tag{6.4}$$

Another interesting concept, directly derived from equations (6.1) and (6.2) in [53] is that of marginalization:

$$p\left(M\left(\vec{\eta}\right)|I\right) = \int_{-\infty}^{\infty} p\left(M\left(\vec{\eta}, \vec{\kappa}\right)|I\right) d\vec{\kappa}. \tag{6.5}$$

Sometimes it is necessary to include parameters $\vec{\kappa}$ in the physical model, whose exact values are of no particular interest. Such a parameter may be for example the background of a measured spectral profile. Applying marginalization to these so-called nuisance parameters reduces the dimension of the posterior PDF, but propagates the uncertainties of these parameters through the model.

As already motivated in the beginning of this chapter, a direct inversion of the line integrated measurements presented in this work was avoided by applying Bayes theorem. Therefore, a model M was developed, that relates the unknown radial profiles, the model parameters $\vec{\eta}$, to the measured line integrated data $\vec{d}$. The best estimate of these model parameters, with respect to the measured data and the prior knowledge, is then given by the maximum of the posterior PDF. The focus is therefore shifted from a direct analysis of measured data to the exploration of the posterior PDF.

6.2 Likelihood PDF

The posterior PDF (6.4) consists of two terms. The likelihood PDF, which is discussed in this section, and the prior PDF which is discussed in the next section. Looking at the likelihood in detail, on the one hand the model M has to be specified and on the other hand this model has to be combined with the measured data $\vec{d}$.

#	description
30	He^+ density (spline)
10	He^+ temperature (spline)
40	e^- temperature (correction spline)
35	E_r field (spline)
16	intensity calibration
2	count-photon conversion factor
2	wavelength correction
40	e^- density (correction spline)
2	Lorentz width of Voigt profile
16	count offset of each LOS
1	ρ_{pol} correction
$2 \cdot n$	n additional LOS (intens. & offset)

Table 6.1: Number of model parameters; lower part shows the included nuisance parameters

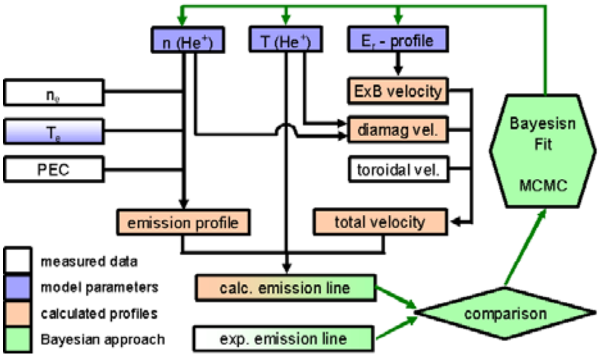

Figure 6.1: Flow chart of the forward model in white, blue and red together with the Bayesian fit and MCMC error estimation in green

6.2.1 Forward model

An overview of the model is given in the flow chart in figure 6.1, where the most important free model parameters $\vec{\eta}$ are marked in blue. The complete set of parameters is provided in table 6.1, where the lower ones are nuisance parameters. Each line in this table, referred to as parameter, is realized by more than one real parameter η_k. The reason for this is either the fact, that this parameter is different for each line of sight or it represents a radial profile specified by spline nodes. Furthermore, marked in red, one can see the most important profiles calculated by the model using the model parameters $\vec{\eta}$ and the prior knowledge I like atomic data. The model output $\vec{r}\left(\lambda, M\left(\vec{\eta}\right)\right)$, a line integrated spectrum, is marked with a color gradient from red to green because it is also an input for bayesian parameter estimation marked in green (discussed later in this chapter).

The basic task of the presented model is to calculate line integrated emission profiles of the He II $(n = 4 \rightarrow 3)$ transition. To simulate line integration, the experimental lines of sight are discretized by 200 non-equidistant points. The sum of the local line emission profiles at each point then gives an approximation of a line integrated measurement:

$$\vec{r}_k\left(\lambda, M\left(\vec{\eta}\right)\right) \propto \int_{LOS} g\left(\lambda, M\left(\vec{\eta}\right)\right)|_{\rho_{pol}(l)} dl \approx \sum_{l}^{LOS} g_l\left(\lambda, M\left(\vec{\eta}\right)\right) \cdot \delta l. \tag{6.6}$$

Therefore, the model can be simplified. It is sufficient to calculate the local line emission profile $g_l\left(\lambda, M\left(\vec{\eta}\right)\right)$ only at single points in the plasma. The overall shape of $g_l\left(\lambda, M\left(\vec{\eta}\right)\right)$ is modeled by a Voigt function specified by the emission A_l, the position $\lambda_{0,l}$, the width $\delta\lambda_{G,l}$ and a factor specifying the width of the Lorentzian part $\delta\lambda_L$.

Emission line amplitude $A\left(\rho_{pol}\right)$: Recalling the physics discussed in chapter 3, impact excitation was identified as the leading process in populating the excited $n = 4$ state. Equation (3.18)

$$A\left(\rho_{pol}\right) = \langle P \rangle = n_{He^+}\left(\rho_{pol}\right) \cdot n_e\left(\rho_{pol}\right) \cdot \mathrm{PEC}_{\mathrm{excit}}\left(n_e\left(\rho_{pol}\right), T_e\left(\rho_{pol}\right)\right) \cdot E_{Ph} \tag{6.7}$$

therefore determines the total emission in $[W/\left(m^3 \cdot nm\right)]$, enclosed by the local emission profile $g_l\left(\lambda, M\left(\vec{\eta}\right)\right)$. The emission profile $A\left(\rho_{pol}\right)$ depends on electron temperature, electron density and the He^+ density. As already discussed in chapter 4, the electron density profile $n_e\left(\rho_{pol}\right)$ at the plasma edge is provided by measurements. Thus, it was treated as prior knowledge I. To include the measurement errors in the model, a correction spline with 20 nodes was added to the profile, being allowed to vary within the error bars. The same concept was used for the electron temperature profile $T_e\left(\rho_{pol}\right)$. It is also measured and was included as prior knowledge. Again, a 20 node correction spline was added, due to the measurement errors. Furthermore, the effect of ECE shine through is automatically taken into account, because the uncertainties in this region rise drastically. Being to some part determined by measurements and to some part a free model parameter, this profile is marked with a color gradient in the flow chart. The He^+ density profile is not measured at ASDEX Upgrade routinely. Therefore, it was implemented as model parameter represented by a 10 node spline.

Emission line position $\lambda_0\left(\rho_{pol}\right)$: The central wavelength of an emission line is determined on the one hand by the transition causing it and on the other hand by the velocity of the emitting ion due to the Doppler shift. The central wavelength of the observed He transition in the NIST Atomic Spectra Database [55] is[8] $\lambda_C = 468.57\,\mathrm{nm}$. The shifted wavelength λ_0 was determined by the radial velocity profile due to the Doppler shift:

$$\lambda_0\left(\rho_{pol}\right) = \lambda_C \cdot \left(1 - \frac{v_{He^+,P}\left(\rho_{pol}\right)}{c}\right). \tag{6.8}$$

In chapter 2, a detailed discussion on particle movement in a toroidally confined plasma has been given. It was shown, that in first order the perpendicular motion of ions is solely determined by the $E \times B$ and the diamagnetic drift:

$$\vec{v}_{E\times B}\left(\rho_{pol}\right) = \frac{\vec{E}_r\left(\rho_{pol}\right) \times \vec{B}\left(\rho_{pol}\right)}{\left(B\left(\rho_{pol}\right)\right)^2} \qquad \vec{v}_{dia}\left(\rho_{pol}\right) = -\frac{\nabla p_{He^+}\left(\rho_{pol}\right) \times \vec{B}}{q_{He^+} n_{He^+}\left(\rho_{pol}\right) B^2}. \tag{6.9}$$

Because the field of view discussed in chapter 5 is not completely perpendicular to the magnetic field, it was necessary to project these perpendicular velocities on the lines of sight. Furthermore, the projection of the toroidal velocity has to be included as a small correction term. It is measured by CXRS and can be treated as prior knowledge I. Also contained in I is the magnetic field vector $\vec{B}$, which is given by the equilibrium reconstruction. The two remaining profiles, the radial electric field $\vec{E}_r$ and the He^+

---

[8] In the sensitivity study in the next chapter, the influence of the fine structure splitting and the Paschen-Back effect on the central wavelength is explored.

pressure profile were implemented as model parameters, because at ASDEX Upgrade there exists no diagnostic that measures the He^+ temperature profiles routinely. It was implemented as a 10 node spline and is required additionally to the already introduce He^+ density profile to calculate the He^+ pressure profile. 25 spline nodes are used to describe the radial electric field profile. By summing up all the contributions

$$v_{He^+,P}\left(\rho_{pol}\right) = v_{He^+}\left(\rho_{pol}\right)|_{LOS} = \vec{v}_{E\times B}\left(\rho_{pol}\right) + \vec{v}_{dia}\left(\rho_{pol}\right) + \vec{v}_{tor}\left(\rho_{pol}\right)|_{LOS}, \tag{6.10}$$

the projection of the total velocity v_{He^+} on the line of sight $v_{He^+,P}$ is calculated.

Emission line width $\delta\lambda\left(\rho_{pol}\right)$: The width of the Voigt shaped emission spectrum $g_l\left(\lambda, M\left(\vec{\eta}\right)\right)$ is a combination of the width of the Gaussian part (FWHM: $\delta\lambda_G$) and the width of the Lorentz part (FWHM: $\delta\lambda_L$), with which the Gaussian part is convoluted. Doppler broadening due to the temperature of the He^+-ions is Gaussian shaped:

$$\delta\lambda_G\left(\rho_{pol}\right) = \frac{\lambda_C}{c} \cdot \sqrt{\frac{8k_B T_{He^+}\left(\rho_{pol}\right) \cdot \ln 2}{m}}. \tag{6.11}$$

The radial profile of the He^+ temperature has already been introduced as model parameter in the last paragraph.

The complete equation for the modeled local emission spectrum in $\left[\frac{\text{Photons}}{m^3 \cdot nm \cdot s}\right]$ can be written as:

$$\begin{aligned} g_l\left(\lambda, M\left(\vec{\eta}\right)\right) =& A\left(n_e, T_e, n_{He^+}\right) \cdot \\ & \cdot \left(\varsigma * h\right)\left(\lambda, \lambda_0\left(\vec{E}_r, n_{He^+}, T_{He^+}\right), \delta\lambda_G\left(T_{He^+}\right), \delta\lambda_L\right)|_{\rho_{pol}(l,\rho_{corr})}, \end{aligned} \tag{6.12}$$

where $h\left(\lambda, ...\right)$ is a Voigt function with an area normalized to unity. The parameter $\delta\lambda_L$ was implemented as a constant for each spectrometer without radial dependency. This assumption was made because it turned out, that fitting both width, $\delta\lambda_G$ and $\delta\lambda_L$, as radial profile led to interdependencies due to too little information in the data. The Voigt shaped line profile is convoluted with the spectrometer function $\varsigma\left(\lambda\right)$. This function was derived from the spectrum of the calibration lamp connected to one channel of each spectrometer and assumed to be constant for all channels of a given spectrometer. To evaluate equation (6.12) at a certain ρ_{pol} value specified by the l-th discrete point along the calculated LOS, a small additive correction ρ_{corr} (≈ 0.005) had to be applied to the ρ_{pol} value. It depends on plasma shape and the side (left ($+\rho_{corr}$) or right ($-\rho_{corr}$)) of the optical head from which the LOS observes the plasma. The reason for this is the assumption of a shared starting point for all LOS (see section 5.3), which leads to a small error in the toroidal and poloidal angle of the LOS. A correction of the LOS angle would have given more accurate results but would also have increased the evaluation time to inacceptable values, because a time consuming (R, z) to ρ_{pol} mapping of all LOS would have to be done in each iteration instead of doing it at the startup of the program.

To derive the model output r_k in [counts] (see next section for a definition) for the k-th line of sight, some additional effects had to be included:

$$r_k\left(\lambda, M\left(\vec{\eta}\right)\right) \approx C_{A,k} \cdot \sum_{l}^{LOS} \left[g_l\left(\lambda + \lambda_{Corr}, M\left(\vec{\eta}\right)\right) \cdot \delta l\right] + O_k. \tag{6.13}$$

This was the intensity calibration $C_{A,k}$ (see section 5.3), an offset O_k in each line profile due to measurement background and an additive wavelength correction λ_{Corr} from the Zn lamp. Looking at table 6.1 one can see, that there are $2 \cdot n$ parameters reserved for n additional lines of sight. In section 5.2 the concept of shifting the plasma radially was introduced to increase the spatial resolution of the measurements. To included this in the model, it had to be assumed, that all radial profiles stay constant during the radial shift. Virtual lines of sight were introduced, which only differ in the time point used to map real coordinates to fux coordinates (ρ_{pol}) along a line of sight, using the equilibrium reconstruction. To relief this strong condition of unchanged plasma, each of this virtual lines of sight got a background and relative intensity model parameter on its own. This allowed a balancing of intensity changes of the He II line during the scan, which is caused by the following effect. Shifting the plasma outward leads to an increased particle flux to the wall. Therefore, more neutral helium is released into the plasma, which also increases the He^+ density. By decreasing the relative intensity calibration factor, this effect could be balanced. The small wavelength shift λ_{Corr} of the modeled emission spectrum, introduced in equation (6.13), takes the in-situ wavelength calibration into account. It was determined by the deviation in the position of the measured calibration lamp profile compared to the tabulated position.

An important point which should be mentioned here is the influence of the emission profile $A\left(\rho_{pol}\right)$ on the shape and shift of the line integrated emission spectrum. Looking at the model, the line shift of the modeled emission profile seems to be mainly determined by the velocity profile, which itself is governed by the drift created from the radial electric field (in the case of He^+). But relating the line shift directly to the radial electric field like it was done in section 5.2 neglects the weighting effect of the emission profile during line integration. A high emission on positions with a small shift can lead to a stronger total line shift than a large local line shift with vanishing emission amplitude.

6.2.2 Measured data

To write down an expression for the likelihood PDF, the output of the forward model $\vec{r}$ had to be related to the measured data $\vec{d}$. This relation is given by the probability of reproducing the measured data $\vec{d}$ with uncertainty $\vec{\sigma}$ for a given set of model parameters $\vec{\eta}$. The data points d_k are measured as positive integer values called counts within a predefined temporal and spatial interval by the CCD camera. This count number is related to the number of detected photons N during a given time interval and for a given wavelength region by a conversion factor Υ. Applying the same mapping to the count number calculated from the model r_k results in the mean number of photons F expected for a given set of model parameters $\vec{\eta}$. The probability of reproducing the data is given by the Poisson PDF

$$p\left(N|F\right) = \frac{F^N e^{-F}}{N!} \approx \frac{1}{\sqrt{2\pi N}} \exp\left(-\frac{\left(F-N\right)^2}{2N}\right), \tag{6.14}$$

which is commonly approximated by a normal distribution for high photon counts N. The derivation of equation (6.14) from the Binomial PDF presented in reference [53], makes use of a second order Taylor expansion and the Sterling approximation of the factorial $N!$. The standard deviation of this normal distribution is given by $\sqrt{N}$.
Photon emission due to line transitions in atoms is a statistical process, therefore the statistical noise σ_N of photons counted by the detector N is given by the width of the normal distribution associated to the expectation value F:

$$\sigma_N = \sqrt{N}. \tag{6.15}$$

This is independent of the expectation value and therefore correct, even if the expected value is not known exactly.

The final step towards an explicit formulation of the likelihood PDF was to determine the conversion factor Υ, which relates the counts d_k measured by the camera to the number of detected photons $N = d_k \cdot \Upsilon$. It can be obtained either by calibration of the CCD camera or directly from the measured spectra of a whole discharge. For the first possibility, the signal to noise ratio has to be measured for different mean count rates:

$$\Upsilon = \frac{\sigma_{d,k}^2}{d_k}. \tag{6.16}$$

The other possibility, which was used in this work, has the advantage, that it also could be applied to older discharges. For all measured data points (each pixel in each spectrum for all channels) of a discharge the local variation was determined. This is given by the scatter of the five nearest pixels compared to the tangent at the central point, visualized in figure 6.2 a). The square of this local variation was sorted by the count rate of the central pixel, leading to a large dataset of $(\sigma_d^2; d_k)$ data pairs. Fitting a regression line then defines the conversion factor Υ, its uncertainty σ_Υ and the readout noise σ_r (see figure 6.18 b)):

$$\sigma_{d,k}^2 = \Upsilon \cdot d_k + \sigma_r^2. \tag{6.17}$$

The read-out noise arises from the electronic devices of the experimental setup. A consistency check was made by comparing it to the measured scatter during the first frames of each discharge, where the plasma breakdown had not been established yet $(d_k = 0)$.

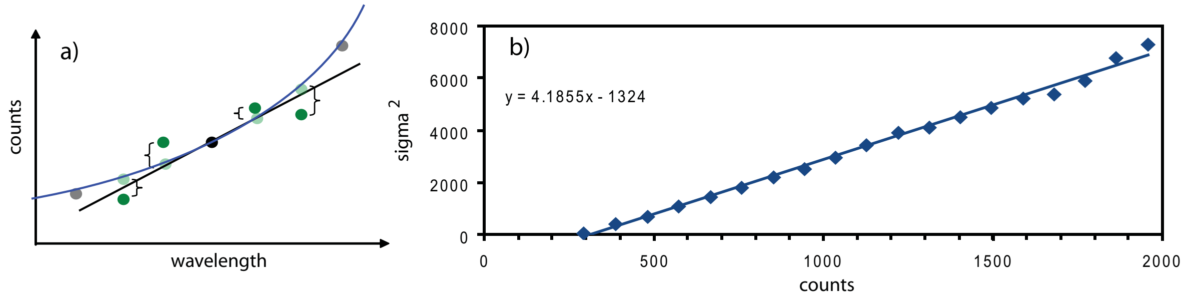

Figure 6.2: **Left:** Sketch of the determination of the local variation
Right: Squared variation plotted over binned count rate

Using equation (6.14), the likelihood PDF of a single point within a measured spectrum d_k is given by

$$p\left(d_k|M\left(\vec{\eta}\right),I\right)=\frac{1}{\left(\sqrt{\Upsilon\cdot d_k+\sigma_r^2}\right)\sqrt{2\pi}}\exp\left[-\frac{\Upsilon^2\cdot\left(r_k-d_k\right)^2}{2\left(\Upsilon\cdot d_k+\sigma_r^2\right)}\right]. \tag{6.18}$$

The combined likelihood PDF $p\left(d_{k_1},d_{k_2},...|M,I\right)$,

$$p\left(\vec{d}|M\left(\vec{\eta}\right),I\right)=\prod_k p\left(d_k|M\left(\vec{\eta}\right),I\right) \tag{6.19}$$

is simplified by recalling equation (6.2) and assuming, that the probability of measuring a data point d_{k_1} is independent of measuring another data point d_{k_2}:

$$p\left(d_{k_1}|d_{k_2},M,I\right)=p\left(d_{k_1}|M,I\right). \tag{6.20}$$

Inserting equation (6.18) in (6.19) leads to a very compact way of writing the likelihood PDF

$$p\left(\vec{d}|M\left(\vec{\eta}\right),I\right)\propto\exp\left(-\frac{\chi^2}{2}\right), \tag{6.21}$$

where χ^2 is the square of the normalized residual

$$\chi_d^2=\sum_k\left(\frac{F_k-N_k}{\sigma_{N,k}}\right)^2, \tag{6.22}$$

with $N_k=\Upsilon\cdot d_k$, $F_k=\Upsilon\cdot r_k$ and $\sigma_{N,k}=\sqrt{\Upsilon\cdot d_k+\sigma_r^2}$. In this likelihood PDF Gaussian error bars $\vec{\sigma}_N$ are assumed for the measured photon counts $\vec{N}$ (see chapter 7.1).

Until now, all considerations in this chapter concerning the measurements $\vec{N}$ and the associated uncertainties $\vec{\sigma}_N$ assume well behaving normally distributed deviations from the exact counts. But for real measurements there are data points which are far from their

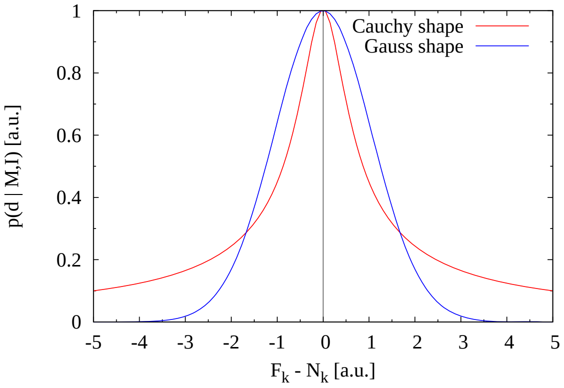

Figure 6.3: Comparison of Gaussian and Cauchy shaped probability density functions

expected value, called outliers. These measured values disturb the parameter estimation, because the error assigned to them using the normal distribution is too small. To account for this true but unknown error, $\vec{\tilde{\sigma}}_N$ is introduced, that can differ from $\vec{\sigma}_N$ but should be of the same order:

$$p\left(\tilde{\sigma}_{N,k}|\sigma_{N,k},I\right)=\frac{2\sigma_{N,k}}{\sqrt{\pi}\tilde{\sigma}^2_{N,k}}\exp\left(-\frac{\sigma^2_{N,k}}{\tilde{\sigma}^2_{N,k}}\right). \tag{6.23}$$

The unknown error $\vec{\tilde{\sigma}}_N$ is marginalized by equation (6.5)

$$p\left(\vec{d}|M\left(\vec{\eta}\right),I\right)=\int_0^\infty p\left(\vec{d}|M\left(\vec{\eta}\right),\vec{\tilde{\sigma}}_N,I\right)p\left(\vec{\tilde{\sigma}}_N|\vec{\sigma}_N,I\right)d\vec{\tilde{\sigma}}, \tag{6.24}$$

resulting in an Cauchy shaped likelihood PDF

$$\chi^2_d=\sum_k 2\cdot\log\left(\frac{1}{2}+\frac{1}{2}\cdot\left(\frac{F_k-N_k}{\sigma_{N,k}}\right)^2\right), \tag{6.25}$$

derived in [52]. The main differences of this likelihood PDF to the Gaussian shaped PDF are the much slower decaying wings (see figure 6.3). These are the consequences of possible higher error bars and provide a more tolerant behavior if outliers are involved.

6.3 Prior PDF

The second term of the posterior PDF in (6.4), which still needs to be discussed is the prior PDF. On the one hand, known error estimations for profiles included in the prior knowledge should be taken into account and on the other hand, reasonable restrictions on the free model parameters speed up and stabilize the maximization of the posterior PDF.

6.3.1 Uncertain prior knowledge

In the presentation of the forward model, some parameters were introduced as model parameters $\vec{\eta}$ like the absolute calibration factors, even though they were measured and therefore should have been included in the prior knowledge I. The reason for that is, that these measured values are uncertain. This was taken into account by including these parameters as nuisance parameters $\vec{\xi}$ in the model $M\left(\vec{\eta}\right) \to M\left(\vec{\tilde{\eta}}, \vec{\xi}\right)$ with the associated Gaussian distributed error $\vec{\sigma}_\xi$ and the reference value $\vec{\xi_0}$:

$$p\left(\xi_k|I\right) \propto \exp\left(-\frac{1}{2}\cdot\left(\frac{\xi_k-\xi_{k,0}}{\vec{\sigma}_{\xi,k}}\right)^2\right). \tag{6.26}$$

$\vec{\tilde{\eta}}$ is the reduced set of model parameters given by the upper part of table 6.1. Rewriting equation (6.26) in a way similar to the one used for the likelihood PDF leads to

$$p\left(\xi_k|I\right) \propto \exp\left(-\frac{\chi^2}{2}\right) \qquad \text{with} \qquad \chi^2_\xi = \left(\frac{\xi_k-\xi_{k,0}}{\vec{\sigma}_{\xi,k}}\right)^2. \tag{6.27}$$

Marginalizing out these parameters by applying equation (6.5), a direct dependence of the posterior PDF on these parameters is not given, but the error is propagated correctly to the uncertainties of the results.

Calibration factors: This method was applied to the calibration factors of the forward model, which were derived at the end of chapter 5. For each LOS, an absolute calibration factor $C_{A,k}$ was introduced as nuisance parameter and included in $\vec{\xi}$, together with a measured value $C_{A,0,k}$ and its measurement uncertainty $\sigma_{C_A,k}$.

Count-photon conversion: Also included in $\vec{\xi}$ is the count-photon conversion factor Υ for each spectrometer. The algorithm presented in the last section provides the reference value Υ_0 with its uncertainty σ_Υ.

Wavelength correction: Dependent on the experimental campaign, both spectrometer, only the LIA spectrometers or non of the spectrometers were connected to the Zn calibration lamp. If available for a spectrometer, the measured wavelength correction $\lambda_{Corr,0} \pm \sigma_\lambda$ was included in $\vec{\xi}$ otherwise it was treated as free model parameter.

Electron density profile: Obtained by integrated data analysis, the electron density profile $n_e\left(\rho_{pol}\right)$ is provided with error estimations $\sigma_{ne}\left(\rho_{pol}\right)$, which were included in the model by adding a correction spline $\tilde{n}_e\left(\rho_{pol}\right)$ to the measured electron density profile.

The spline parameters were treated as nuisance parameters $\vec{\xi}_{ne}$ and included in $\vec{\xi}$. The squared residual associated to this profile were calculated using a discretized version of the spline

$$\chi^2_{ne} = \sum_j \left(\frac{\tilde{n}_{e,j}}{\sigma_{ne,j}} \right)^2, \tag{6.28}$$

where the correction $\tilde{n}_{e,j}$ is expected to be close to 0 within the given error.

Electron temperature profiles: The presentation of the forward model discusses the special role of the electron temperature profile. On the one hand, the inner part of the profile is determined by prior knowledge from ECE measurements and on the other hand, the outer part is treated as free model parameter. This was realized by introducing a correction spline $\tilde{T}_e(\rho_{pol})$, which was added to the ECE electron temperature profile $T_e(\rho_{pol})$, comparable to the electron density profile. Again, the spline parameters were treated as nuisance parameters $\vec{\xi}_{T_e}$, which were included in $\vec{\xi}$. The squared residual $\chi^2_T e$ is given by a summation over the discretized profile:

$$\chi^2_{Te} = \sum_j \left(\frac{\tilde{T}_{e,j}}{\sigma_{Te,j}} \right)^2. \tag{6.29}$$

In regions where $T_e(\rho_{pol})$ was not defined by the ECE measurement, $\vec{\sigma}_{T_e}(\rho_{pol})$ was large (see region just outside the separatrix in figure 4.2) and the influence of the reference value $T_{e,j}$ on the profile was reduced. Depended on the measurement error of the ECE, a smooth transition of $\vec{\xi}_{T_e}$ between nuisance and free model parameter was given.

The remaining parameters classified as nuisance parameters in table 6.1 (Lorenz width, count offset of LOS, ρ_{corr} and the parameters of the additional LOS) were not measured. Therefore, they were treated as free fitting parameters whose final values are not relevant for the interpretation of the results. But they had to be included, to give the model the required flexibility to adapt to the measured data and to get a realistic error estimation.

6.3.2 Restrictions on free model parameters

The concept of restricting the variation of the nuisance parameters by the prior PDF is now generalized to apply restrictions also on the model parameters. This was useful to increase the numerical stability of the model and helped to avoid convergence problems, due to interdependencies in an underdetermined model. The explicit realization of each boundary condition included in the model presented in this work is discussed in the following. To simplify the combination of all boundary conditions within the prior PDF, they were defined as Gaussian shaped functions only differing in the χ_k:

$$p\left(\tilde{\eta}_k|I\right) \propto \exp\left(-\frac{\chi_k^2}{2}\right). \tag{6.30}$$

Electron temperature profile: As already discussed, the electron temperature was required for calculating the emission profile, using the He^+ density and the PEC data. An accurate emission profile has a key role in modeling the measured data, due to the weighting during line integration. Therefore, detailed knowledge of the electron temperature in the near SOL was required to model the onset of He II emission correctly. Because at ASDEX Upgrade electron temperatures in the near SOL are not available with the required resolution, the error of the electron temperature in this region was set to a constant value of 100 eV. This gave the model the ability to balance inaccuracies of the model itself and also of the PEC for low temperatures.

He^+-temperature profile: The He^+ temperature profile, which is not measured at ASDEX Upgrade and therefore introduced as free model parameter, had to be regularized, because the available information in the measured He^+ line profiles was not sufficiently accurate over the whole radial range, required by the model. Looking from the plasma center outward, a monotonic decaying profile was assumed, which translates into the following prior for the discretized spline:

$$\chi^2_{T_{He^+,s}} = \sum_j \left\{ \begin{array}{c|l} \left(\frac{T_{He^+,(j)} - T_{He^+,(j-1)}}{\epsilon_{T_{He^+}}}\right)^2 & T_{He^+,(j)} - T_{He^+,(j-1)} > 0 \\ 0 & \text{otherwise} \end{array} \right\}. \tag{6.31}$$

A constant regularisation $\epsilon_{T_{He^+}} = 0.5\,\mathrm{eV}$ of the slope at each discrete step was used to prevent oscillations of the He^+ temperature spline near the hot inner boundary of the profile. Furthermore, a minimal temperature of 50 eV was assumed inside the separatrix. This prevented the parameter estimation from being trapped at unrealistic emission profiles due to very narrow calculated emission lines:

$$\chi^2_{T_{He^+,v}} = \sum_j \left\{ \begin{array}{c|l} \left(\frac{T_{He^+,(j)} - 50\,\mathrm{eV}}{1\,\mathrm{eV}}\right)^2 & \rho_{pol} < 1.0 \quad \wedge \quad T_{He^+} < 50\,\mathrm{eV} \\ 0 & \text{otherwise} \end{array} \right\}. \tag{6.32}$$

He^+-density profile: Being directly derived from the well determined emission profile, only the slope of the He^+ density at the inner and outer boundary had to be restricted. Due to the vanishing emission profile, the He^+ density is not determined in this region. The atomic model presented in chapter 3 predicts a vanishing He^+ density for both boundaries, on the outer side due to the too low electron temperature and density and on the inner side due to full ionization:

$$\chi^2_{n_{He^+}} = \sum_j \left\{ \begin{array}{c|l} \left(\frac{\tilde{n}_{He^+,(j)} - \tilde{n}_{He^+,(j-1)}}{\epsilon_{n_{He^+}}}\right)^2 & n_{He^+,(j)} - n_{He^+,(j-1)} > 0 \ \wedge \ \rho_{pol} > 1.06 \\ \left(\frac{\tilde{n}_{He^+,(j)} - \tilde{n}_{He^+,(j-1)}}{\epsilon_{n_{He^+}}}\right)^2 & n_{He^+,(j)} - n_{He^+,(j-1)} < 0 \ \wedge \ \rho_{pol} < 0.95 \\ 0 & \text{otherwise} \end{array} \right\}. \tag{6.33}$$

The slope restriction is applied to the logarithm of the density $\tilde{n}_{He^+,(j)} = \log\left(n_{He^+,(j)}/m^3\right)$, to ensure the regularizing effect in all orders of magnitude ($1 \cdot 10^{14}\,\mathrm{m}^{-3}$–$3 \cdot 10^{19}\,\mathrm{m}^{-3}$). The regularization parameter $\epsilon_{n_{He^+}}$ was set to 0.1.

Radial electric field: The most interesting model parameter for this work is the radial electric field. It is only determined by the data in the region with non-vanishing He II emission, analog to the He^+-density profile. Therefore, it was necessary to restrict the shape of the profile in the undefined region. The inner and outer boundary condition is given by minimal and maximal values:

$$\chi^2_{Er} = \sum_j \left\{ \begin{array}{c|lcl} \left(\frac{Er_{(j)} - 0\,\mathrm{kV/m}}{0.5\,\mathrm{kV/m}}\right)^2 & \rho_{pol} < 0.95 & \wedge & Er < +0\,\mathrm{kV/m} \\ \left(\frac{Er_{(j)} - 60\,\mathrm{kV/m}}{0.5\,\mathrm{kV/m}}\right)^2 & \rho_{pol} < 0.95 & \wedge & Er > +60\,\mathrm{kV/m} \\ \left(\frac{Er_{(j)} + 20\,\mathrm{kV/m}}{0.5\,\mathrm{kV/m}}\right)^2 & \rho_{pol} > 1.04 & \wedge & Er < -20\,\mathrm{kV/m} \\ \left(\frac{Er_{(j)} - 20\,\mathrm{kV/m}}{0.5\,\mathrm{kV/m}}\right)^2 & \rho_{pol} > 1.04 & \wedge & Er > +20\,\mathrm{kV/m} \\ 0 & \text{otherwise} & & \end{array} \right\}. \tag{6.34}$$

Furthermore, the slope in the weakly determined regions with an emission of nearly zero had to be regularized in order to prevent mathematically possible but physically not realistic shapes:

$$\chi^2_{Er} = \sum_j \left\{ \begin{array}{c|l} \left(\frac{Er_{(j)} - Er_{(j-1)}}{\epsilon_{Er}}\right)^2 & Er_{(j)} - Er_{(j-1)} > 0 \quad \wedge \quad 0.94 < \rho_{pol} < 0.975 \\ 0 & \text{otherwise} \end{array} \right\}. \tag{6.35}$$

ϵ_{Er} is set to a value of $0.1\,\mathrm{kV/m}$. In order to reproduce the steep gradients, a high number of spline nodes was necessary. The disadvantage of this is the possibility of very narrow and too deep structures in the radial electric fields in regions with low LOS coverage. To prevent this, a weak restriction on the curvature of the radial electric field was introduced:

$$\chi^2_{Er,C} = \sum_j \left(\frac{S''_{Er,(j)}}{1 \cdot 10^9\,\mathrm{V/m^3}}\right)^2. \tag{6.36}$$

6.3.3 Restrictions on calculated profiles

Additionally to the already discussed restrictions on the model parameters $\vec{\nu}$, also indirect restrictions were necessary acting on calculated profiles.

Emission profile: A regularization was necessary for the emission profile to increase the stability of the parameter estimation. Inside the separatrix ($\rho_{pol} < 0.99$) the spline is restricted to have a positive slope and outside the separatrix ($\rho_{pol} > 1.04$) to a negative slope

$$\chi^2_{Em} = \sum_j \left\{ \begin{array}{c|lcl} \left(\frac{Em_{(j)} - Em_{(j-1)}}{\epsilon_{Em}}\right)^2 & Em_{(j)} - Em_{(j-1)} < 0 & \wedge & \rho_{pol} < 0.99 \\ \left(\frac{Em_{(j)} - Em_{(j-1)}}{\epsilon_{Em}}\right)^2 & Em_{(j)} - Em_{(j-1)} > 0 & \wedge & \rho_{pol} > 1.04 \\ 0 & \text{otherwise} & & \end{array} \right\}, \tag{6.37}$$

with a regularization parameter of $\epsilon_{Em} = 0.1\,\frac{\mathrm{W}}{\mathrm{m^3 \cdot nm}}$. To ensure a vanishing emission profile at the inner and outer boundary, the solution with the minimal area enclosed by the spline and the ρ_{pol} axis is preferred by adding the prior

$$\chi^2_{Em} = \sum_j \left(\frac{Em_{(j)}}{300\,\frac{\mathrm{W}}{\mathrm{m^3 \cdot nm}}} \right)^2 . \tag{6.38}$$

Furthermore, restrictions on the absolute values of the emission profile had to be made to prevent the fit from being trapped in local maxima in the starting phase far from the maximum:

$$\chi^2_{Em} = \sum_j \left\{ \begin{array}{c|l} \left(\frac{Em_{(j)} - 200.0\,\mathrm{W}/\left(\mathrm{m^3 \cdot nm}\right)}{0.1\,\mathrm{W}/(\mathrm{m^3 \cdot nm})}\right)^2 & Em_{(j)} > 200.0\,\frac{\mathrm{W}}{(\mathrm{m^3 \cdot nm})} \\ 0 & \text{otherwise} \end{array} \right\}. \tag{6.39}$$

At the end of the last chapter, the possibility of measuring too high counts for the inner lines of sight was discussed due to reflections. This can be prevented by introducing a stronger tendency towards zero emission for ρ_{pol} values lower than 0.97, which is further inward than the edge pedestal and thus has no effect on the minimum in the radial electric field:

$$\chi^2_{Em} = \sum_j \left\{ \begin{array}{c|l} \left(\frac{Em_{(j)}}{5.0\,\mathrm{W}/(\mathrm{m^3 \cdot nm})}\right)^2 & \rho_{pol} < 0.975 \\ 0 & \text{otherwise} \end{array} \right\}. \tag{6.40}$$

Diamagnetic velocity: As already discussed in chapter 2.3, the diamagnetic drift is given by equation (2.13):

$$\vec{v}_D = -\frac{\nabla p \times \vec{B}}{qnB^2}.$$

The term $\nabla p/n$ is numerically unstable for He^{+}, because both the pressure and the density are vanishing towards the plasma center. To avoid arbitrary high values of the diamagnetic velocity due to slightly ill shaped estimated profiles in a region with very little information in the data because of the vanishing He II emission, the value of $\vec{v}_D$ was restricted to a maximal value of 50 km/s.

6.4 Posterior PDF

In the last two sections, the likelihood PDF and the prior PDF have been discussed in detail. Now they are combined to the posterior PDF in equation (6.4)

$$p\left(\vec{d}|M\left(\vec{\eta}\right),I\right)=\prod_k p\left(d_k|M\left(\vec{\eta}\right),I\right)\cdot\prod_i p\left(\eta_i|I\right). \tag{6.41}$$

Assuming the independence of the probability of measuring each data point (see equation (6.19)) and also the independence of the different contributions to the prior PDF, the following simplification can be made

$$p\left(\vec{d}|M\left(\vec{\eta}\right),I\right)\propto\exp\left(-\frac{\vec{\chi}^2}{2}\right) \tag{6.42}$$

$$\vec{\chi}^2=\chi_d^2+\chi_\xi^2+\chi_{\tilde{\eta}}^2 \tag{6.43}$$

by recalling that all $p\left(d_k|...\right)$, $p\left(\eta_i|...\right)$ and $p\left(\xi_i|...\right)$ are Gaussian shaped PDFs.

6.4.1 Detection of the maximum

The posterior PDF provides the probability, that the modeled profiles (associated to a specific set of model parameters $\vec{\eta}$) reproduce the measured profiles, which are disturbed by measurement noise and meets the provided priors within the specified uncertainties. Therefore, exploring the maximum of the posterior PDF gives information on the most probable model parameters η^* and the associated uncertainties σ_η. An equivalent and numerically more stable approach is given by defining the Logarithm of the posterior PDF

$$L=c-\frac{1}{2}\left(\vec{\chi}^2\right) \tag{6.44}$$

and exploring the maximum of L, where c is an arbitrary constant.[53] A solver for dense nonlinear programming problems from the NAG (Numerical Algorithms Group) Fortran90 library [54] was used to find the most probable η^*. No other constraints than upper and lower values for each parameter had to be specified, because the posterior PDF (L respectively), which was set as objective function already contained the complete prior knowledge discussed in the last section. Recalling the flow chart in figure 6.1, determining the maximum of L is illustrated in green and labeled as “Bayesian fit”.

6.4.2 Error estimation

One way to determine the uncertainty of the estimated parameters, which maximize the posterior PDF, is to calculate the curvature at the maximum η^*. This method is only useful for peaked uni-modal PDF's. As derived in [53], by applying a Taylor expansion to equation (6.44), the first order term $(\ldots \sum_i \frac{\partial L}{\partial \eta_i} \ldots)$ can be neglected because it is zero. The second order term is the leading one and therefore a good approximation of the curvature at the maximum. The covariance matrix $\bar{C}$ is then given by the inverse Hessian matrix, containing all second derivatives.

$$\bar{C} = -\left(\nabla\nabla L\right)^{-1} \tag{6.45}$$

The square root of the diagonal elements $\sqrt{C_{\eta\eta}}$ of this matrix are the marginal uncertainties of the model parameters: $\vec{\eta} \pm \vec{\sigma}_\eta$. An alternative way to determine these values is to use equation (6.5) to marginalize all model parameters except the i-th one η_i from the posterior PDF and fit a Gaussian to get the width $\sigma_{\eta,i}$. The off-diagonal elements are a measure for the correlation of the different model parameters. If the correlations of a parameter η_i with all others gets too large only dependencies between the correlated parameters can be derived.

6.4.3 Marcov chain Monte Carlo

Another way of determining the most probable values for the model parameters and their uncertainties is to construct a Markov chain[9] with the posterior PDF as target distribution. Then, a sufficiently large amount of samples from this Markov chain has the same features (e.g. mean value, standard deviation) as the posterior PDF.[57] In 1970 W. K. Hastings presented a paper, which showed that an algorithm previously developed by N. C. Metropolis can be used to draw samples form a high-dimensional PDF, the target distribution of the Marcov chain. This so-called "Monte Carlo method" [59] uses random numbers to sample a distribution function.[58] Combining the Monte Carlo algorithm and the generalizations by Hastings, leads to the "Metropolis-Hastings algorithm", discussed in detail in this section.

Metropolis-Hastings algorithm: In general, Markov chain Monte Carlo algorithms are used to determine the transition probability $p(x, y)$ of the different states of the Markov chain for a given target density $\pi(x)$, in this case the posterior PDF. In the implementation of the Metropolis-Hastings algorithm within this work, a Cauchy shaped candidate-generating density $q\left(x,y\right)$ is chosen. It describes a guess for the probability of advancing from state x to state y in the Markov chain. Then, the real probability for $x \neq y$ is given by $p\left(x,y\right) = q\left(x,y\right) \cdot \alpha\left(x,y\right)$, introducing the probability α of making the proposed step. Thus, the chance of remaining at the same position within the chain is given by $r\left(x\right) = 1 - \int_{\Re^n} q\left(x,y\right)\alpha\left(x,y\right)dy$. The unknown acceptance rate α is determined by the reversibility of the Marcov chain, called detailed balance:[56]

---

[9] In the framework of this thesis, a Markov chain is a sequence of states (a specific set of model parameters) within the target distribution, where the probability of changing to an other state only depends on the actual state.

$$\pi\left(x\right)p\left(x,y\right) = \pi\left(y\right)p\left(y,x\right). \tag{6.46}$$

Utilizing the symmetry of the used candidate-generating density $q\left(x,y\right) = q\left(y,x\right)$, the required acceptance rate to maintain reversibility is given by $\pi\left(y\right)/\pi\left(x\right)$.[56] This means, transitions towards the maximum of the posterior PDF are always made, transitions away from the maximum are possible but only with reduced probability:

$$\alpha\left(x,y\right) = \min\left(1, \frac{\pi\left(y\right)}{\pi\left(x\right)}\right) \tag{6.47}$$

Step width determination: Defining a suitable candidate-generating density is important for a fast convergence of the Markov chain towards the target distribution. A transition is proposed using a random walk chain $y = x + z$, where z is a random increment given by a Cauchy distributed random number. The spread is defined by the step-width for this parameter. Therefore, in a preparation phase, the step-width had to be adjusted for each parameter in a way, that the average acceptance rate was about 0.25. Independent derivations of this value are presented in reference [56]. If the acceptance rate for a given parameter was too high, the step width was increased, if it was too low, the step width was decreased.

Sampling of posterior PDF: In a second phase, samples were drawn from the Markov chain with constant step-width. These samples were used to calculate the most probable value and its error, by the mean value of all drawn samples and its standard deviation. Asymmetrical error bars were also determined by using only values, which are higher or lower than the mean value. This method was used for most of the profiles presented in the next chapter. But for some profiles another way was used, because for expectation values near the upper or lower boundary of the allowed parameter range, mean values can be misleading. The reason for this is that the candidate-generating density is disturbed by the boundary condition. An example is the emission profile of He^+. It has to be ≥ 0 and for the innermost values it is 0 due to the vanishing He^+ density. Deviations due to uncertainties can only be ≥ 0, leading to a shifted expectation value. A solution to this is to directly plot the marginal posterior PDF for this profile, represented by all samples drawn from the Marcov chain. In figure 6.4, a direct comparison between the mean value with asymmetric error bars and a visualization of the marginal posterior PDF is shown. The structures at the inner part of the profile in the left figure do not have a physical meaning. Calculating the mean value and its error from the clipped

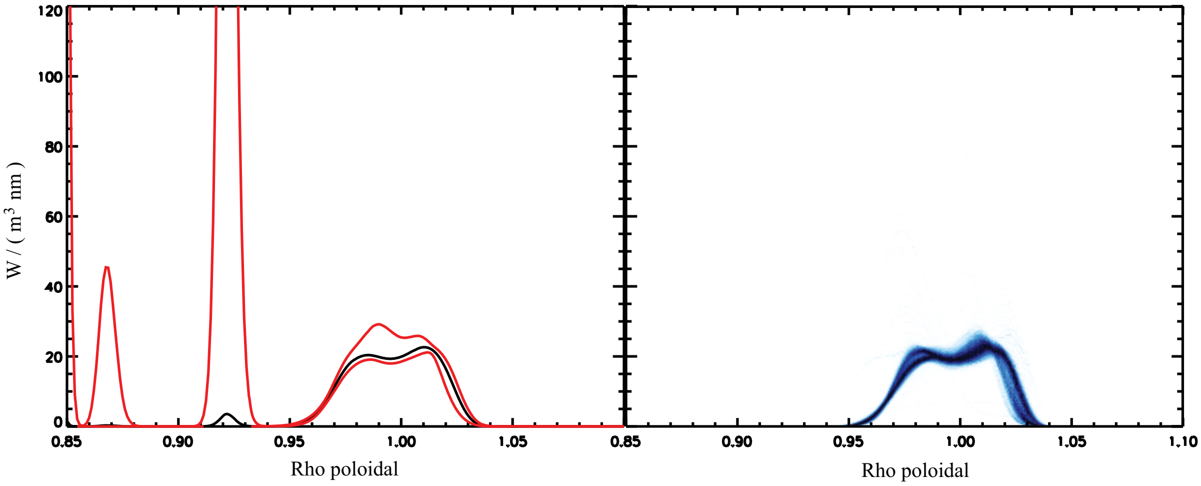

Figure 6.4: **Left:** Radial plot of the He II emission profile; mean value in black, assymetric 1-σ error bars in red;
Right: Histogram of the marginal posterior PDF

parameter space, resulting from applying the boundary condition, lead to these artefacts.

6.4.4 Model run-time

In this and the previous chapters, the forward model, the underlying physics and the "Marcov chain Monte Carlo"-algorithm were discussed in detail. But in the following chapters, which will present the results, more practical issues like the required effort of preparing the necessary edge profiles or the program run-time will gain importance.

At ASDEX Upgrade, there is no automated process to generate well aligned edge pedestal temperature and density profiles. According to requirements, there are two possibilities of profile fitting. One of them is to use the IDA fits to the electron density and temperature with a temporal resolution of 1 ms. The averaging over at least four IDA profiles for each evaluated time point, due to the exposure time of 4 ms of the new E_r diagnostic was carried out with due care. ELM affected profiles and radially displaced ones were filtered out manually. The other possibility is to use the AUGPed program. Intensive user interaction is require to created the ELM filtered well aligned modified hyperbolic tangent fits. Therefore, in both cases, the edge electron temperature and density profiles were prepared manually for each evaluated time point.

The run-time of the diagnostic can be separated in 3 phases. The first one is the already discussed Bayesian least squares fit to get near the optimal solution for arbitrary starting parameters. In most of the cases, this phase is completed within 5 to 10 minutes. In the next phase, the step-with of each model parameter is determined in order to reach the average acceptance rate of about 0.25. Typically, this was accomplished after about 2 to 4 million iterations. In the third phase, the estimations for the model parameters were determined by calculating the mean value out of 9 million samples, drawn from the Marcov chain. The deviation of this samples from the mean value gives the asymmetric error of each model parameter. Having to calculate the complete forward model for about 12 million samples[10], the run-time of the forward model is crucial. By putting great effort in run-time optimization and parallelizing on a Linux cluster, it could be reduced by a factor of 6 to 1.69 ms, which leads to a total runtime of about 5:30 hours.

---

[10] Each sample from the Markov chain includes a whole set of model parameters.

7 Sensitivity study

In the last chapter, Bayesian probability theory was introduced, which is the basis for the data evaluation in this work. One of the key topics was the integration of known uncertainties, in the measured data and in the model design (see section 6.2.2 and 6.3). But there are also additional not exactly known sources for uncertainties. One of them for example is given by using the equilibrium to map coordinates to ρ_{pol}. The effect of these not directly included uncertainties can be quantified by a sensitivity study.

7.1 First result

In this section, the results of the unmodified model and input profiles are discussed in detail to create a reference for the sensitivity study. But before that, a closer look on the underlying discharge #23227 has to be taken.

7.1.1 Discharge #23227

A set of overview plots of the typical parameters of the discharge #23227 can be seen in figure 7.1. It is a 1.0 MA discharge with an electron density of $4.0 \cdot 10^19\,\mathrm{m}^{-3}$ at the edge and $6.0 \cdot 10^19\,\mathrm{m}^{-3}$ at the center. The gas fueling is ramped up at the beginning and from 0.8 s it is kept constant until it is switched off at 2.5 s. During the discharge, the NBI heating is increased in several steps. Just after the ramp up at 0.3 s, 2.5 MW NBI is applied, which is increased at 0.9 s to 5.0 MW. Additionally, 1.3 MW ECRH heating is added at 1.5 s. From 2.8 s on, the heating power is increased to 7.5 MW and the gas fueling is switched off. The last step with 10.0 MW NBI starts at about 4.0 s. In each of these steps, a radial scan of the plasma is included to increase the resolution of the edge diagnostics (3 cm in 0.6 s towards the outer vessel wall and back again). The end of the discharge is initiated from 5.5 s on, by a fast stepwise reduction of NBI heating power, a gas puff and the ramp down of the plasma current. One time-point in each of the tree highest steps in NBI heating power (vertical lines in figure 7.1) will be analyzed in this and the following chapter. As indicated by the strong fluctuations in the H_α signal and a $H - L$ factor of near 1.0, the plasma is in H-mode during the analyzed time intervals. During the 5 MW phase with gas puff, there is a strong variation in the

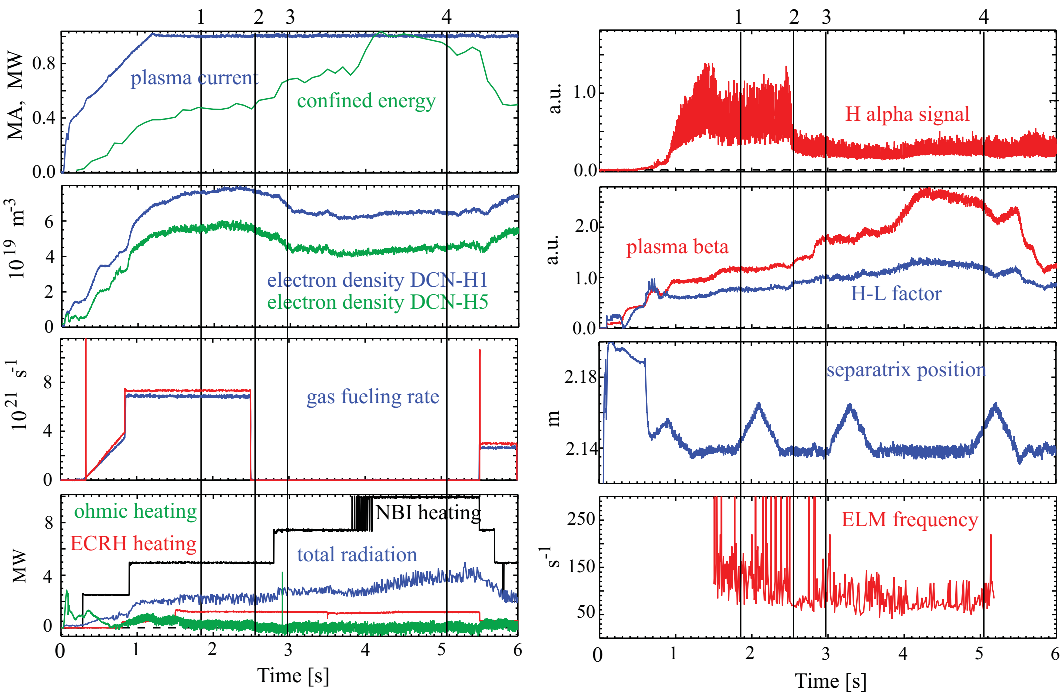

Figure 7.1: Important plasma parameters of the AUG discharge #23227

ELM frequency from 75-200 Hz. In the following two phases without gas puff the ELM frequency is reduced to 70 Hz with some exceptions up to 130 Hz. As already discussed, the exposure time of the presented diagnostic is 4 ms, therefore about 2 to 4 frames can be measured within one ELM cycle.

7.1.2 Results

The first result presented in this work will be discussed at full length to, introduce the different ways of visualization used in this and the following chapter. This section is structured in the following way. At first, a closer look on measured values and the corresponding output of the model is taken. Then, the directly derived radial profiles are discussed. Finally, the focus is shifted to the remaining radial profiles depending on the directly derived ones.

Line integrated fitting: In figure 7.2, one can see the measured spectrum (black dots) together with the assumed errors (solid red line) of one of the 17 LOS . The solid blue line, which is compared to the measurements, is the output of the model. Next to the

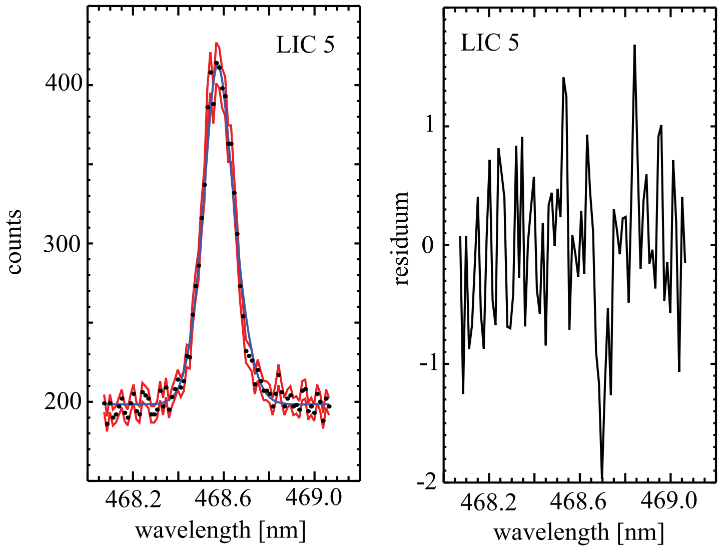

Figure 7.2: Comparison of measured spectra (black dots) of shot #23227 with the model output (solid blue line). The solid red line indicates the assumed measurement error from photon statistics and readout noise.

spectrum, the associated residual is plotted, which is given by

$$R_k = \frac{F_k - N_k}{\sigma_{D,k}} \tag{7.1}$$

(see equation 6.22), where N is the number of measured photons with uncertainty σ_D. F is the model output. The overall deviation of the measurements from the model within one sigma indicates, that the measurement error is defined realistically and that the model is flexible enough to reproduce all features of the measured data.

Radial profiles: The just presented output of the forward model is, as already described in section 6.2.1, created by summing up local line emission spectra along the line of sight. These local spectra are determined by three radial profiles realized as model parameters: the emission profile, the He^+ temperature profile and the He^+ velocity profile. In figure 7.3, the estimates of two of these profiles are shown. The He^+ velocity profile is not plotted, because its projection is directly calculated for the discrete points along each line of sight and therefore the unprojected, LOS independent radial profile is not available. Looking at the emission profile in figure 7.3, it can be seen that this profile is well determined by the measurement. The skipping of the outermost LOS, discussed at the end of chapter 5, leads to an increase of the uncertainties outside the separatrix. From about $\rho_{pol} = 1.02$, the rapidly decreasing photon emission coefficient, which is dependent on electron temperature and density, causes a steep gradient in the emission profile. The error bars are also decreasing, due to the neglected uncertainty[11] of the PEC for low densities and temperatures. This profile defines the range ($0.95 < \rho_{pol} < 1.05$ for this discharge and time point), in which the different radial profiles can be estimated by the presented diagnostic. The result for the estimated He^+ temperature profile (right picture in figure 7.3) is consistent with this results, because for $\rho_{pol} > 1.03$ the temperature is too low to get a significant amount of singly ionized He.

---

[11] The uncertainties of the PEC file are not included directly in the model. Therefore, the vanishing error bars of the emission profile in the scrape off layer are not based on increased accuracy, but only

Secondary radial profiles: The radial emission profile, discussed in the last paragraph, can be used to derive the He^+ density profile, taking into account the considerations from chapter 3. Recalling equation (3.18)

$$\langle P \rangle = n_{He^+} \cdot n_e \cdot \mathrm{PEC}_{\mathrm{excit}}\left(n_e, T_e\right) \cdot E_{Ph} \qquad\qquad E_{Ph} = \frac{hc}{\lambda_{4\to 3}}$$

the electron density and temperature has to be included in the forward model. For this discharge (#23227), these two profiles are taken from the IDA diagnostic. Figure 7.4 shows the electron density profile and the electron temperature profile. As already discussed in chapter 6.2.1 during the introduction of the forward model, a free spline is added to these profiles. It can be seen, that the deviation from the measured profiles is very low. The reasons for this are on the one hand, the small error bars of the IDA profiles and on the other hand, additional information from the measured data as well as restrictions due to the boundary conditions. Therefore, these error bars do not represent the absolute error of the electron density and temperature profiles, but only the range in which they vary during parameter estimation. The effects of larger variations due to uncertainties in radial position will be discussed later in this chapter. In the left picture of figure 7.5, the resulting profile of the He^+ density is plotted. Being directly derived from the emission profile, which vanishes for $\rho_{pol} < 0.95$, the He^+ density also has to vanish towards the plasma center. Due to the accurate decaying wing of the emission profile, the error bars of the He^+ density are also very small. In the SOL for $\rho_{pol} > 1.02$, the error bars are increasing due to the decaying emission profile and the vanishing electron temperature. The not included uncertainties of the PEC files, the position uncertainties of the equilibrium reconstruction and the not exactly known shape of the electron temperature in the SOL lead to a much greater real uncertainty outside the separatrix. This is discussed in detail in the following section.

Radial electric field: The last model parameter that needs to be discussed is the radial electric field. It is connected to the total velocity profile, the He^+ pressure profile and the emission profile. Because the emission profile acts as weights in the line integrated spectrum, the radial electric field can be determined only in those regions which have a significant emission. In the right plot of figure 7.5, one can see the radial electric field for the discharge #23227 and for comparison in blue the emission profile together with the error bars. The minimum in the field, which is the interesting edge structure, this

---

on the strongly decreasing PEC data. Derived profiles have to be treated with care in this region due to the underestimated uncertainties.

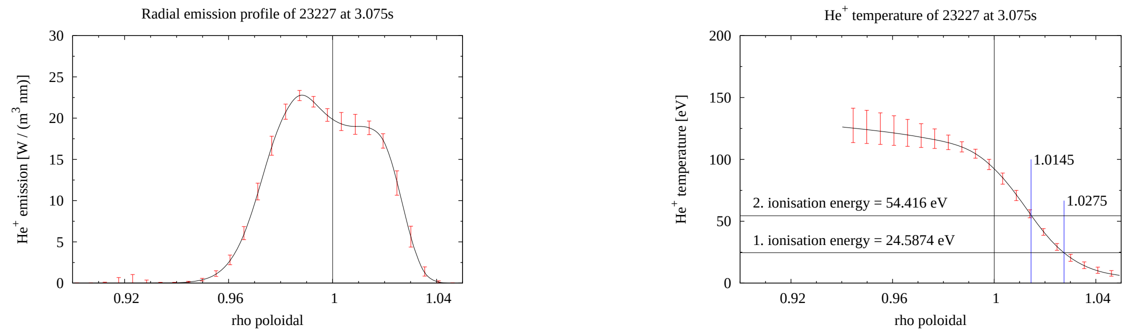

Figure 7.3: Profiles directly related to the measured data; the black line represents the mean value derived from the Markov chain; in red the associated 1σ uncertainty is given; the two blue lines mark the radial positions where the first and second ionisation energy is reached

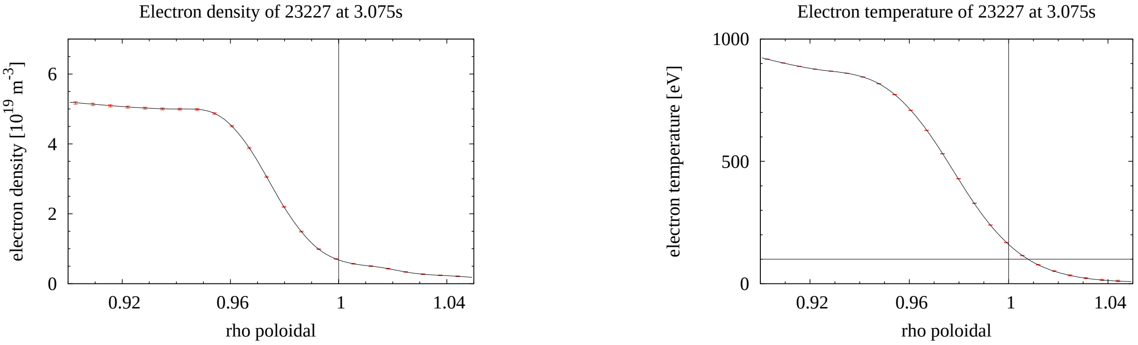

Figure 7.4: Applied electron density and temperature profiles for He^+ density estimations using PEC

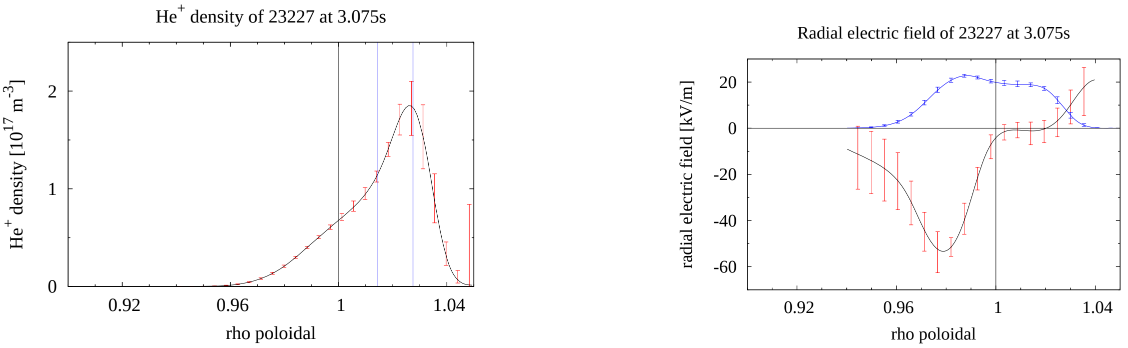

Figure 7.5: Being dependent on the emission profile both profiles are restricted to areas with sufficient He^+ emission $(0.94 < \rho_{pol} < 1.04)$
Left: The blue lines mark the first and second ionisation energy of He
Right: Emission profile is scaled and re-plotted in blue to identify the significant region

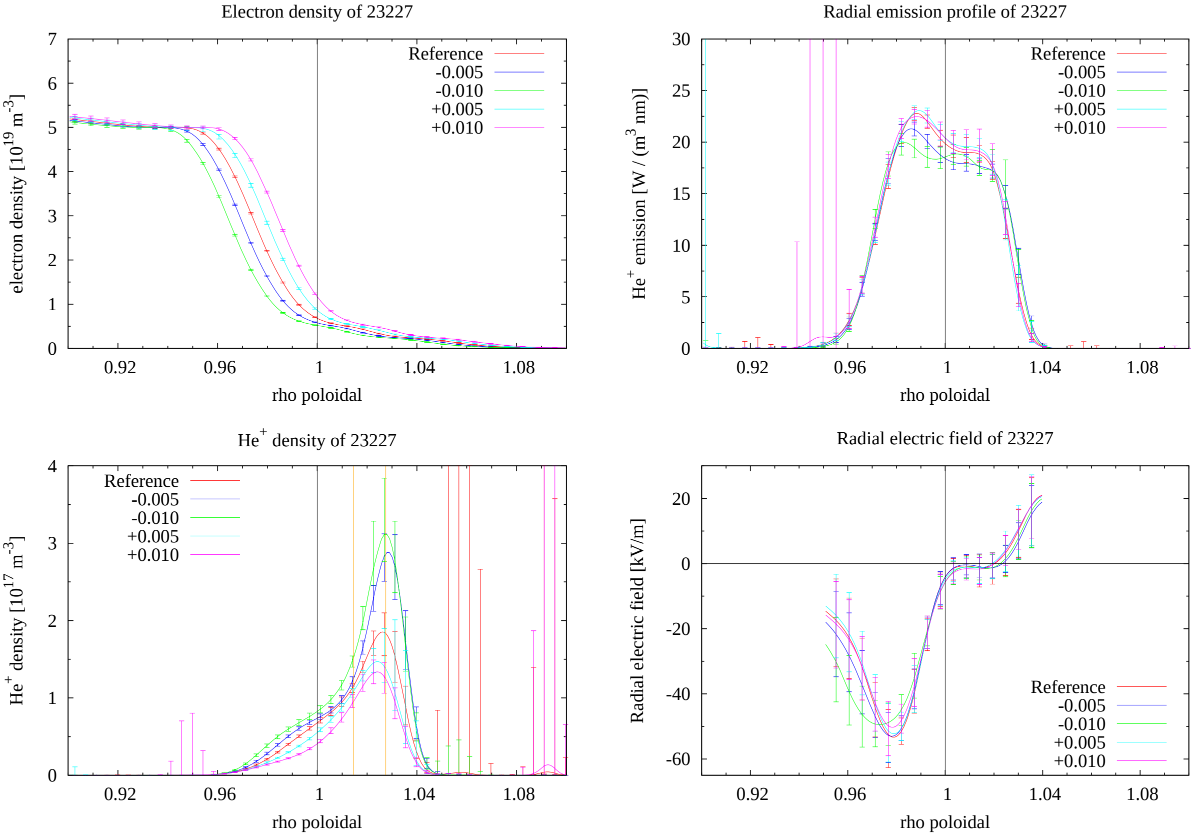

Figure 7.6: Different radial shifts of the electron density are shown; this affects only the He^+ density; emission profile and radial electric field vary only within the error bars

work is concentrating on, is situated in the region $0.96 \leq \rho_{pol} \leq 1.0$, having sufficient intensity.

7.2 Variation in equilibrium reconstruction

After the discussion of the parameters of discharge #23227 and the output of the unmodified model, its dependency on the profile reconstruction can be analyzed. This is done by varying the positions of the electron density, electron temperature and toroidal velocity profile. As already discussed in section 4.2, the positions of these profiles are very sensitive to the equilibrium.

Variation of the electron density profile: At the beginning of this chapter and also in earlier ones, the neglected uncertainties due to equilibrium reconstruction and due to position uncertainties of the plasma edge diagnostics were mentioned. The effect of small shifts (see top left graph in figure 7.6) in the electron density profile on the estimated profiles are now explored. An important result is, that the radial electric field is not affected from these variations (see lower right graph in figure 7.6) within the error bars. The reasons for this are the unchanged emission (top right graph), velocity and He^+-temperature profiles, which are directly dependent on the measurements. The remaining He^+ density profile therefore has to be very sensitive to the electron density variations. Due to the change in slope of the electron density (top left graph) at about $\rho_{pol} = 1.01$ and also due to the change in slope of the photon emission coefficient at about 100 eV, which is also at about $\rho_{pol} = 1.005$ (see figure 7.4), the effects on the He^+ profile have to be separated in two regions. One is the region around the separatrix and further inwards ($\rho_{pol} < 1.01$), the second one is the scrape off layer ($\rho_{pol} > 1.01$). In the inner, well determined[12] region with high temperatures, the large changes in the electron density due to the steep gradient of the pedestal only lead to small variation in the He^+ density. In the outer, very uncertain[13] region with low electron temperatures, small changes in electron density result in strong variations of the He^+ density. In conclusion, He^+ profiles can only be trusted in the inner region ($\rho_{pol} < 1.01$), assuming that the shape and the position of the electron temperature and density are accurate enough.

Variation of the electron temperature profile: As well as the just discussed uncertainty of the electron density profile position, also the effects of a uncertain electron temperature position were analyzed. Figure 7.7 shows the most important profiles. As already mentioned, due to the strong H-mode, the electron temperature of the reference was chosen slightly above the 100 eV at the separatrix. As expected, the emission profile and the radial electric field are stable against variations of the electron temperature, because of the direct dependence of these profiles on measured quantities. In analogy to the variation of the electron density, the He^+ density profile is strongly affected by the electron temperature variations. In contrast to electron density variations, only the scrape off layer part of the profile varies larger than the error bars. Reason for this is the flat gradient in the photon emission coefficient for electron temperatures higher than about 100 eV, followed by a steep gradient for lower temperatures (see figure 3.3). This supports the results from the last paragraph: The estimated He^+ densities can only be trusted in the region $\rho_{pol} < 1.01$. The shape is more sensitive to the position of the electron density rather than the position of the electron temperature.

---

[12] This region is well determined, because the photon emission coefficients are accurate for high densities and temperatures. Furthermore, the emission profile is covered well by the used lines of sight. Also the shape and absolute value of the electron temperature and density profiles is more accurate inside the separatrix than in the SOL.

[13] This region is very uncertain, because the photon emission coefficients are not accurate for the low temperatures and densities in the SOL and are governed by steep gradients leading to large variations for small changes. Furthermore, the shape and absolute values of the electron density and temperature can only be measured with large error bars. Additionally, the LOS exclusively covering this region suffer from reflections and have to be excluded from the calculation.

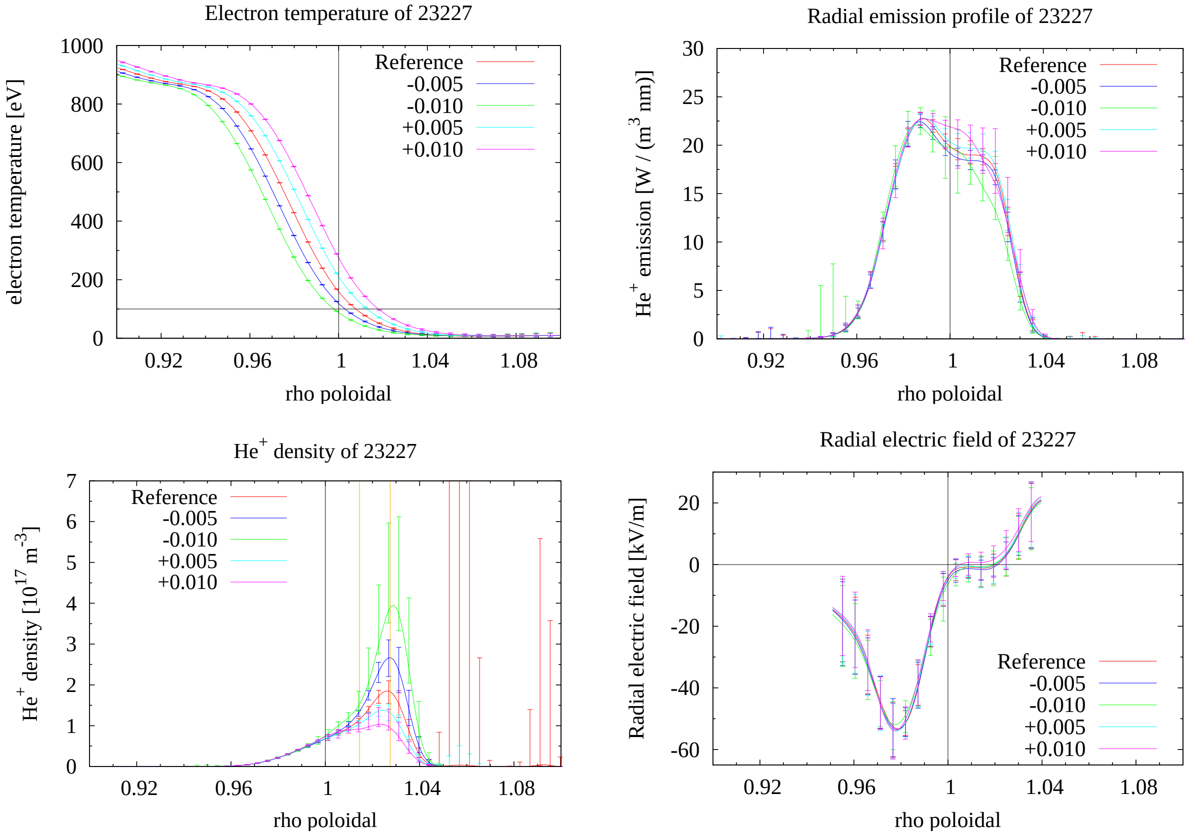

Figure 7.7: Different radial shifts of the electron temperature are shown; this affects only the He^+ density; emission profile and radial electric field varies only within the error bars

Variation of the toroidal velocity profile: Finally, to close the discussion of the equilibrium reconstruction, a closer look on the toroidal velocity profile was taken. The effects of uncertainties in the equilibrium (ρ_{pol} position; blue and green profiles) as well as variations in the magnitude (vanishing velocity: magenta, doubled velocity: cyan) and also different shapes (magenta and brown) are analyzed in figure 7.8. One can see, that radial variations only cause changes in the estimated profiles within the error-bars. The largest variations, that can be seen in the radial electric field are still within the error bars. They are caused by neglecting (magenta) and doubling (cyan) the toroidal velocity. The radial electric field is affected by the variation, because it is the only term contributing to the total velocity profile along each LOS, that can react to the variation (see equation 6.10):

$$v_{He^+}|_{LOS} = [\vec{v}_{E\times B} + \vec{v}_{dia} + \vec{v}_{tor}]_{LOS}\,.$$

The total projected velocity is determined by the measurement and the diamagnetic velocity by the He^+ pressure. Both of them do not change during the variation of the toroidal velocity. Small position uncertainties (blue and green) as well as neglecting the minimum in the toroidal velocity near the separatrix (brown) lead to no significant changes in the estimated profiles, reinforcing the assumption, that the toroidal velocity

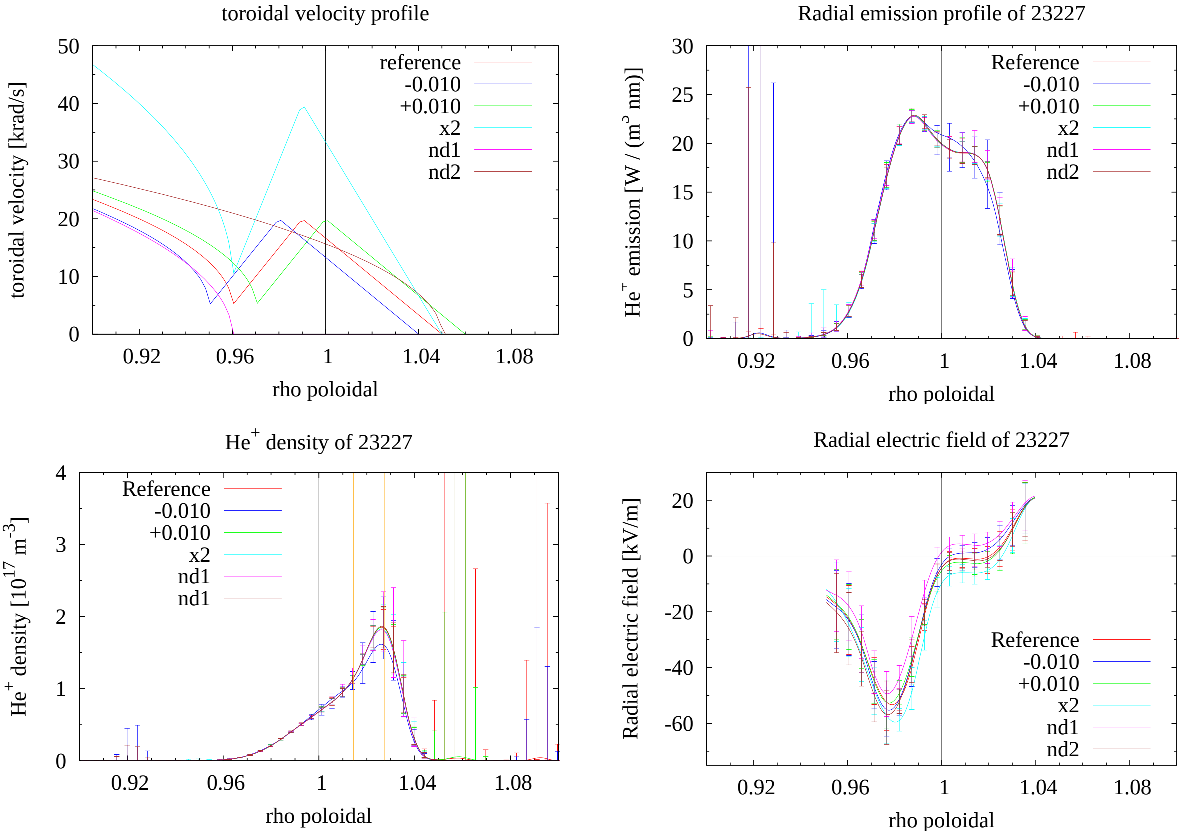

Figure 7.8: Variations of the toroidal velocity profile: this includes a radial shift $\rho_{pol} \pm 0.01$, an artificial magnitude increase by a factor of two and variations of the shape

is only a small correction due to the nearly perpendicular lines of sight (see section 6.2.1).

The considerations in this section on variations of the input profiles due to uncertainties of the equilibrium lead to the conclusion, that on the one hand the determination of the radial electric field is independent of these variations and on the other hand the shape of the determined He^+ density is very sensitive to these variations. All other estimated profiles are independent on uncertainties due to the equilibrium.

7.3 Effects due to He II fine structure

As already mentioned at the end of chapter 3.2, the effect of the neglected fine structure splitting and the Paschen-Back effect on the determined radial electric field is discussed in this chapter. In figure 7.9, three radial electric fields are compared. The red one is

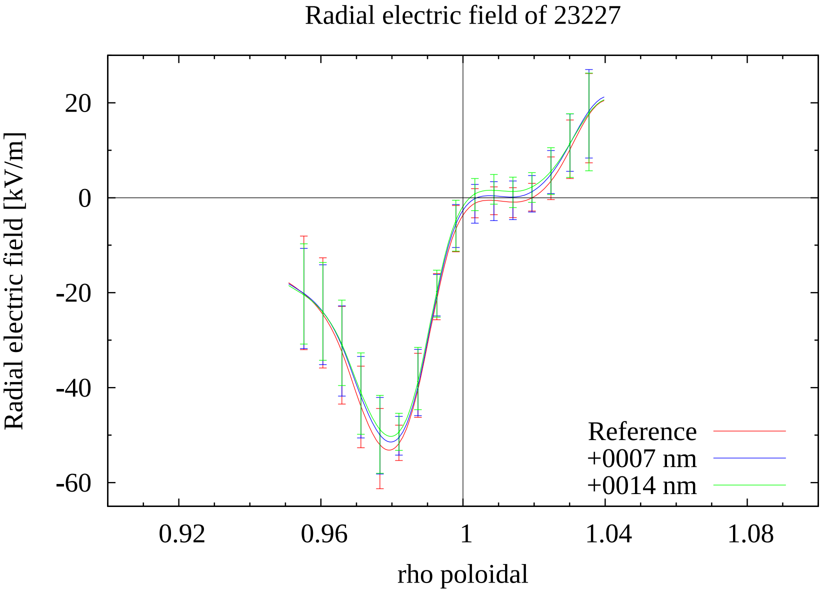

Figure 7.9: Variation of the central wavelength of the He II line due to finestructure and Paschen-Back splitting

the reference case used during the complete sensitivity study. In the blue one, a shift of the central wavelength by 0.0007 nm is included, which corresponds to the estimated displacement of the central wavelength for an He^+ ion-temperature of 100 eV (see figure 3.5). In green, the doubled shift of the central wavelength is assumed, which would be caused by a He^+ ion-temperature of only 15 eV. It can be seen, that the variation of the radial electric field is below the error bars. This justifies the simple approach utilized in this work.

7.4 Possible experimental improvements

Based on the measurement uncertainties and the results of the sensitivity study, the following improvements to the diagnostic could lead to a significant improvement of the derived radial electric field. The two most promising modifications of the experimental setup would be to use only one spectrometer, capable of measuring all LOS, and to increase the temporal resolution to 1 ms or below. The first measure would make the cross calibration of the wavelength between the two spectrometers obsolete and the second one would allow to resolve the development of the E_r well during the ELM cycle. This would enable a detailed study of the ELM crash for different ELM types, or to address the question whether the increased depth of the radial electric field well is the cause or a consequence of the steep edge profiles in H-mode. An increased number of lines of sight and thus an increased radial resolution, combined with a better spectral resolution,

would even more increase the accuracy of the results and release the restriction of only being able to analyze H-mode discharges.
Another possible improvement of the E_r diagnostic, focusing on the run-time of the "Markov chain Monte Carlo"-code, would be a complete re-implementation of the forward model using the parallel computation power of graphic cards. This new and quickly developing possibility of performing independent massive parallel calculations is particularly suitable for drawing samples from Marcov chains.

8 Results

The sensitivity study in the last chapter has proven the stability of the radial electric field estimation against small variations of input profiles not covered by the error propagation. This chapter now will focus on the results for different discharges and time points.

8.1 Previous radial electric field measurements

To introduce the discussion of the results, a short overview of the findings from other measurements at ASDEX Upgrade and also from other Tokamaks is presented in the following.

Up to now, the only system, that was capable of measuring radial electric fields just inside the separatrix at ASDEX Upgrade was Doppler reflectometry. Fluctuation measurements are used to directly derive the radial electric field and its shear.[61],[26] A minimum just inside the last closed flux surface is measured in H-mode, which has a fixed width and a depth that is dependent on the confinement. The measured depth for typical H-modes is about -40 kV/m and in improved H-modes up to -50 kV/m.
Much deeper radial electric fields were measured at the plasma boundary of Alcator C-Mod by charge exchange recombination spectroscopy.[62] This Tokamak has a high magnetic field ($\approx 5\,\mathrm{T}$) and a very narrow pedestal (2-6 mm). The toroidal and poloidal rotation velocity of a certain impurity species, together with its temperature and density is used to calculate the E_r-profile, applying the radial force balance equation. The typical E_r fields in H-mode have a depth of about -75 kV/m, but vary dependent on the plasma parameters between -30 kV/m and -120 kV/m. The width of these fields is about 5 mm and show no variation. In ELM free H-modes the depth of the minimum rises up to -300 kV/m.
The JT60-U Tokamak also has a high toroidal magnetic field (4 T), but additionally a high plasma current of up to 5 MA.[63] The radial electric field at the plasma boundary is measured by charge exchange recombination spectroscopy. In reference [64] a radial electric field is presented with a minimum up to -80 kV/m in H-mode.
The DIII-D Tokamak [65] has a pedestal width of about 1-2 cm, which is in the same order of magnitude as the pedestal width of ASDEX Upgrade. Also the plasma parameters like the confining magnetic field and plasma current are very similar. The measured radial electric fields in H-mode have a typical width of about 1 cm and a depth of -12 kV/m

up to -30 kV/m.[66] In ELM-free H-modes, a depth of up to -100 kV/m was measured. Furthermore, it was found, that decreasing triangularity reduces the depth of E_r and increases the width.[67]

8.2 Comparison to theory

In chapter 2, the theoretical background for this work was discussed and a derivation of the neoclassical radial electric field was given. Additionally, it is possible to make an approximation for the radial electric field, by analyzing the pressure and density of the main ions.

$\nabla p/n$ approximation: The radial force balance equation (2.19) derived in chapter 2 has to be valid for each ion species a separately. But the radial electric field E_r, which is a global plasma property, has to be the same for each species:

$$\vec{V}_{a\perp}^{(1)} = \frac{\partial p_a}{q_a n_a \partial r} - E_r .$$

If one now assumes, that the velocity perpendicular to the magnetic field lines is small for the main ions, it is possible to derive an approximation for the radial electric field:

$$E_r\,[V/m] \approx \frac{\nabla P_D\,[Pa/m]}{q_D\,[C]\cdot n_D\,[m^{-3}]} \cdot \frac{k_B\,[eV/K]}{k_B\,[J/K]} \cdot 1.6022 \cdot 10^{-19} \left[\frac{C\cdot V}{eV}\right]. \tag{8.1}$$

By applying two simplifications, this equation can be solved completely with profiles that are included in the forward model. Therefore they are easily accessible. The main ion density n_D is assumed to be proportional to the electron density $n_D = \alpha n_e$ and the main ion temperature is approximated[14] by the electron temperature $T_D \approx T_e$. This leads to the following expression for the $\frac{\nabla p}{n}$-term:

$$\frac{\nabla P_D}{n_D} = \frac{\nabla\left(T_D \cdot \alpha n_e \cdot k_B\right)}{\alpha n_e} = \frac{\nabla\left(T_D n_e k_B\right)}{n_e} \approx \frac{\nabla P_e}{n_e}. \tag{8.2}$$

In the following sections of this chapter, the measured radial electric fields are compared to the approximated ones in order to verify, if the assumption of small perpendicular velocity of the main ions is correct.

---

[14] At ASDEX Upgrade, this assumption is only applicable for high collisionalities. In general the ion temperature is higher than the electron temperature but the gradient of the ion temperature in the pedestal is smaller than the gradient of the electron temperature.

Neoclassical radial electric field: A more advanced derivation of the radial electric field, using neoclassical theory was also given in chapter 2 by equation (2.43):

$$E_{r,neo} = \frac{T_D}{q_D}\left[\frac{\partial \ln P_D}{\partial r} - (\beta_1, g_{2i})\frac{\partial \ln T_D}{\partial r}\right].$$

This equation corrects the $\frac{\nabla p}{n} = T \cdot \frac{\partial \ln p}{\partial r}$ term, discussed in the last paragraph, by the internal friction of the main ions, which is dependent on the main ion temperature T_D and the collisionality ν_*. From the Banana regime to the plateau regime (β_1, g_{2i}) is given by equation (2.40):

$$(\beta_1, g_{2i})_{bp} \simeq \frac{1.17 - 0.35\nu_{*i}^{1/2}}{1 + \nu_{*i}^{1/2} 0.7}.$$

The continuation from the plateau regime to the collisional regime is given by equation (2.41), which is the relevant one for the plasma analyzed in this chapter:

$$(\beta_1, g_{2i})_{pc} \simeq \frac{(\beta_1, g_{2i})_{bp} - 2.1\nu_{*i}^2\epsilon^3}{1 + \nu_{*i}^2\epsilon^3}.$$

As already mentioned in the previous paragraph, the main ion density is assumed to be proportional to the electron density and the main ion temperature is assumed to be equal to the electron temperature. The collisionality ν_* is defined by the effective main ion collision frequency ν_{eff} divided by the trapped particle average bounce frequency ω_b [60]:

$$\nu_* = \frac{\nu_{eff}}{\omega_b} = \frac{\nu_D/\epsilon}{\epsilon^{1/2} v_{th}/(R_0 q)} = \frac{\nu_D \cdot R_0 \cdot q}{\epsilon^{3/2} \cdot v_{th}}. \tag{8.3}$$

The thermal velocity of the main ions is given by

$$v_{th}\left[\frac{cm}{s}\right] = \sqrt{\frac{k_b\,[J/K] \cdot T_D\,[K]}{m_a \cdot m_p\,[kg]}}, \tag{8.4}$$

where m_a is the main ion mass divided by the proton mass m_p(in the case of Deuterium $m_a = 2$).[2] The inverse aspect ratio ϵ associated to a flux surface is defined by

$$\epsilon = 0.5 \cdot \frac{R_L - R_H}{R_0}, \tag{8.5}$$

where R_0 is the radial position of the plasma center ($\rho_{pol} = 0$). R_L and R_H are the radial positions of the associated flux surface at the mid-plane on the low-field side and on the high-field side. The radial q-profile is determined by the equilibrium reconstructed by the CLISTE code. The collision frequency of the main ions ν_D is given in reference [4] by

$$\nu_D\,[1/s] = \frac{n_D\,[m^{-3}] \cdot Z_a^4 \cdot \ln\Lambda}{6.60 \cdot 10^{17} \cdot \sqrt{m_a} \cdot T_D^{3/2}\,[keV]}, \tag{8.6}$$

with a main ion charge q_D divided by the electron charge e of $Z_a = (q_D/e) = 1$ for Deuterium. $\ln\Lambda$ is called the Coulomb-logarithm and is also defined in [4]:

$$\ln\Lambda = 17.3 - \ln\left(\frac{\sqrt{n_e}\,[m^{-3}]}{T_D^{3/2}\,[keV]\cdot 10^{10}}\right). \tag{8.7}$$

Similar to the $\nabla p/n$ approximation for the radial electric field, discussed in the last paragraph, the neoclassical prediction also depends only on parameters that are included in the forward model. Therefore, it can be easily calculated and compared with the measured radial electric field. If an agreement between neoclassical prediction and measurement is found, this would indicate, that in the region with strong shear in the radial electric field, neoclassical transport is dominant and the turbulent transport is suppressed, like it is predicted by H-mode theory already discussed in chapter 2.

8.3 Effect of ELMs

The first result presented in this chapter is the evolution of the estimated E_r profiles during one ELM cycle, which is essential for all further considerations in H-mode discharges. As already discussed in the introduction, the edge density and temperature profiles collapse on a regular basis, explained by the peeling-ballooning theory. This is connected to a collapse of the edge transport barrier and also to a collapse of the radial electric field. In the following, three consecutive ELM cycles of the discharge #23227 will be discussed. This is the same discharge, which was already used during the sensitivity study. The most important profiles are shown in figure 7.1 of the previous chapter. The selected time slice is indicated by the second vertical black line at about 2.55 s. This time, region was chosen, because it is just after switching off the gas puff and has the lowest ELM frequency (≈ 80 Hz) of the whole discharge. The integration time of 4 ms allowed the evaluation of 3 profiles within one ELM cycle. Sub-figure a) in figure 8.1 visualizes the selected time interval and introduces the color-coding for the other plots in this figure. The structures in the line integrated intensities (stars), measured by one line of sight and plotted over the time, show good agreement with the onset of the ELMs (vertical brown lines). The reason for this is the increased influx of neutral Helium, caused by increased recycling due to the large energy and particle transport towards the walls. The radial profiles of the three time-points relative to the ELM onset are plotted in sub-figures b) to e) of this figure. The break-down of the transport barrier is clearly visible in all of these profiles: in the density profile, which has a strongly reduced gradient, in the temperature profile by a reduced pedestal top value, in the reduced radial electric field minimum and in the emission profile with increased emission in the scrape-off layer. Looking at the estimated radial electric fields in sub-figure b), one can see a significantly reduced radial electric field (red). But it has a clear minimum, which is still about 50 % of the inter ELM value. The reason for this is the relatively long exposure time of 4 ms compared to

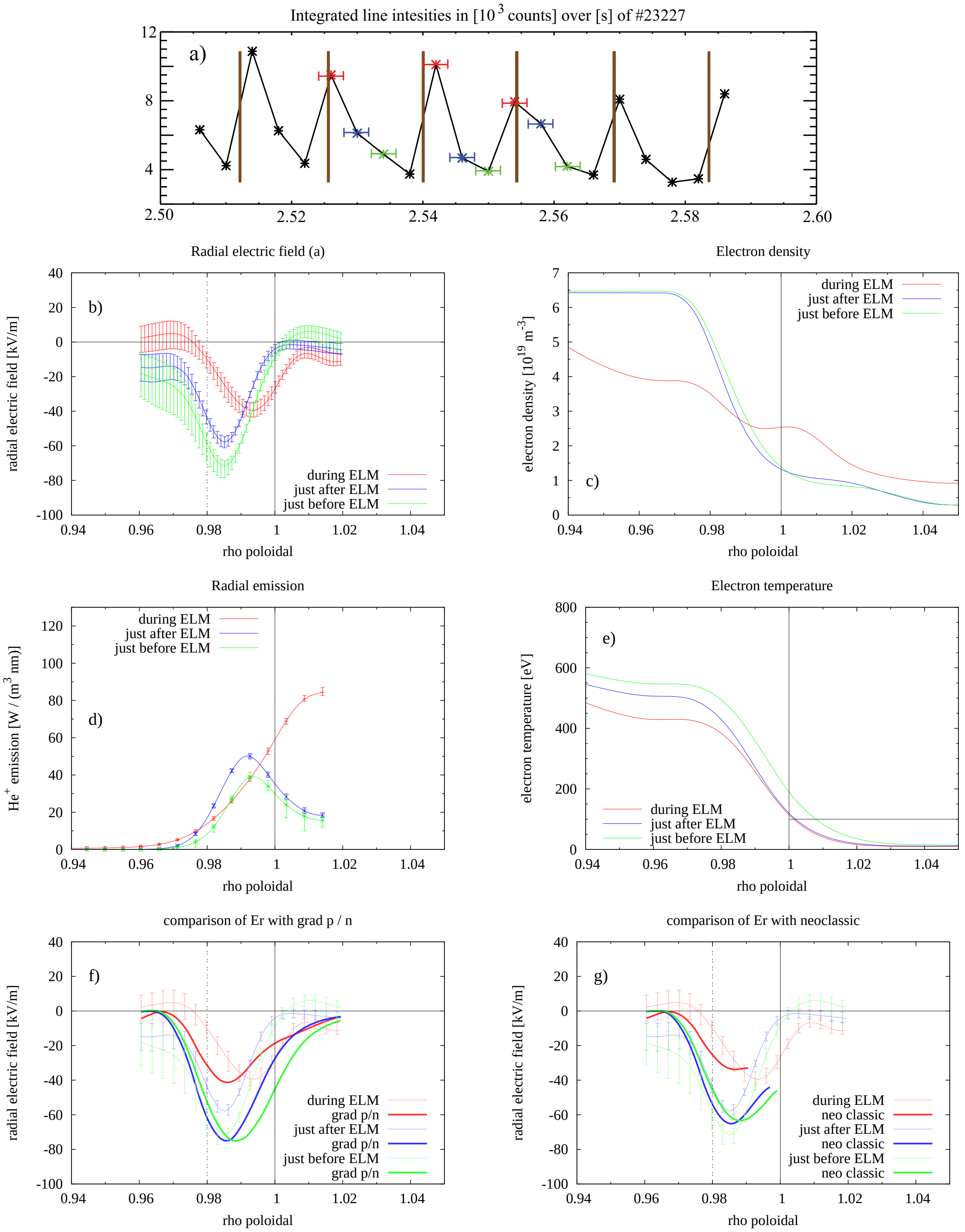

Figure 8.1: Evolution of the measured radial electric field, the electron density profile, the temperature profile, the emission profile during the ELM cycles of discharge #23227; the time-points in the same color are evaluated at the same time

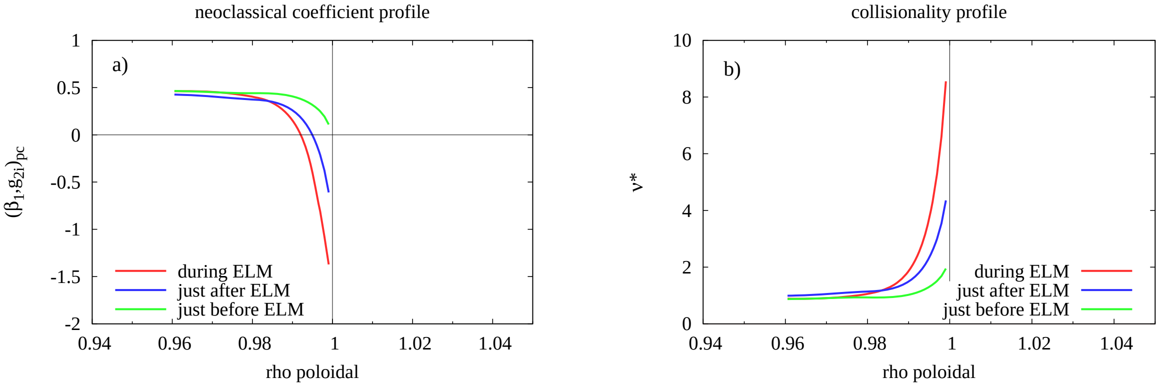

Figure 8.2: Radial profiles of the neoclassical coefficient related to the flux driven by the ion temperature gradient a) and of the collisionality b)

the fast recovery of the edge profiles. In the next time-point (blue), the edge profiles and the radial electric field have almost recovered their shape from before the ELM crash. Comparing the positions of the minima of the radial electric fields in sub-figure b), they are situated in the region $0.98 < \rho_{pol} < 1.00$ marked by the solid and dashed vertical lines. No conclusions regarding this position can be made, because the combined uncertainties of the lines of sight, the input profiles and the equilibrium reconstruction are about $\Delta\rho_{pol} \approx 0.02$ (or $\approx 1\,\mathrm{cm}$).

The two sub-figures f) and g) in figure 8.1 show a comparison of the estimated radial electric fields during the ELM-cycle, with $\nabla p/n$ and the neoclassical prediction presented in the first section of this chapter. $\nabla p/n$ agrees well in depth within the error bars in the time-point containing the ELM (red) and in the one just before the next ELM (green), indicating that the perpendicular main ion velocity has to be very small (see equation (2.19)). During the recovery phase of the field (blue) there is a significant deviation.
The radial electric fields predicted by neoclassical theory in plot g) show better agreement than $\nabla p/n$ due to the corrections related to the collisionality and the temperature gradient. The depth of the two time-points within the ELM (red) and just before (green), which were described well by $\nabla p/n$, were reproduced also by the neoclassical prediction within the error bars. But with neoclassics, the depth of the blue profile can also be predicted correctly. The reason for this is the temperature and collisionality dependent term (see equation 2.43). In figure 8.2 the collisionality profiles and the profiles of the resulting neoclassical coefficients are plotted. The coefficient is positive for all three cases at the position of the minimum ($\rho_{pol} \approx 0.99$), leading to a flatter radial electric field compared to $\nabla p/n$. The two profiles in the recovery phase of the ELM crash are modified more strongly than the one directly at the crash due to the reduced collisionality and the steeper edge gradients.

8.4 Plasma parameter scans

This section concentrates on scans of important plasma parameters in H-mode plasma. Only time-points just before an ELM are used for data evaluation, to ensure the comparability of these ELM synchronized radial electric fields at maximal depth.

8.4.1 NBI heating power scan

The first parameter scan discussed in this chapter is a variation of the heating power. Because the stored energy of the plasma increases with heating power, this is an important parameter. In figure 7.1, the most important time-traces are plotted and the used time-points are indicated by black vertical lines. Four time-points were selected, two at 5 MW NBI heating power with and without gas puff, one at 7.5 MW heating power and one at 10 MW heating power. The results are presented in figure 8.3. The smooth and accurately aligned electron density and temperature profiles (sub-figures b) and d)) are determined by ELM synchronized averaging over the complete radial sweep at each heating power level using the AUGPed program. The time-point with 5 MW NBI heating and no gas puff did not have a radial sweep, therefore less measurements were available for profile reconstruction. Sub-figures a) and c) show the results for the radial emission profile and the radial electric field. The first time-point (black) with the strong gas puff has on the one hand a much higher He II emission and electron density than the other time-points, but on the other hand relatively flat edge gradients and a flat radial electric field. Switching off the gas puff (magenta) without changing the heating scheme does not change the depth of the measured radial electric field but strongly increases the edge gradients. A significant change in the E_r is achieved by increasing the heating power from 5 MW to 7.5 MW (orange profile), accompanied by an even steeper edge gradient in electron temperature. The last step in heating power from 7.5 MW to 10.0 MW (green profile) does not follow the trend. The radial electric field does not get significantly deeper and the edge temperature gradient even flattens again.

A comparison of the measurements to $\nabla p/n$ and the neoclassical prediction is presented in sub-figures e) and f). In e) the focus is on the depth of the measured radial electric field minimum compared to theory, while f) emphasizes the deviation of the measurement and the neoclassical prediction from $\nabla p/n$. Looking at the first two time-points (black and red), which differ only in gas puff level, $\nabla p/n$ gets significantly deeper if the gas puff is switched off, due to the much steeper edge gradients. However, the depth of the measured radial electric field nearly stays constant, which is correctly predicted by neoclassical theory. Important is the change of sign in the neoclassical coefficient due to decreased collisionality, visualized in sub-figure g) and h). Increasing the heating power to 7.5 MW (blue profiles) lowers the collisionality even more and increases the edge gradients. This leads to a deeper $\nabla p/n$ prediction which is over corrected by neoclassical theory compared to the measurement. A possible reason for this is the

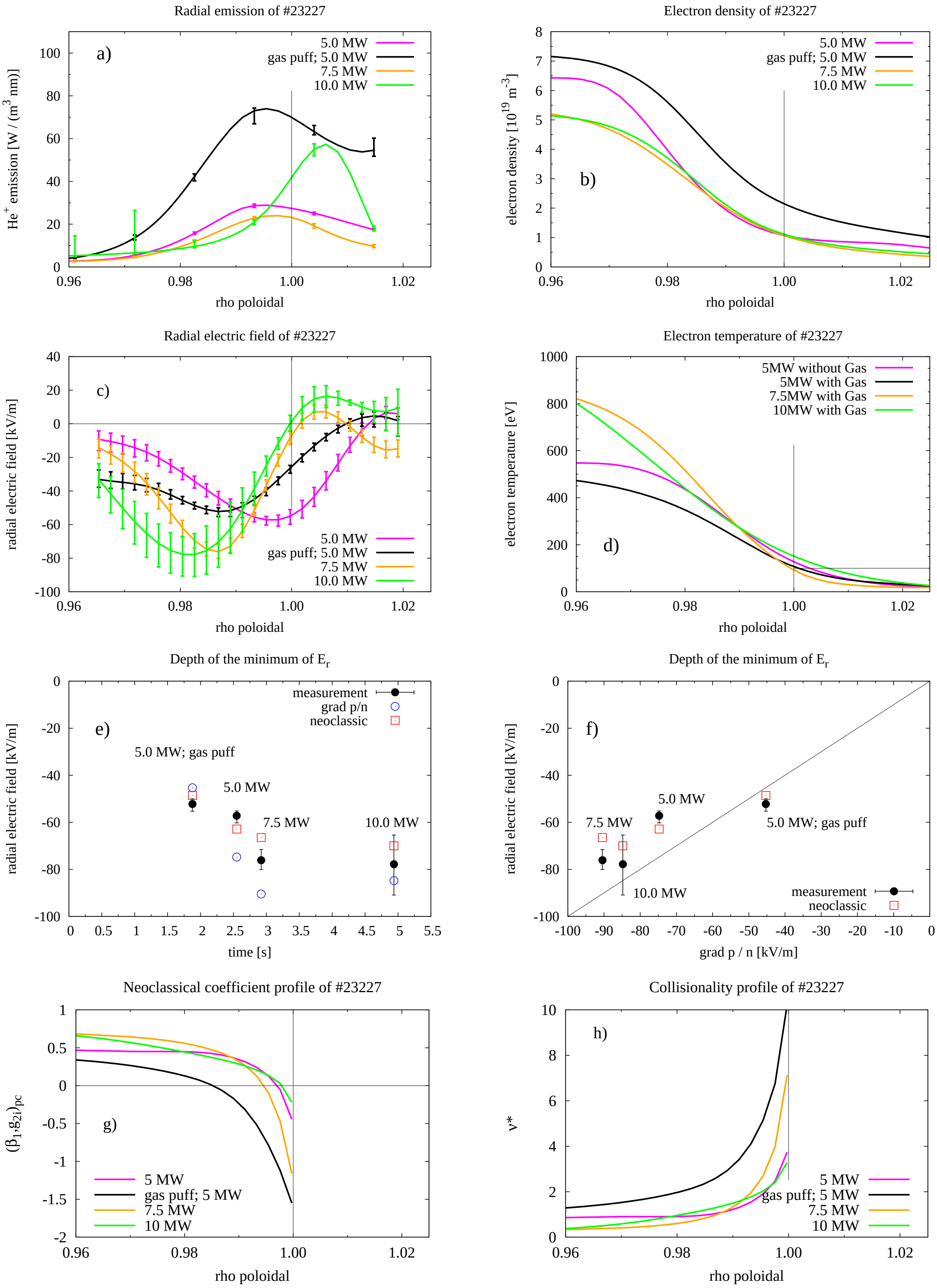

Figure 8.3: Evolution of the measured radial electric field, the electron density and temperature profile as well as the He II emission profile for different levels of NBI heating

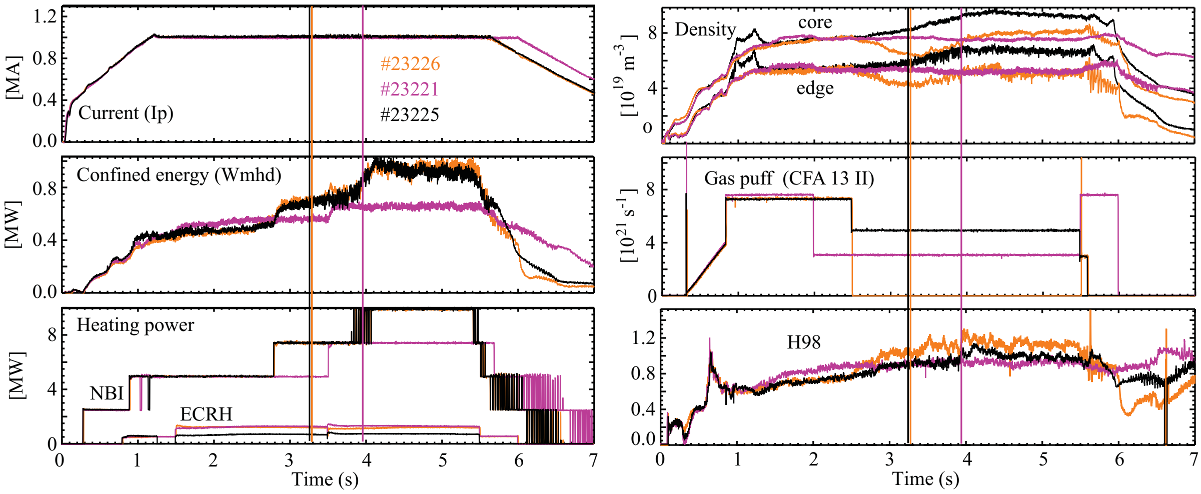

Figure 8.4: Overview of the discharges used for the gas-scan. The profiles of each discharge are plotted in the same color. The selected time-point in each discharge is marked with a vertical line. All plasma parameters except the gas puff, thus plasma density, and the H98 scaling are equal for this time-points. It is a 1 MA discharge with 7.5 MW NBI and about 1.0 MW ECRH heating power. The gas fueling is done using two valves. The time-trace of only one of them is plotted, because the fueling scheme is identical. The total fueling rates are zero for #23226, $5.6 \cdot 10^{21}\,\mathrm{s}^{-1}$ for #23221 and $9.0 \cdot 10^{21}\,\mathrm{s}^{-1}$ for #23225.

$T_i = T_e$ assumption which only holds for high collisionalities. Using the ion temperature gradient, which is flatter than the electron temperature gradient would lead to a better agreement with the measurement. Increasing the NBI heating power to 10 MW (green profiles) did not cause a further steepening, but rather a slight flattening of the edge profiles and a barely unchanged collisionality. Therefore, $\nabla p/n$ and the neoclassical prediction did not change significantly.

8.4.2 Gas puff scan

In H-mode discharges, the H98 factor[15] is used to classify the quality of the confinement compared to ITER. By varying the gas puff level, it is analyzed whether changes in the H98 factor have an influence on the depth of the radial electric field. Discharges #23226, #23221 and #23225 each have a phase where all plasma parameters are very similar except the gas puff level. An overview of the time-traces of relevant plasma parameters is given in figure 8.4. Discharge #23226 and #23225 are evaluated at 3.27 s and discharge #23221 at 3.96 s. From one discharge to the other, the fueling level

---

[15] H98(y,2) is the enhancement factor of thermal energy confinement τ_{th} compared to the ITER scaling IPB98(y,2).[60]

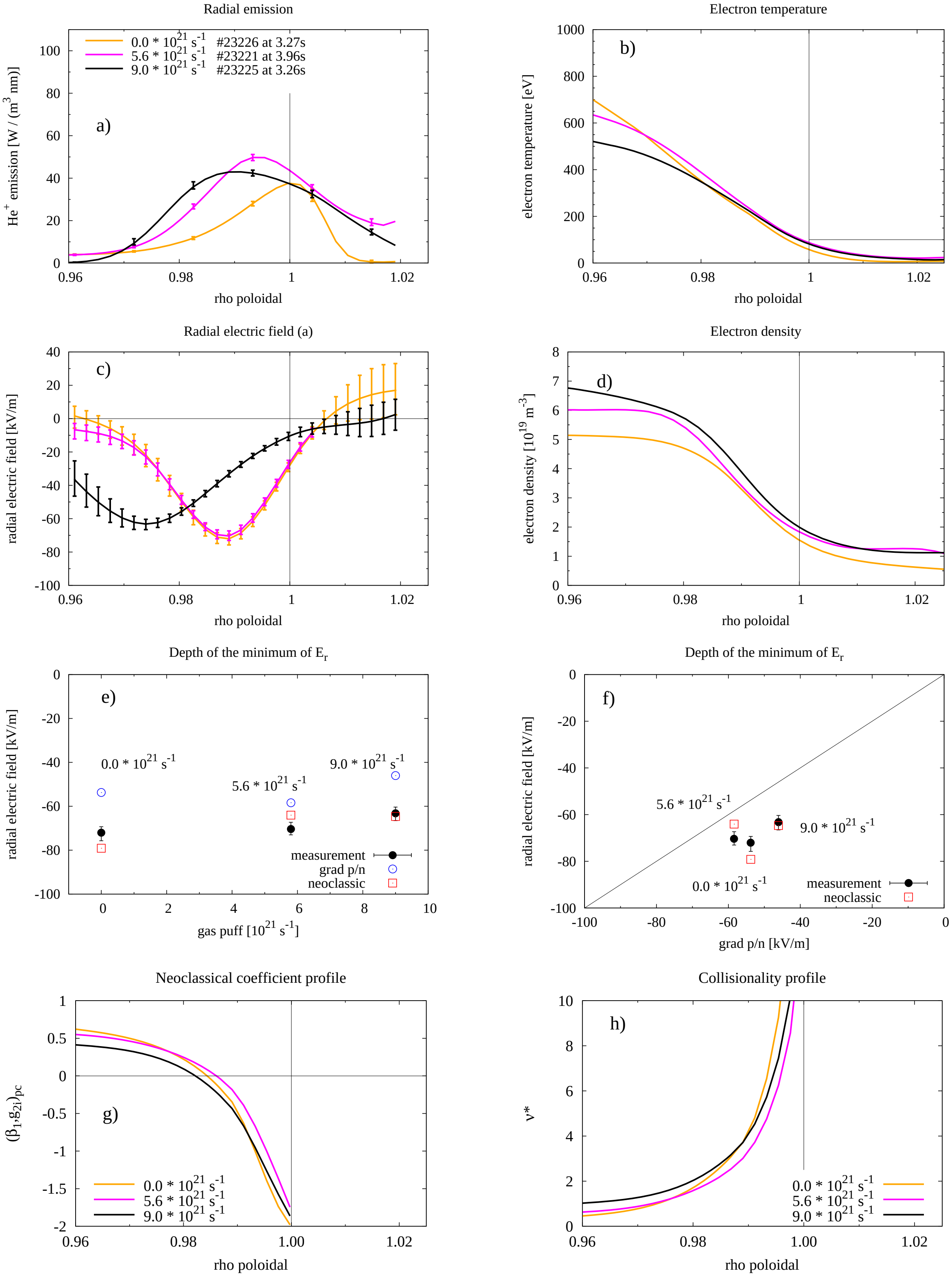

Figure 8.5: Comparison of discharges with three different gas puff levels

increases, $0.0 \cdot 10^{21}\,\mathrm{s}^{-1}$, $5.6 \cdot 10^{21}\,\mathrm{s}^{-1}$ and $9.0 \cdot 10^{21}\,\mathrm{s}^{-1}$, while the H98 factor decreases from 1.02 ± 0.2 over 0.92 ± 0.2 to 0.90 ± 0.2. The results of this gas puff scan are plotted in figure 8.5. Sub-figure b) and d) show the edge pedestal with an increasing pedestal top density and decreasing pedestal top temperature for increasing gas puff. The gradients of these profiles stay nearly constant. Sub-figures a) and c) show the estimated emission and radial electric field profiles. With increased gas puff, the shape and depth of the minimum in the radial electric field remains nearly unchanged. The variation in the position is within the combined uncertainties of the measurements and the equilibrium reconstruction, mentioned in the last section.

Sub-figure e) shows the comparison of the depth of the estimated radial electric fields to neoclassical theory as well as to $\nabla p/n$. The effect of the collisionality and temperature dependent neoclassical correction compared to $\nabla p/n$ is emphasized in sub-figure f). The high collisionality (sub-figure h)) in this series of discharges lead to a negative neoclassical coefficient (sub-figure g)) in the area around the minimum and thus to a deeper predicted minimum in E_r, which is well confirmed by the measurements. Because of the nearly unchanged collisionalities and edge pressure gradients for all three gas puff levels, there is only a small variation in the theoretical prediction, which is also reproduced by the measurement. From the increasing density and unchanged pressure gradient, a decrease in $\nabla p/n$ and therefore also of the neoclassical prediction is expected. Due to the uncertainties of the edge gradients, a clear trend could not be found but comparing the discharge with the highest gas puff level to the other two, a small reduction of $\nabla p/n$ and of the measured minimum can be observed.

8.5 L-H transition

After having discussed examples of varying heating power and fueling, this section concentrates on the transition from L- to H-mode. The development of the radial electric field during the transition is very important, because it plays a major role in transport reduction (see chapter 2.5 for a detailed discussion). In the following, discharge #24923, which is presented in figure 8.6, is used to analyze the L-H transition. It is a 0.8 MA discharge with a toroidal magnetic field of -2.5 T. In the observed time-interval constant NBI heating of 1.2 MW was applied. The L-H transition was started by switching on 1.5 MW of ECRH. The plots on the right-hand side of the figure are a close up of the L-H transition indicated by the yellow bar in the left-hand side of the figure. One can see, that after switching on ECRH at 2.0 s, the plasma stays in L-mode for 40 ms. At 2.04 s, there is the typical drop in the signal of the divertor current (I_{polsola}), that indicates the start of the L-H transition (see uppermost plot in figure 8.7). Plot b) in figure 8.7 shows the measured line integrated raw signal for one line of sight in counts. In L-mode (< 2.04 s) there is a nearly constant emission of about 7500 counts, which decreases during the L-H transition to 6000 counts. The first clear ELMs that could be identified by the ELM detection code start at 2.06 s. A correlation between the ELM

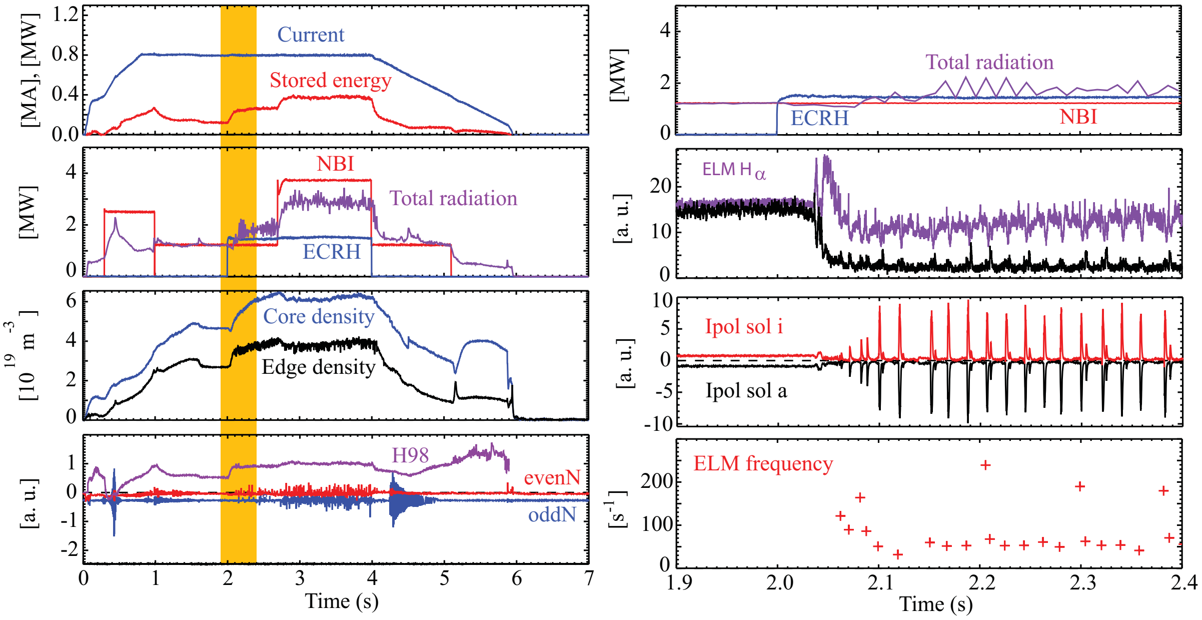

Figure 8.6: Overview of shot #24923 on the left; close up on the L-H transition on the right

onset and the increased measured emission can be observed. The reason for this is the already discussed increased transport towards the walls during the ELM.

The results of the radial electric field calculations for this discharge are plotted in graph c) and d) of figure 8.7. In the L-mode phase, a nearly constant depth of the minimum is measured at -16 kV/m. AUGPed was used to fit the edge electron density and temperature profiles. All profiles from 1.8 s to 2.0 s were used for the fit. The E_r measurement is in good agreement with the neoclassical prediction. The last time-point of this phase might already be an indicator for the L-H transition by a deeper well in the radial electric field compared to the prediction using L-mode edge profiles, because it is the time-point which indicates the actual L-H transition.

The next two time-points, region B, were calculated using IDA density profiles with the high time-resolution of 1 ms. But only one electron temperature profile was used, fitted by the modified hyperbolic tangent function from AUGPed. Averaging over the whole 8 ms was done in order to include one Thomson electron temperature measurement to reduce the uncertainties in the ECE shine through region of the IDA temperature profile. By looking at figure 8.7 one can see, that the slightly steeper profiles compared to the L-mode profiles better match the measurements. The small reduction of the E_r-well depth in the second time-point of this phase may be due to the influence of a small early ELM (perhaps a type III-ELM), which was below the detection limit of the ELM-detection software. This is supported by looking at the integrated line intensity.

The edge profiles of region C are aligned and fitted in the same way as in region B. The

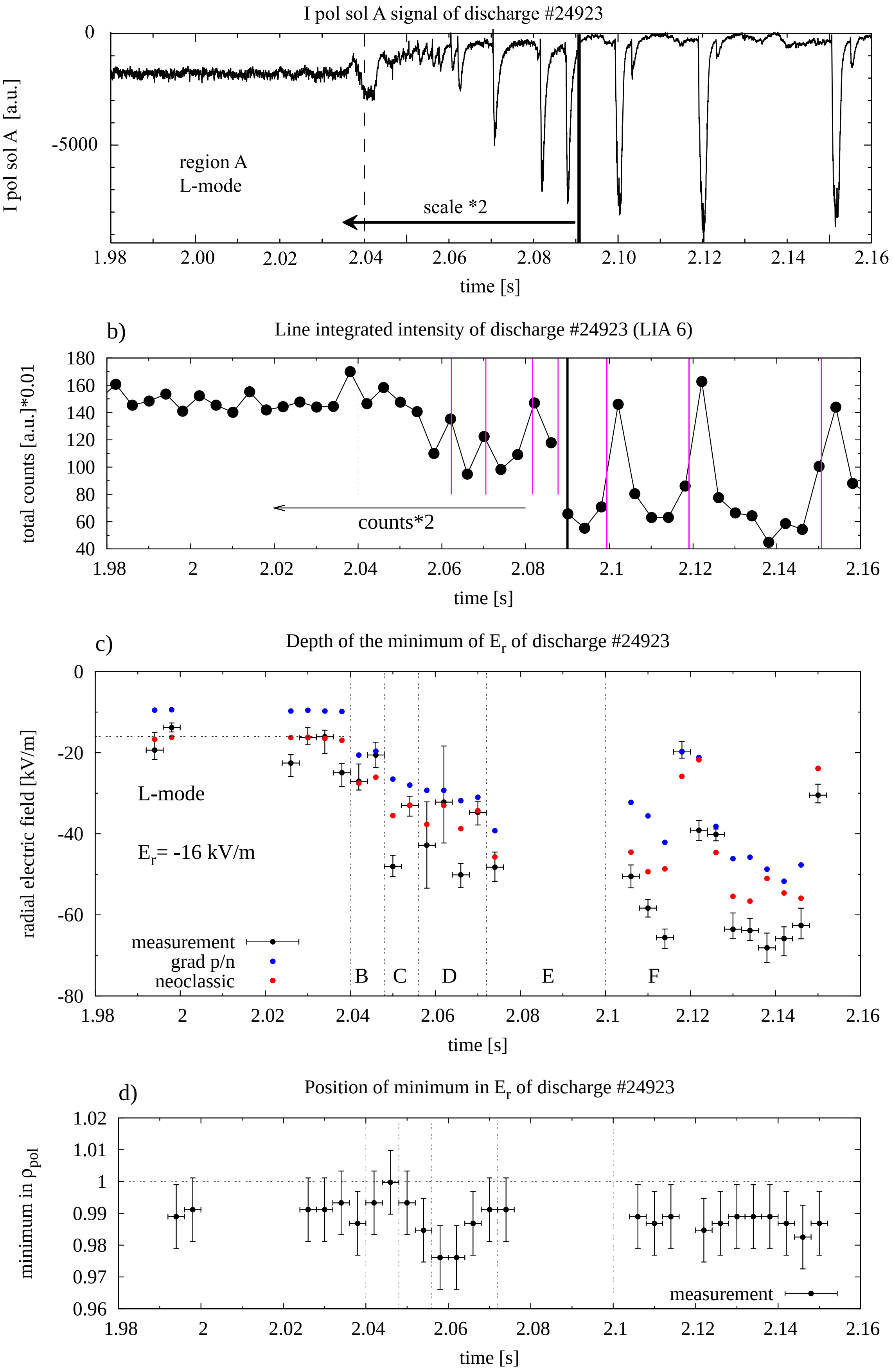

Figure 8.7: Comparison of the depth of the minimum of measured radial electric field to theory during the L-H transition

density profile is taken from the IDA diagnostic and the electron temperature profile was improved by the AUGPed modified hyperbolic tangent fit. The discrepancy between the prediction in the first time-point of this region and the good agreement with the second one probably results from the fact, that for both time-points the same temperature profiles was used and it was too early to apply ELM filtering. Therefore, the gradients, which are steeper than in the previous regime, are governed by a small early ELM during the second time-point in this region.

In region D, the first larger ELM's were detected (vertical magenta lines in sub-figure 2). This can be seen in the structures in the integrated line intensity, in the I_{polsola} signal as well as in the alternating depth of the radial electric field. The theoretical prediction agrees only with the time-points containing an ELM, because the interval was too small to apply ELM synchronization in AUGPed.

The only measurement point in region E was compared to the theory with completely ELM synchronized AUGPed profiles and shows good agreement to neoclassical theory. The remaining time-points in this region could not be evaluated, because no Lithium beam data and thus no IDA data were available.

In the last evaluated region F, there is a clear H-mode plasma with strong and very low frequent ELMs. The radial electric field for two ELM cycles was calculated and included in figure 8.7. The ELM crash and the recovery phase of the radial electric field can be clearly seen, as well as a stable phase around 2.14 s with maximal depth until the next ELM crash. In this region only IDA profiles were used for electron density and temperature reconstruction. $\nabla p/n$, the blue dots, show good agreement in the field development but has constantly too low maximal depth (of about $\approx 20\,\mathrm{kV/m}$). The neoclassical term, green dots, which is also dependent on the collisionality and the temperature gradient, shows better agreement with the measurements. Due to the very uncertain gradient of the edge electron temperature in H-mode caused by ECE shine through, the agreement with the measured data varies for each time-point.

The lowest plot in figure 8.7 shows the temporal development of the position of the minimum in the radial electric field. All data points lie in the region $0.98 < \rho_{pol} < 1.0$, which is the region with steep gradients in H-mode. This corresponds to the measurement resolution of the presented radial electric field diagnostic. Therefore, no conclusions could be drawn regarding the position of the E_r minimum relative to the separatrix.

8.6 Dependency of E_r on collisionality

Having discussed the depth of the radial electric field for different plasma parameters and during a L-H transition, it turned out, that the collisionality and temperature dependent term in the neoclassical prediction of the radial electric field is crucial.

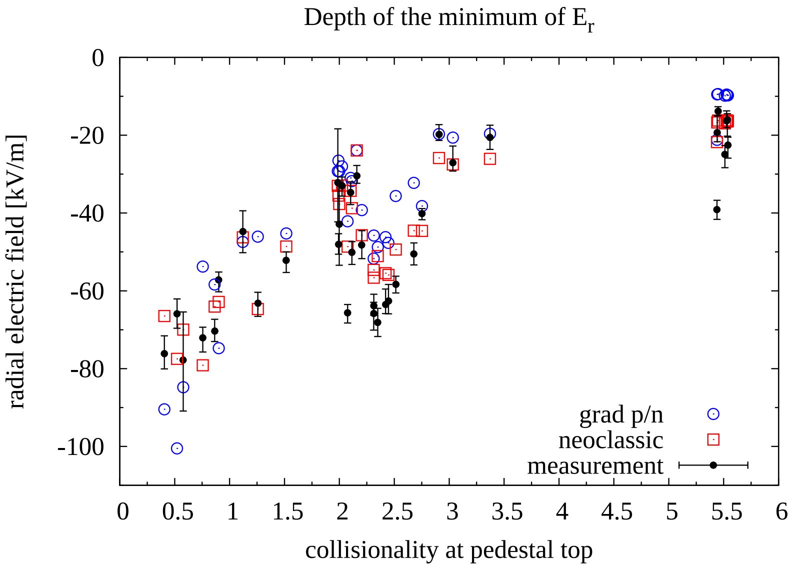

Figure 8.8: Collisionality dependence of the theoretical and measured radial electric field of all analyzed time-points

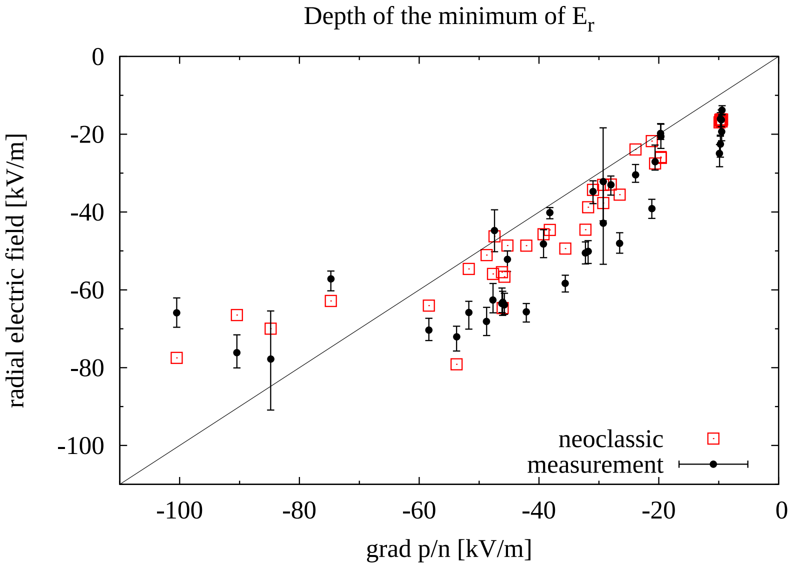

Figure 8.9: Comparison of measured and neoclassical depth at the minimum of the radial electric field to $\nabla p/n$

To discuss the collisionality dependence of the neoclassical theory, all analyzed discharges in this work are plotted over the pedestal top collisionality ($\rho_{pol} = 0.97$) in figure 8.8. The measurements, plotted in black with error bars, are compared to $\nabla p/n$ (blue) and the neoclassical prediction (red). The depths of the evaluated radial electric fields obviously gets deeper for decreasing collisionality. Furthermore, one can see that the neoclassical factor (β_1, g_{2i}) (see equation (2.43) or chapter 8.2) changes its sign at a collisionality of about $\nu_* \approx 1.0$. For discharges with a higher collisionality, the neoclassical prediction for the minimum of the radial electric field is deeper than $\nabla p/n$ and for discharges with a lower collisionality the predicted field is flatter. This is emphasized in figure 8.9. The minima of the neoclassical and the measured radial electric fields are plotted against $\nabla p/n$ to emphasize the effect of the collisionality and temperature dependent term in the neoclassical theory. In this figure, the change of the sign of the neoclassical factor at a collisionality of $\nu_* \approx 1$, which corresponds to a $\nabla p/n$ minimum depth of about $70\,\mathrm{kV/m}$ for the evaluated discharges, is even more obvious. The measurements perfectly agree with this sign dependence on the collisionality. Furthermore, looking at figure 8.9, one can see that the depth of the measured radial electric field follows $\nabla p/n$ with a displacement of $\approx -15\,\mathrm{kV/m}$ until the collisionality gets too low and the temperature and collisionality dependent term gets more important.

9 Summary and Conclusions

This PhD thesis was done at the Max-Planck-Institute for Plasma Physics (IPP) in Garching, Germany and all measurements used for data evaluation were made at the ASDEX Upgrade Tokamak. Inspired by a promising feasibility study carried out during my diploma thesis also at the IPP, a new diagnostic for measuring the radial electric field E_r by passive He II emission was installed at ASDEX Upgrade. The main focus of this diagnostic is on the edge pedestal region with its distinctive minimum in the E_r, which has an important role in widely accepted theories on turbulence reduction in H-mode.

The radial electric field diagnostic presented in this work is a passive method, that measures line integrated He II spectra ($\lambda_0 = 468.57\,\mathrm{nm}$) from the plasma boundary. Bayesian statistics was used to unfold the spectra. Therefore, a forward model was developed, describing the relation between the plasma properties and these spectra. Furthermore, this Bayesian approach provided the ability to include a consistent error propagation through the complete forward model using a Marcov chain Monte Carlo algorithm. The basic concept of modeling the measured spectra is based on calculating the line shift from the perpendicular drift motion (ExB and diamagnetic drift), the width from the He^+ ion temperature and the amplitude from the He^+ ion density using a collisional-radiative model. Therefore, it is also possible to make predictions on the He^+ density and temperature in the region with high He II emission.

The accuracy of the new radial electric field diagnostic and the impact of uncertainties, not included in the forward model, was analyzed in a sensitivity study. The most important finding was that the determination of the radial electric field is independent of the relative and absolute alignment of the edge pedestal electron temperature and density profiles. The estimated He^+ density profile, on the contrary, is strongly dependent on these profiles and their relative alignment. Furthermore, it could be shown that the effect of fine structure splitting and magnetic splitting on the line center is negligible in the region with steep edge gradients due to the high He^+ ion temperatures and the high perpendicular rotation velocities.

The newly implemented diagnostic could be used for nearly every discharge, due to the passive measurement method. Therefore, a wide variety of discharges could be analyzed. But, because of the long run-time of the Marcov chain Monte Carlo algorithm, the radial electric field was only evaluated for the most significant time points in the selected discharges.
In the field of plasma edge physics, the transition from L- to H-mode is a lively discussed

topic. Hence, an analysis of the temporal development of the depth of the radial electric field before, during and after the transition was done. It was found that the depth of the minimum in the measured radial electric field is about 16 kV/m in L-mode. Due to the fast (< 1 ms) L-H-transition compared to the temporal resolution of the diagnostic (4 ms), the important question whether the increased depth of the radial electric field is the cause or the consequence of the transition could not be answered. But in the following, 40 ms lasting, phase of slowly increasing gradients in the edge temperature and density of the analyzed discharge, a behavior of the depth of the radial electric field comparable to the edge gradients was found. This suggested a connection of this depth to the edge gradients, which is corroborated by neoclassical theory

$$E_{r,neo} = \frac{T_D}{q_D}\left[\frac{\partial \ln P_D}{\partial r} - (\beta_1, g_{2i})\frac{\partial \ln T_D}{\partial r}\right] = \frac{\nabla P_D}{q_D n_D} - (\beta_1, g_{2i})\frac{\nabla T_D}{q_D}.$$

$\nabla P_D/n_D$ of the main ions is the leading term, which is corrected by the second term, that is dependent on main ion temperature, collisionality and the inverse aspect ratio. In both, the L-mode phase and the transition phase, good agreement in the predicted depth of the minimum compared to the measurement was found within the combined error of the diagnostic and the edge profiles. At the end of the phase with steepening edge gradients and in the following stable H-mode, the edge gradients crashes periodically due to the ELM-cycle. It was shown, that the radial electric field also breaks down simultaneously to the edge gradients, but the time resolution was too low to carry out the temporal development in a single ELM-cycle. By introducing ELM filtering further studies of H-mode discharges could be done.

By varying neutral beam heating power and gas fueling level, measured radial electric fields for different edge gradients and collisionalities were compared to neoclassical theory in order to validate the $\nabla p/n$ dependence of the minimum and also the collisionality dependence of the correction term. Good agreement within the combined uncertainties of the measurement and the edge gradients with neoclassic was found. For lower collisionalities ($\nu_* < 1.0$) the neoclassical coefficient (β_1, g_{2i}) changes its sign and significantly reduces the predicted minimum, which was also verified by the measurements.

In conclusion, there is evidence, that the radial electric field in the transport barrier at the plasma edge is governed by the main ions and that neoclassical theory is appropriate to predict the depth of minimum in this field.

Bibliography

[1] S. Günter. IPP lecture notes: Plasmaphysik 2. 2005.

[2] S. Günter. IPP lecture notes: Plasmaphysik 1. 2005.

[3] J. P. Freidberg. *Ideal Magneto-Hydro-Dynamics*. Plenum Publishing Corporation, New York, 1987.

[4] J. Wesson. *Tokamaks*. Oxford University Press, Inc., New York, 2 edition, 1997. ISBN 0-19-856293-4.

[5] B. Streibl, P. T. Lang, F. Leuterer, J.-M. Noterdaeme and A. Stäbler. Chapter 2: Machine Design, Fueling, and Heating in ASDEX Upgrade. *Fusion Science and Technology*, 44(3), November 2003.

[6] L. Horton, A. Chankin, Y. Chen, G. Conway, D. Coster, T. Eich, E. Kaveeva, C. Konz, B. Kurzan, J. Neuhauser, I. Nunes, M. Reich, V. Rozhansky, S. Saarelma, J. Schirmer, J. Schweinzer, S. Voskoboynikov, E. Wolfrum and the ASDEX Upgrade Team. Characterization of the H-mode edge barrier at ASDEX Upgrade. *Nuclear Fusion*, 45(8):856, 2005.

[7] P. B. Snyder and H. R. e. a. Wilson. Edge localized modes and the pedestal: A model based on coupled peeling-ballooning modes. *Physics of Plasmas*, 5(3), May 2002.

[8] ITER and Fusion Energy. Hompage, 2011. Http://iter.rma.ac.be.

[9] P. C. Liewer. Measurements of microturbulence in Tokamaks and comparisons with theories of turbulence and anomalus transport. *Nuclear Fusion*, 25(5), 1985.

[10] W. Schneider, P. McCarthy, K. Lackner and et al. ASDEX Upgrade MHD equilibria reconstruction on distributed workstations. *Fusion Engineering and Design*, 48:127–134, 2000.

[11] A. R. Field, G. Fussmann and J. V. Hofmann. MEASUREMENT OF THE RADIAL ELECTRIC-FIELD IN THE ASDEX TOKAMAK. *NUCLEAR FUSION*, 32(7), Juli 1992.

[12] P. Helander and D. J. Sigmar. *Collisional Transport in Magnetized Plasmas*. Cambridge Monographs on Plasma Physics, 2002. ISBN 0521807980.

[13] F. L. Hinton and Hazeltine. theory of plasma transport in toroidal confinement systems. *Reviews of Modern Physics*, 48(2), April 1976.

[14] W. X. Wang, F. L. Hinton and S. K. Wong. Neoclassical Radial Electric Field and Transport with Finite Orbits. *Physical Review Letters*, 87(5), July 2001.

[15] L. Spitzer, Jr. *Physics of Fully Ionized Gases*. John Wiley and Sons, London, 2. edition, 1962.

[16] W. M. Stacey. Neoclassical Theory of the Plasma Edge. Technical report, Georgia Institute of Technology, October 1992.

[17] J. W. Connor. The Neo-Classical Transport Theory of a Plasma with Multiple Ion Species. *Plasma Physics*, 15:765–782, 1973.

[18] T. Pütterich, E. Wolfrum, R. Dux and C. F. Maggi. Evidence for Strong Inversed Shear of Toroidal Rotation at the Edge-Transport Barrier in the ASDEX Upgrade. *Phys. Rev. Lett.*, 102(2):025001, Jan 2009.

[19] R. D. Hazeltine. Recursive derivation of drift-kinetic equation. *Plasma Physics*, 15(1):77, 1973.

[20] P. Helander. Effects of a temperature gradient on parallel velocity, May 2011. Private communication.

[21] U. Stroth, P. Manz and M. Ramisch. On the interaction of turbulence and flows in toroidal plasmas. *Plasma Physics and Controlled Fusion*, 53(2):024006, 2011.

[22] T. Kurki-Suonio, S. I. Lashkul and J. A. Heikkinen. Formation and detection of internal transport barriers in low-current tokamaks. *Plasma Physics and Controlled Fusion*, 44(3):301, 2002.

[23] G. D. Conway. Turbulence measurements in fusion plasmas. *Plasma Physics and Controlled Fusion*, 50(12):124026, 2008.

[24] P. W. Terry. Suppression of turbulence and transport by sheared flow. *Rev. Mod. Phys.*, 72(1):109–165, Jan 2000.

[25] A. Fujisawa. A review of zonal flow experiments. *Nuclear Fusion*, 49(1):013001, 2009.

[26] G. D. CONWAY, E. POLI and T. H. aAND the ASDEX Upgrade Team. Interac-

tion of Mean and Oscillating Plasma Flows Across Confinement Mode Transitions. *Plasma Fusion Res.*, 5:S2005, 2010.

[27] D. F. Bates, A. E. Kingston and R. W. P. McWhirter. Recombination Between Electrons and Atomic Ions. I. Optically thin Plasmas. *Proceedings of the Royal Society of London. Series A, Methematical and Physical Science*, 267(1330):297–312, 1962.

[28] H. P. Summers, W. J. Dickson, M. G. O'Mullane, N. R. Badnell, A. D. Whiteford, D. H. Brooks, J. Lang, S. D. Loch and D. C. Griffin. Ionization state, excited populations and emission of impurities in dynamic finite density plasmas: I. The generalized collisional radiative model for light elements. *Plasma Physics and Controlled Fusion*, 48(2):263, 2006.

[29] H. P. McWhirter, R. W. P.; Summers. Atomic Radiation from Low Density Plasma. *Applied Atomic Collision Physics, Volume 2: Plasmas*, page 52, 1984.

[30] T. Puetterich, E. Wolfrum, R. Dux and C. F. e. a. Maggi. . *Physical Review Letters*, 102, 2009.

[31] S. Bellm, K. Lower, Bartschat and et al. Ionization and ionization-excitation of helium to the n=1-4 states of He+ by electron impact. *Physical Review A*, 75, April 2007.

[32] R. Hoekstra, H. Anderson, F. W. Bliek, M. von Hellermann, C. F. Maggi, R. E. Olson and H. P. Summers. Charge exchange from $D(n = 2)$ atoms to low-Z receiver ions. *Plasma Physik and Controlled Fusion*, 40(8), 1998.

[33] R. Dux. STRAHL User Manual. Technical report, IPP-Report 10/30, September 2006.

[34] The ADAS Project. March 2011.
URL `http://adas.phys.strath.ac.uk/`

[35] J. Schweinzer, E. Wolfrum, F. Aumayr, M. Pöckl, H. Winter, R. P. Schorn, E. Hintz and A. Unterreiter. Reconstruction of plasma edge density profiles form Li I (2s-2p) emission profiles. *Plasma Physics and Controlled Fusion*, 34(7):1173–1183, 1992.

[36] E. Wolfrum, J. Schweinzer, M. Reich, L. D. Horton and C. F. Maggi. Impurity ion density measurements at the plasma edge of ASDEX Upgrade using lithium beam charge exchange spectroscopy. *Review of Scientific Instruments*, 77(3), 2006.

[37] W. Suttrop, A. G. Peeters, ASDEX Upgrade team and NBI group. Practical Limitations to Plasma edge Electron Temperature Measurements by Radiometry of Electron Cyclotron Emission. *IPP Report*, 1/306, Dezember 1996.

[38] H. Murmann, S. Gotsch, H. Rohr, H. Salzmann and K. H. Steuer. The Thomson scattering systems of the ASDEX upgrade tokamak. *Review of Scientific Instruments*, 63(10):4941 –4943, October 1992. ISSN 0034-6748.

[39] T. Pütterich, E. Wolfrum, R. Dux and C. F. Maggi. Evidence for Strong Inversed Shear of Toroidal Rotation at the Edge-Transport Barrier in the ASDEX Upgrade. *Phys. Rev. Lett.*, 102(2):025001, Jan 2009.

[40] R. C. Isler. An overview of charge-exchange spectroscopy as a plasma diagnostic. *Plasma Physics and Controlled Fusion*, 36:171–208, 1994.

[41] R. Fischer, C. J. Fuchs, b Kurzan, W. Suttrop, E. Wolfrum and the ASDEX Upgrade Team. INTEGRATED DATA ANALYSIS OF PROFILE DIAGNOSTIC AT ASDEX UPGRADE. *FUSION SCIENCE AND TECHNOLOGY*, 58:675–684, 2010.

[42] E. Wolfrum, A. Burckhart, R. Fischer, N. Hicks, C. Konz, B. Kurzan, B. Langer, T. Pütterich, H. Zohm and the ASDEX Upgrade Team. Investigation of inter-ELM pedestal profiles in ASDEX Upgrade. *Plasma Physics and Controlled Fusion*, 51(12):124057, 2009.

[43] H. Urano, W. Suttrop, L. D. Horton, A. Herrmann, J. C. Fuchs and A. U. Team. Energy and particle losses during type-I ELMy H-mode in ASDEX Upgrade. *Plasma Physics and Controlled Fusion*, 45(9):1571, 2003.

[44] M. Reich, E. Wolfrum, J. Schweinzer, H. Ehmler, L. D. Horton, J. Neuhauser and ASDEX UPGRADE TEAM. Lithium beam charge exchange diagnostic for edge ion temperature measurements at the ASDEX Upgrade tokamak. *Plasma Physics and Controlled Fusion*, 46(5):797–808, 2004.

[45] A. Burckhart, E. Wolfrum, R. Fischer, K. Lackner, H. Zohm and the ASDEX Upgrade Team. Inter-ELM behaviour of the electron density and temperature pedestal in ASDEX Upgrade. *Plasma Physics and Controlled Fusion*, 52(10):105010, 2010.

[46] K. H. Burrell. Effects of E x B velocity shear and magnetic shear on turbulence and transport in magnetic confinement devices. *Physics of Plasmas*, 4(5):1499–1518, 1997.

[47] W. Horton. Drift waves and transport. *Rev. Mod. Phys.*, 71(3):735–778, Apr 1999.

[48] K. Itoh, S.-I. Itoh, P. H. Diamond, T. S. Hahm, A. Fujisawa, G. R. Tynan, M. Yagi and Y. Nagashima. Physics of zonal flows. *Physics of Plasmas*, 13(5):055502, 2006.

[49] J. Neuhauser, D. Coster, H. U. Fahrbach, J. C. Fuchs, G. Haas, A. Herrmann, L. Horton, M. Jakobi, A. Kallenbach, M. Laux, J. W. Kim, B. Kurzan, H. W. Müller, H. Murmann, R. Neu, V. Rohde, W. Sandmann, W. Suttrop, E. Wolfrum

and the ASDEX Upgrade Team. Transport into and across the scrape-off layer in the ASDEX Upgrade divertor tokamak. *Plasma Physics and Controlled Fusion*, 44(6):855, 2002.

[50] T. Lunt, J. Fuchs, K. Mank, Y. Feng, F. Brochard, A. Herrmann, V. Rohde and N. Endstrasser. A new 3D viewer as an interface between the ASDEX Upgrade CAD models and data from plasma modelling and experiment. *Nuclear Instruments and Methods in Physics Research Section A: Accelerators, Spectrometers, Detectors and Associated Equipment*, 623(2):812 – 814, 2010. 1rs International Conference on Frontiers in Diagnostics Technologies.

[51] R. Fischer, E. Wolfrum, J. Schweinzer and ASDEX Upgrade Team. Probabilistic lithium beamdata analysis. *Plasma Physics and Controlled Fusion*, 50:5, June 2008.

[52] V. Dose and W. Von der Linden. Outlier tolerant parameter estimation. *MAXIMUM ENTROPY AND BAYESIAN METHODS*, 105:47–56, 1999.

[53] D. S. Sivia. *Data Analysis, A Bayesian Tutorial*. Oxford University Press Inc., New York, 1996.

[54] NAG-Fortran 90 library. Hompage, 2010. Http://www.nag.co.uk.

[55] National Institute of Standards and Technology. Hompage, 2010. Http://physics.nist.gov.

[56] S. Chib and E. Greenberg. Understanding the Metropolis-Hastings Algorithm. *The American Statistician*, 49(4):pp. 327–335, 1995. ISSN 00031305.

[57] S. P. Brooks. Markov Chain Monte Carlo Method and Its Application. *Journal of the Royal Statistical Society. Series D (The Statistician)*, 47(1):pp. 69–100, 1998. ISSN 00390526.

[58] D. B. Hitchcock. A History of the Metropolis-Hastings Algorithm. *The American Statistician*, 57(4):pp. 254–257, 2003. ISSN 00031305.

[59] N. Metropolis and S. Ulam. The Monte Carlo method. *J. Amer. Statistical Assoc*, pages 335–341, 1949.

[60] ITER Physics Expert Group on Confinement and Transport and ITER Physics Expert Group on Confinement Modelling and Database and ITER Physics Basis Editors. Chapter 2: Plasma confinement and transport. *Nuclear Fusion*, 39(12):2175, 1999.

[61] J. Schirmer, G. Conway, H. Zohm, W. Suttrop and the ASDEX Upgrade Team.

The radial electric field and its associated shear in the ASDEX Upgrade tokamak. *Nuclear Fusion*, 46(9):S780, 2006.

[62] R. McDermott. *Edge Radial Electric Field Studies Via Charge Exchange Recombination Spectronscopy on the Alcator C-Mod Tokamak*. Ph.D. thesis, Saint Louis University, 2009.

[63] N. Hosogane, H. Ninomiya, M. Matsukawa, T. Ando, Y. Neyatani, H. Horiike, S. Sakurai, K. Masaki, M. Yamamoto, K. Kodama, T. Sasajima, T. Terakado, S. Ohmori, Y. Ohmori and J. Okano. Development and Operational Experiences of the JT-60U Tokamak and Power Supplies. *Fusion Science and Technology*, 42(2,3):368–385, 2002.

[64] K. Kamiya, K. IDA, Y. Sakamoto, G. Matsunaga, A. Kojima, H. Urano, N. Oyama, Y. Koide and Y. Kamada. Observation of a Complex Multistage Transition in the JT-60U H-mode Edge. *Physical Review Letters*, 105:045004, 2010.

[65] J. Luxon. A design retrospective of the DIII-D tokamak. *Nuclear Fusion*, 42(5):614, 2002.

[66] P. Gohil, K. Burrell and T. Carlstrom. Parametric dependence of the edge radial electric field in the DIII-D tokamak. *Nuclear Fusion*, 38(1):93, 1998.

[67] K. H. Burrell, W. P. West, E. J. Doyle, M. E. Austin, J. S. deGrassie, P. Gohil, C. M. Greenfield, R. J. Groebner, R. Jayakumar, D. H. Kaplan, L. L. Lao, A. W. Leonard, M. A. Makowski, G. R. McKee, W. M. Solomon, D. M. Thomas, T. L. Rhodes, M. R. Wade, G. Wang, J. G. Watkins and L. Zeng. Edge radial electric field structure in quiescent H-mode plasmas in the DIII-D tokamak. *Plasma Physics and Controlled Fusion*, 46(5A):A165, 2004.

Glossary

Notation	Description	
(β_1, g_{2i})	Collisionality and plasma shape dependent neoclassical factor	25, 85
ADAS	The IPP is member of the Atomic Data and Analysis Structure project. Therefore, a variety of atomic data, like atomic cross-sections and associated calculation tools can be used.	29
A_l	Amplitude of the Voigt profile used for profile calculation by the forward model.	53
ASDEX	Axial Symmetric Divertor Experiment	5
AUGPed	A graphical tool to fit the pedestal profiles using the combined data from different diagnostics.	41
$\vec{B}$	Magnetic field vector: It consists of a poloidal $\vec{B}_p$ and a toroidal $\vec{B}_t$. The poloidal one can be derived from poloidal flux Ψ_p and has two components B_R and B_z.	15
β	Ratio of kinetic pressure to magnetic pressure	3
$\bar{C}$	Covariance matrix of the posterior PDF.	65
$C_{A,k}$	Absolute intensity calibration factor for the k-th line of sight.	56
$C_{A,n}$	Absolute intensity calibration factor for the n-th channel.	49
χ^2	Squared normalized residual of the Bayesian parameter estimation.	58
CLISTE	The CompLete Interpretive Suite for Tokamak Equilibria is a Grad-Shafranov solver used to calculated reconstruct the equilibrium at ASDEX Upgrade.	15
CXRS	The electron cyclotron emission diagnostic measures highly resolved edge electron temperature profiles.	40
DCN interferometer	A set of Deuterium CyaNide (DCN) laser interferometers, which are used to measure line integrated electron densities.	8, 40
ELM	The edge localized mode is a typical edge instability of H-mode discharges.	9

Notation	Description	
ETB	The edge transport barrier is a typical feature of H-mode discharges.	8
$\delta\lambda_{0,l}$	Width of the Gaussian part of the Voigt profile used for profile calculation by the forward model.	55
$\delta\lambda_L$	Width of the Lorentzian part of the Voigt profile used for profile calculation by the forward model.	55
ECE	The electron cyclotron emission diagnostic measures highly resolved edge electron temperature profiles.	39
ECRH	Electron Cyclotron Resonant Heating	8
ϵ	Inverse aspect ratio of a Tokamak	7
E_r	Radial electric field	25, 84
M	Forward model M used for probabilistic data analysis with the model-parameters $\vec{\eta}$.	51
$\vec{\eta}$	Parameters of the forward model M used for probabilistic data analysis.	51
F	Number of counts, calculated by the forward model, that are expected for a given set of model parameters.	56
$f\left(\vec{r}, \vec{v}, t\right)$	Time-dependent particle density in a volume in the 6-dimensional phase space.	19
$g_l\left(\lambda, M\left(\vec{\eta}\right)\right)$	Local line emission profile at a certain ρ_{pol}-position, calculated by the forward model M.	53
$\vec{\Gamma}_{a\perp}$	Perpendicular particle flow of species a. In addition to the poloidal component, there is also a classical $\vec{\Gamma}_a^c$ and a neoclassical$\vec{\Gamma}_a^{nc}$ one.	20
$h\left(\lambda, \lambda_0, \delta\lambda_G, \delta\lambda_L\right)$	Voigt function at the position λ_0 with a Gaussian width of $\delta\lambda_G$ and a Lorentzian width of $\delta\lambda_L$.	55
I	Background information I of the forward model M.	51
IDA	Integrated Data Analysis	42
$\vec{J}_{tor}$	Toroidal plasma current induced by the ohmic transformer	3
JET	Joint European Torus	9
k_B	Boltzmann constant	84
L	Negative logarithm of the posterior PDF	65
$\lambda_{0,l}$	Position of the Voigt profile used for profile calculation by the forward model.	54

Notation	Description	
λ_C	Tabulated un-shifted central wavelength of the observed He II transition from the NIST database.	54
λ_{Corr}	Correction to the wavelength calibration using a Zn spectral-lamp.	56
LIA	Name of one of the two spectrometers used in this work to measure He^+ spectra.	45
LIC	Name of one of the two spectrometers used in this work to measure He^+ spectra.	45
MSE	The ... diagnostic ...	15
μ	Magnetic moment of a gyrating particle	17
N	Number of counts detected by the CCD camera.	56
N_a	Number of particles of the species a in a given volume.	24
n_D	Deuterium density, approximated by the electron density	84
ν^*	Normalized collision frequency of trapped particles to the bounce frequency of the banana orbit	7
O_k	Offset in counts for each line of sight of the forward model.	56
Ω_a	Cyclotron frequency of the species a.	20
$p\left(X \mid I\right)$	Probability of hypothesis X under the condition I. $\bar{X}$ represents the complementary of X.	51
PDF	Probability Density Function	52
PEC	The photon emission coefficients calculated by an ADAS routine can be used to calculated the number of photons emitted by a certain transition.	32
Φ	Electrostatic potential leading to a predominantly radial electric field $\nabla\Phi$.	19
π	Viscosity tensor between the different particle species.	19
Ψ	The Magnetic flux can be separated in a poloidal component Ψ_p and a toroidal component Ψ_t. Ψ_0 represents the poloidal magnetic flux on the magnetic axis and Ψ_S the flux on the separatrix.	15
Q	Ratio of external heating compared to internal α particle heating	6
q	Safety factor, which is a measure for the slope of the magnetic field lines	7
q_D	Electric charge of Deuterium	84

Notation	**Description**	
$\vec{r}\left(\lambda, M\left(\vec{\eta}\right)\right)$	Model output: Line integrated spectrum for each line of sight dependent on the given set of model parameters $\vec{\eta}$	52
ρ_{pol}	normalized poloidal radius	13
$\varsigma\left(\lambda\right)$	Measured spectrometer function.	55
$\sigma_{C_{A,n}}$	Standard deviation of the absolute intensity calibration factor for the n-th channel.	49
σ_N	Statistical noise of the measured photon count.	57
σ_r	Read-out noise due to the applied electronic devices.	57
$\vec{\sigma}_\xi$	Gaussian distributed error of the nuisance parameters.	59
STRAHL	This is a code to calculate the transport and emission of impurities in a plasma.	34
T_a	Temperature profile of the species a.	24
τ_E	Energy confinement time	5
Υ	CCD camera specific conversion factor from measured counts to detected photons.	56
v_D	Drift motion of a charged particle in a magnetic field $\vec{B}$ by an perpendicular external force $\vec{F}$	16
$v_{He^+,P}\left(\rho_{pol}\right)$	Combined velocity profile projected on the line of sight, with contributions from the $E \times B$-velocity, the diamagnetic velocity and the toroidal velocity	55
$\vec{\xi}$	Nuisance parameters of the forward model.	59
Z_a	Charge number of species a.	24

Index

A

acceptance rate . . . 67
Alcator C-Mod . . . 83
ASDEX Upgrade . . . 5
atomic processes
  charge-exchange . . . 30, 33
  impact excitation . . . 29, 33
  impact ionization . . . 30
  ionization . . . 30, 33
  radiative recombination . . . 30
  recombination . . . 30, 33
  secondary ionization . . . 30
  spontaneous emission . . . 29
atomic waste . . . 1
AUGddd program . . . 49
AUGPed . . . 41

B

Banana orbits . . . 7
Bayes theorem . . . 51
Bayesian probability theory . . . 51
Boltzmann-equation . . . 19

C

collisional-radiative model . . . 29
collisionality . . . 7, 85
confinement
  gravitational . . . 1
  magnetic . . . 2
  -time . . . 6
  θ-pinch . . . 3
  Z-pinch . . . 3
covariance matrix . . . 66

D

Deuterium-Tritium reaction . . . 2
diagnostics
  CXRS . . . 40
  DCN interferometer . . . 40
  ECE . . . 39
  Li-beam . . . 39
  Thomson-scattering . . . 40
DIII-D . . . 83
divertor . . . 4
Doppler
  reflectometry . . . 83
  broadening . . . 55
  shift . . . 54
drift kinetic equation . . . 23
  0th-order . . . 23
  1th-order . . . 24
drift-motion . . . 16
  diamagnetic drift . . . 18
  $E \times B$-drift . . . 17
  excitation probability drift . . . 18
drift-wave fluctuations . . . 27

E

eddy decorrelation . . . 27
electric field . . . 19
  radial . . . 8, 25, 84, 85
ELM
  cycle . . . 43
  synchronization . . . 43

F

FARO system . . . 49
fine structure splitting . . . 35
fission, nuclear . . . 1
fluid-drift . . . 18
flux surfaces . . . 4
Fokker-Planck equation . . . 19

forward model 53
fossil resources 1
friction
  parallel 22
  poloidal 21
fusion, nuclear 1

G

geodesic acoustic mode 27
Grad-Shafranov equation 15
guiding-center approach 2, 16

H

heating
  external 4
  internal 6
Hessian matrix 66

I

in-situ correction 49
instability
  edge localized mode 9
  peeling-ballooning 10
inverse aspect ratio 7, 85

J

JT60-U 83

M

Marcov chain 66
  detailed balance 67
  random walk chain 67
marginalization 52
Metropolis-Hastings 66

N

normal distribution 57
nuisance parameters 52, 60

O

operation regimes
  H-mode 8
  L-mode 8

P

particle flow
  ambipolar 21, 22
  classical 21
  neoclassical 22
  parallel 23
  poloidal 20
Paschen-Back-effect 36
pedestal, edge 8
Pfirsch-Schlüter currents 17, 23, 26
photon emission coefficients 32
photon noise 57
posterior probability 52
prior probability 52
probability density function
  Binomial- 57
  likelihood- 52
  Poisson- 57
  posterior- 65
  prior- 59
proton-proton chain 1

R

radial force banance equation 20
readout noise 57
reflections 50
residual, normalized 58
Reynolds stress 27

S

safety factor 7
separatrix 4, 14
Shafranov-shift 4
Sterling approximation 57

T

transport 19
  anomalous 7
  classical 6
  neoclassical 6
  turbulent 7, 26

trapped particles 7
tunnel effect 1

U

Ulbricht sphere 49

Z

Zeeman-effect 36
Zn-lamp 49
zonal flows 27